

Partial Discharge Recognition of Defects in Gas Insulated Systems under DC Voltage

Serge Blufpand

Supervisor: Prof. dr. J.J. Smit

Daily supervisor: Dr. ir. Armando Rodrigo Mor

A thesis presented for the degree of
M.Sc of Electrical Engineering

Electrical Sustainable Energy Department
DC Systems and Storage Group
Technical University of Delft
The Netherlands

Thesis committee:

Prof. dr. J.J. Smit

Dr. ir. Armando Rodrigo Mor

Dr. ir. Olindo Isabella

Delft University of Technology
Faculty of Electrical Engineering, Mathematics and Computer Science
Electrical Sustainable Energy Department
DC Systems and Storage Group
The Netherlands

*In loving memory of my grandparents,
and to my parents and siblings.*

Partial Discharge Recognition of Defects in Gas Insulated Systems under DC Voltage

Serge Blufpand

Abstract

Gas insulated substations have become an increasingly important part of the power system due to the high reliability and the compactness of the design made possible by using SF_6 as insulating medium. To keep the availability of the power system high, the reliability of a Gas Insulated System (GIS) should be further improved by the prevention of a major cause of failure through the timely detection of major insulation defects.

Time based maintenance is systematically being replaced by condition based maintenance that aims to reduce the costs that are associated with the maintenance of high voltage equipment and prevent possible failures. Though, Partial Discharge (PD) monitoring is accredited as a fundamental diagnostic tool for Alternating Current (AC) GIS, it has been little investigated for Direct Current (DC) applications. The growing application of High Voltage Direct Current (HVDC) transmission creates a need for a similar diagnostic tool for the DC GIS.

This thesis focuses on the development of a diagnostic tool for GISs subjected to HVDC based on PD measurements. The research focuses on the major insulating defects that can have a detrimental effect on the operation of the GIS.

The insulating defects and the conditions have been modelled by use of true to scale experiments. Signature PD patterns for AC conditions associated with the defects have been used to validate the experiments. For applied DC voltage, characteristic graphs of PDs associated to the insulation defects are obtained making use of the conventional PD detection system. In addition to off-line defect recognition using the IEC 60270 method, Radio Frequency (RF) PD detection measurements are used to establish a relationship to the apparent charge for use in on-line defect recognition.

The main purpose of this research project is an investigation into the applicability of PD measurements as a diagnostic tool for assessment of the insulation of a DC GIS.

Contents

Abstract	iv
Contents	v
List of Abbreviations	viii
List of Figures	ix
List of Tables	xii
Nomenclature	xiv
1 Introduction	1
1.1 Motivation	1
1.2 HVDC Gas Insulated Systems	1
1.2.1 PD sources in GIS	3
1.3 Thesis Overview	4
1.4 Thesis Objectives	5
2 Partial Discharge Phenomena in GIS	6
2.1 Partial Discharge Physics	6
2.1.1 Ionization	6
2.1.2 De-ionization	9
2.2 Breakdown Mechanisms in Gas	11
2.2.1 Pre-breakdown phenomena in gases	11
2.2.2 Townsend mechanism	14
2.2.3 Streamer mechanism	15
2.3 Partial Discharges in GIS	16
2.3.1 Partial discharge conditions	16
2.3.2 DC electric field	17
2.3.3 Corona discharges	18
2.3.4 Internal discharges	22
2.3.5 Surface discharges	28
2.3.6 Floating Components	32
2.4 Insulating Gases	33
3 Measurement Setup and Detection Systems	35
3.1 Measurement Setup	35
3.1.1 Test Object	35
3.1.2 High Voltage Circuit	35
3.2 Partial Discharge Detection	36
3.2.1 IEC 60270 - Conventional Detection Method	37

3.2.2	Ultra High Frequency (UHF) - Non-conventional Detection Method	41
3.2.3	The PD current pulse	44
3.3	Detection Units	45
3.3.1	Techimp PDBaseII	45
3.3.2	Agilent E4403B	47
3.3.3	Tektronix DPO7354C	48
3.4	Noise	49
4	Partial Discharge Analysis	50
4.1	PD features	50
4.2	Feature Extraction	51
4.2.1	Pulse waveform analysis	51
4.2.2	Pulse sequence analysis	53
5	Experimental Results I: DC recognition of PD defects	55
5.1	Floating Components	55
5.1.1	AC Voltage	56
5.1.2	DC Voltage	59
5.1.3	Discussion	64
5.2	Internal Discharges	65
5.2.1	AC Voltage	65
5.2.2	DC Voltage	68
5.2.3	Discussion	72
5.3	Surface Discharges	73
5.3.1	AC Voltage	73
5.3.2	DC Voltage	77
5.3.3	Discussion	85
6	Experimental Results II: RF PD calibration in GIS	86
6.1	Introduction	86
6.2	PD Measurement	87
6.2.1	Acquirement of data	87
6.2.2	Tools for quantitative data analysis	88
6.3	Results and discussion	89
6.3.1	Floating component discharges	89
6.3.2	Negative corona	91
6.3.3	Positive corona	92
6.3.4	Internal discharges	94
6.3.5	Surface discharges	96
6.3.6	Discussion	97
7	Conclusions and Recommendations	102
7.1	Conclusions	102
7.1.1	Recognition of PD under DC	102
7.1.2	RF method	102
7.2	Recommendations for future research	103
	Appendix A Spectrum Analyser Fundamentals	104
	Appendix B Amplifier response	107
	Acknowledgements	109

Bibliography	110
---------------------	------------

List of Abbreviations

AC	Alternating Current
CD	Coupling Device
DC	Direct Current
EM	Electromagnetic
EMI	Electromagnetic Interference
FFT	Fast Fourier Transform
GIS	Gas Insulated System
HF	High Frequency
HFCT	High Frequency Current Transformer
HV	High Voltage
HVAC	High Voltage Alternating Current
HVDC	High Voltage Direct Current
IF	Intermediate Frequency
LV	Low Voltage
LO	Local Oscillator
PD	Partial Discharge
PRPD	Phase Resolved Partial Discharge
PWM	Pulse Width Modulation
RBW	Resolution Bandwidth
RF	Radio Frequency
SA	Spectrum Analyser
SNR	Signal-to-Noise Ratio
ST	Sweep Time
UHF	Ultra High Frequency
VHF	Very High Frequency

List of Figures

1.1	Cross-section view of Gas-Insulated Substation [2].	2
1.2	Cause of dielectric failures in 123 kV and 420 kV GIS based on a study of German utilities [5].	3
2.1	Niels Bohr model of the hydrogen atom radiating a photon.	7
2.2	Ionization factor α as a function of pressure p [11].	11
2.3	Distribution of charge carriers in an avalanche and their contribution to the applied uniform electric field $E_1 > E$; $E_2 < E$; $E_3 > E$ [12].	12
2.4	Breakdown voltage versus pressure spacing product pd for different gases [14].	15
2.5	Field distortion caused by space charges in an avalanche [14].	16
2.6	Statistical time lag t_l causes over-voltage then breaks down to a residual voltage V_r varying the discharge magnitude q for every PD [18].	17
2.7	Different field situations at DC voltage [19].	18
2.8	The accumulation of homocharge and heterocharge [21].	18
2.9	Equivalent circuit for <i>corona</i> discharges with \mathbf{c} representing the gas volume to break down [11].	19
2.10	Negative corona: Negative space charges shield sharp point [11].	19
2.11	Negative rod-plane breakdown and corona characteristics in atmospheric air [14].	20
2.12	Positive corona: Positive space charges cause periodic extinction of the discharge [11].	20
2.13	Positive hemispherical capped anode and plate cathode breakdown and corona characteristics in atmospheric air [14].	21
2.14	Voltage across a cavity in a solid dielectric [17].	22
2.15	Capacitive model of internal void [11].	23
2.16	Sequence of cavity breakdown under AC voltages [14].	23
2.17	Transient currents flowing through capacitive model during discharge [23].	24
2.18	Classic <i>abc</i> diagram extended with leakage resistances [18].	25
2.19	Recharging of a cavity by the dielectric current and the distribution of surface charges [21].	25
2.20	Partial discharges generated by DC voltage [18].	25
2.21	Equivalent circuit for <i>surface</i> discharges with \mathbf{c} representing the part of the surface that flashes over [11].	29
2.22	Spacer and potential distribution [29].	30
2.23	Charge phenomenon with metallic particle on spacer [35].	31
2.24	Conductive component inside a GIS.	32
2.25	Epoxy spacer supporting the conductor with an ineffective connection between conductor and spacer insert [36].	33
3.1	HVAC electric scheme.	36
3.2	Simplified diagram Heinzinger PNC 1000000 DC source [40].	37

3.3	HVDC electric scheme.	38
3.4	Basic coupling device in series with test object C_a [14].	38
3.5	Basic coupling mode in parallel with test object C_a [14].	38
3.6	Resonant parallel circuit connected to measuring device.	39
3.7	Schematic of a HFCT measuring an impulse current [43].	40
3.8	Major components of common PD measuring circuits [42].	41
3.9	Electric and magnetic field of a moving charge particle Q [44].	41
3.10	Electric field line distortion (kink) due to charged particle acceleration [45].	42
3.11	The components of the electric field at an arbitrary angle θ caused by an accelerated charge towards point A continuing to point C with constant velocity [46].	42
3.12	Representations of PD current pulses as a result of the Townsend and Streamer mechanism.	44
3.13	Normalized spectra of Gaussian PD current pulses.	45
3.14	Techimp PDBaseII acquisition unit.	46
3.15	Different visualizations of PD pulses.	46
3.16	Techimp PDBaseII intensity scale.	47
3.17	Agilent E4403B spectrum analyzer.	47
3.18	Tektronix DPO7354C Oscilloscope.	48
3.19	Electric circuit of the insulating transformer.	49
4.1	General PD monitoring scheme [3].	50
4.2	Derived data of pulse waveform.	53
5.1	The metallic component suspended from the inner conductor by fishing line.	56
5.2	Trends of the 95% discharge magnitude and 50 Hz repetition rate at different voltage levels.	57
5.3	Cycles of PD from a floating component at 20kV in 1.0 bar air.	58
5.4	Cycles of PD from a floating component at 70kV in 1.1 bar SF_6	58
5.5	Trend lines of the 95% discharge magnitude and repetition rate at different negative DC voltage levels 1.0 bar <i>air</i>	60
5.6	Time-resolved PD pattern of floating component at -58 kV in 1.0 bar <i>air</i> . .	61
5.7	Time-resolved pattern of rush of floating component PD activity at -58 kV in 1.0 bar <i>air</i> as shown in fig. 5.6.	62
5.8	DC recognition plots for discharges of a floating component at -58 kV in 1.0 bar <i>air</i>	63
5.9	Time-resolved PD pattern of floating component at 55kV in 1.0 bar <i>air</i> . . .	64
5.10	Floating component PD activity at -70 kV in 1.0 bar <i>air</i>	65
5.11	The epoxy spherical void components used for simulating internal discharges.	66
5.12	Trend lines of the 95% discharge magnitude and 50 Hz repetition rate at different voltage levels of spherical cavity sample.	67
5.13	Trend lines of the 95% discharge magnitude and repetition rate at negative DC voltage levels for a spherical cavity sample.	69
5.14	Time-resolved pattern of discharges in a spherical cavity sample at -30 kV.	69
5.15	DC recognition plots for discharges of a spherical cavity sample at -30 kV. .	70
5.16	Trend lines of the 95% discharge magnitude and repetition rate at positive DC voltage levels for a spherical cavity sample.	71
5.17	Time-resolved pattern of discharges in a spherical cavity sample at 30kV. .	71
5.18	DC recognition plots for discharges in a spherical cavity sample at 30kV. . .	72
5.19	The cylindrical spacer and components used for simulating surface discharges.	74
5.20	Trends of the 95% discharge magnitude and 50 Hz repetition rate at different AC voltage levels.	75

5.21	Trend lines of the 95% discharge magnitude and repetition rate at decreasing negative DC voltage levels for surface discharges over a cylindrical spacer.	79
5.22	Time-resolved pattern of surface discharge before flash-over at 63kV.	80
5.23	DC recognition plots for surface discharges before flash-over at 63kV.	80
5.24	Time-resolved pattern of surface discharge after flash-over at 60kV.	81
5.25	DC recognition plots for surface discharges after flash-over at 60kV.	81
5.26	Time-resolved pattern of surface discharge after flash-over at 57kV.	83
5.27	Time-resolved pattern of PD discharge train at 57kV.	83
5.28	DC recognition plots for surface discharges after flash-over at 57kV.	84
6.1	PD detection sensitivity affected by different factors [46].	87
6.2	RF signals and spectra of Streamer and Townsend discharges in internal cavity.	88
6.3	RF signal and frequency spectrum produced by a floating component discharge.	89
6.4	Relationship between RF signal floating component PD and apparent charge quantity.	90
6.5	RF signal and frequency spectrum produced by negative corona.	91
6.6	Relationship between RF signal negative corona and apparent charge quantity.	91
6.7	RF signal and frequency spectrum produced by positive corona.	92
6.8	Relationship between RF signal positive corona PD and apparent charge quantity.	93
6.9	RF Streamer discharge signal and frequency spectrum produced by internal discharges.	94
6.10	RF Townsend discharge signal and frequency spectrum produced by internal discharges.	94
6.11	Relationship between RF signal internal discharges and apparent charge quantity.	95
6.12	RF signal and frequency spectrum produced by a surface discharge.	96
6.13	Relationship between RF signal surface discharges and apparent charge quantity.	97
6.14	Separation of PD sources based on RF parameters.	98
6.15	Time-resolved PD pattern of negative corona.	99
6.16	DC recognition plots of negative corona using the RF parameter of frequency selection between 40 – 50 MHz.	99
A.1	Time and frequency domain of a signal[57].	104
A.2	Spectrum Analyser block diagram [57].	105
B.1	Frequency response of HF amplifier III.	107
B.2	Frequency response of HF amplifier IV.	108

List of Tables

2.1	Townsend primary ionization constants [39]	34
4.1	List of data directly measured by detection systems.	51
4.2	Derived data based on feature extraction of signal information.	52
5.1	Comparison of the inception voltages of floating components discharges for different gas formulations and distances to electrode.	57
5.2	Phase-resolved partial discharge patterns for a floating component in 1 bar air with distance of 4 mm from inner conductor.	59
5.3	Discharge magnitudes of floating components in 1.0 bar at different negative DC voltage levels. Detection by means of quadrupole calibrated according to <i>IEC 60270</i>	60
5.4	Phase-resolved partial discharge patterns for internal discharges in spherical cavity sample.	67
5.5	Discharge magnitudes of a spherical cavity sample at different negative DC voltage levels. Detection by means of quadrupole calibrated according to <i>IEC 60270</i>	68
5.6	Discharge magnitudes of a spherical cavity sample at different positive DC voltage levels. Detection by means of quadrupole calibrated according to <i>IEC 60270</i>	70
5.7	Comparison of the inception voltage for surface discharges over cylindrical spacer using different gas formulations.	73
5.8	Phase-resolved partial discharge patterns for surface discharges over cylindrical spacer in 1 bar air.	75
5.9	Phase-resolved partial discharge patterns for surface discharges over cylindrical spacer in 1.1 bar SF_6	76
5.10	Discharge magnitudes and repetition rate surface discharges over cylindrical spacer at increasing negative DC voltage levels. Detection by means of quadrupole calibrated according to <i>IEC 60270</i>	78
5.11	Discharge magnitudes and repetition rate surface discharges over cylindrical spacer at decreasing negative DC voltage levels. Detection by means of quadrupole calibrated according to <i>IEC 60270</i>	78
5.12	Discharge magnitudes and repetition rate surface discharges over cylindrical spacer at increasing positive DC voltage levels. Detection by means of quadrupole calibrated according to <i>IEC 60270</i>	82
5.13	Discharge magnitudes and repetition rate surface discharges over cylindrical spacer at decreasing positive DC voltage levels. Detection by means of quadrupole calibrated according to <i>IEC 60270</i>	82
6.1	Value of regression coefficient R and slope m of regression line for floating component discharges.	90

6.2	Value of regression coefficient R and slope m of regression line for negative corona discharges.	92
6.3	Value of regression coefficient R and slope m of regression line for positive corona.	93
6.4	Value of regression coefficient R and slope m of regression line for internal discharges.	95
6.5	Value of regression coefficient R and slope m of regression line for surface discharges.	96
6.6	Selection of regression line slopes m of RF parameters to the apparent charge for multiple insulation defects.	100
6.7	Regression coefficients R of RF parameters to the apparent charge for multiple insulation defects.	101

Nomenclature

α	Townsend primary ionization coefficient
ϵ	Permittivity
η	Electron attachment coefficient
Γ	Townsend second ionization coefficient
λ	The mean free path
ν	Phonon frequency
$\bar{\alpha}$	Effective primary ionization coefficient ($\alpha - \eta$)
ρ	Resistivity
σ	Specific conductivity
eV _i	Ionization energy
eV	Unit of energy equal to approximately $1.6 \cdot 10^{19}$ J
E_{crit}	Discharge inception electric field
h	Planck's constant
$h\nu$	Photon energy
N_0	Number of initiatory electrons
q	Discharge magnitude
T	Equivalent time-length
t_l	Time lag to breakdown after reaching minimum breakdown voltage
t_r	Recovery time
U_{bd}	Breakdown voltage of a gas gap between metal electrodes obtained from Paschen curve
U_i	Discharge inception voltage
V_{min}	Minimum breakdown voltage
W	Equivalent Bandwidth
W_k	Kinetic energy
E	Electric field strength
e	Atomic charge
p	Gas pressure

Chapter 1

Introduction

1.1 Motivation

Electricity is regarded as the most important energy source in modern society. The correct operation of many electric facilities is dependent upon the quality of the power from the grid. The quality of the delivered power should be as stable as possible to meet the requirements of the electric equipment. Nowadays, many electricity consumers expect continuous power supply and the costs associated with failure to delivery can be great for both the consumer and the transmission system operator.

This illustrates the importance of protecting and monitoring power systems which are one of the most intricate systems. Determining the condition by monitoring of the transmission network to execute preventive maintenance whenever necessary gains more and more importance to circumvent the occurrence of a failure of the component.

Compared to the many methods for determining the condition of power systems the detection of PD is considered as one of the most promising solutions for monitoring and the detecting possible insulation defects in the components of the power system before a fault occurs.

GIS which are considered fundamental nodes within the modern transmission network is one of these components. Condition monitoring for GIS has been extensively researched under High Voltage Alternating Current (HVAC) conditions, but there still is a scarcity of research done on HVDC with very few recent studies.

HVDC is not a new technology as it has been used to interconnect the Scandinavian grid to mainland Europe through the North and Baltic seas going back to the year 1954. There is however an energy transition as DC solutions are used for renewable energy integration (e.g solar energy systems) and charging of electric vehicles. One of the fastest-growing markets in the utility sector however is the transmission of energy using HVDC [1]. Consumer centers are increasingly more supplied with sustainable electricity over very large distances. These increasing distances that result in high losses for HVAC render the transport through conventional trusted methods disadvantageous.

In order to be able to exploit the advantages of HVDC technology, a stable network is necessary. Standardization of HVDC technology has to be agreed upon and major technical gaps need to be plugged. The assessment of the condition of the power network is a valuable tool for evaluation of this technology. This thesis focuses on the recognition of defects that might take place within HVDC GIS by means of electrical detection of PD.

1.2 HVDC Gas Insulated Systems

A well known variant of the GIS is the gas insulated substation which is a collection of gas-insulated transformers, switchgear, shunt reactor and much more, combined together

to control the distribution of power in high- and medium-voltage networks. Traditionally these substations used to be air-insulated, but the decision to enclose the voltage-carrying parts of the substation and the use of gas insulation (e.g. SF_6) have led to higher reliability and an insulated system unaffected by environmental conditions. The gas insulation makes it possible to shorten the distance between voltage-carrying parts resulting in compact space saving designs.

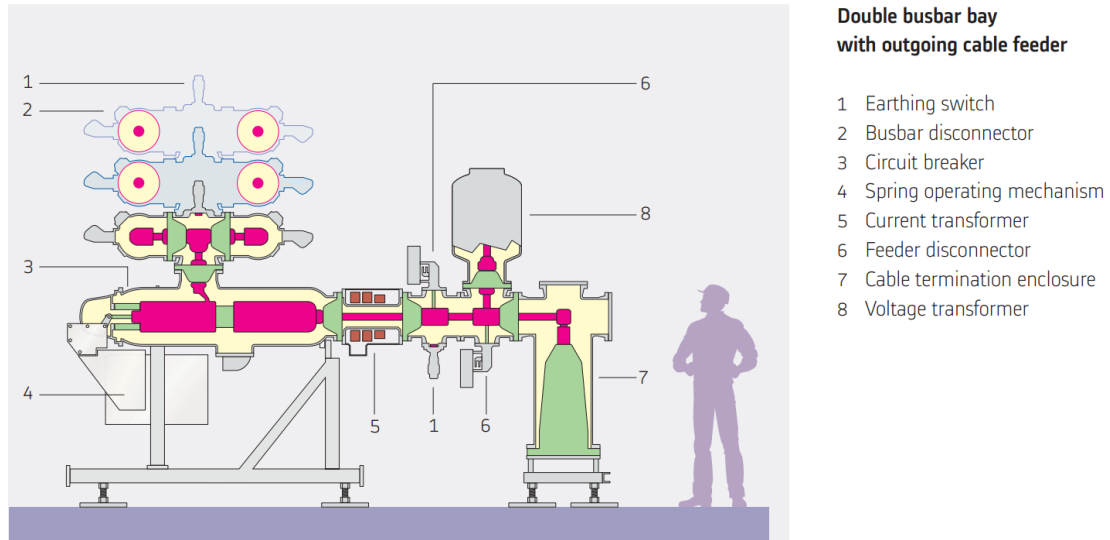


Figure 1.1: Cross-section view of Gas-Insulated Substation [2].

The advantages of the GIS make it the preferred option for installing gas insulated substations in densely populated urban areas. The compactness and flexibility of GIS substations allow for installation close to load centres, allowing for more efficient configuration of the HV system and the MV distribution network.

During the operation of the GIS, defects into the insulation system can be accidentally introduced. These defects most likely originate from undesired moving metal particles inside the GIS or due to vibrations [3, 4].

The main causes of dielectric failure in the GIS according to a service experience study [5] on several GIS with AC operating voltages of either 123 or 420 kV are portrayed in fig. 1.2. Deficiencies in the insulation coordination of disconnectors and earthing switches result in a big portion of the failures, while the major cause of failures is due to defects subjected to high electric fields resulting in PDs. The principal PD sources responsible for failures of GIS are:

- Fixed protrusions
- Free moving particles
- Electrically floating components
- Particles on spacer surface
- Voids in insulators

The failures as a result of these sources could have been prevented by monitoring PDs with a detection system with sufficient sensitivity and planning a maintenance accordingly as these failures are all preceded by detectable PD activity [5]. Although no investigation has been done so far on the severity of the PD sources on GIS operated at HVDC, it is widely accepted that PD has a detrimental effect on both HVAC and HVDC.

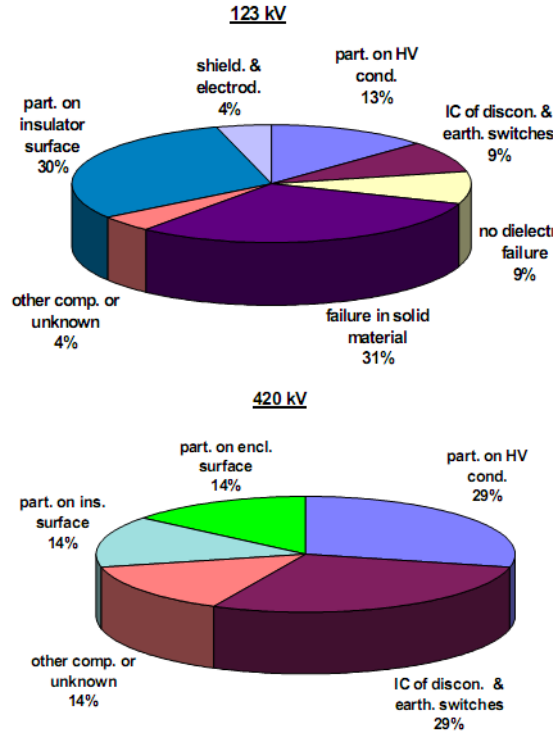


Figure 1.2: Cause of dielectric failures in 123 kV and 420 kV GIS based on a study of German utilities [5].

1.2.1 PD sources in GIS

Fixed Protrusions

During manufacturing of the GIS protrusions fixed to the High Voltage (HV) conductor (HV protrusion) or the enclosure (Low Voltage (LV) protrusion) can be created (e.g. scratches). During operation of the GIS free moving particles can also be welded to a fixed protrusion.

Protrusions fixed to the enclosure result in less PD activity compared to protrusions on the high voltage conductor. The electric field intensity at the conductor is usually higher than near the enclosure [4].

Nevertheless, both protrusions can be very dangerous because the electric field strength is enhanced locally distorting the field distribution. PDs in the form of corona take place leading to electrical losses and causes by-products in SF_6 which may attack and degrade the insulation construction reducing the insulation strength. The lowered insulation strength in combination with sudden changes by lightning and switching impulses increase the possibility of a breakdown [6].

Free Moving Particles

A loose conducting particle inside a GIS is most likely in contact with the outer conductor of the GIS. The particle creates a local perturbation on the surface of the electrode. When it is energized, the electric field is locally distorted and the conducting particle acquires charge according to the induced charge distribution which is determined by the shape, location and orientation of the conducting particle [7, 8].

The particle starts to move and even lift off when the Coulomb force exceeds the gravitational force and could move to a more critical area such as the inner conductor or a spacer.

Electrically floating components

The potential of an electrically floating component is determined by the relationship between its capacitance to the conductor versus that to the ground. In the case that the potential exceeds the insulation strength of the insulating gas between either the conductor or the ground, a relatively large discharge will take place [9]. This type of PD produces pressure waves in the gas mixture which can easily be detected by acoustic sensors.

An example of a floating component is a stress shield of which the contact to the electrode has deteriorated. The partial discharge taking place is very energetic because the gap that breaks down usually has a very high capacitance. The contact degrades further from which metallic particles can be produced [10]. The same type of discharge also occurs in the case of *Floating Electrodes* in which the potential difference between adjacent electrodes results in a partial discharge or when metallic inserts usually embedded into epoxy spacers have bad contact to the conductor.

Particles on Spacer Surface

The movement of a free moving particle near a dielectric insulator surface is affected in such a way that the particle can attach to the insulator surface. The electric field strength enhances as a result of the protrusion and a flash-over along the surface can be triggered more easily [7].

Void in insulator

Voids in insulators result in inclusions of low dielectric strength in the form of unwanted gas-filled cavities. Partial discharges can occur at normal operating voltage in these cavities that are the cause of a slow erosion progress of the material, which eventually leads to a breakdown.

1.3 Thesis Overview

The thesis consists of 7 chapters. The first chapter will explain the background, motivations and the general overview of the thesis. Chapter 2 is a literature review describing the physics behind the creation of PDs. The conditions necessary for the occurrence of PDs are covered in addition to an analysis of the different types of PD in GIS ranging from corona, internal, surface and discharges due to electrically floating components for both AC and DC voltage. Chapter 3 presents the equipment available at TUDelft HV laboratory to create the set-up used for applying AC and DC voltages to the test object. The PD monitoring configuration are covered categorizing conventional and unconventional methods. Chapter 4 deals with signal processing of the PD data for classification of PD sources. Some quantities on which the analysis can be based, are discussed. Furthermore a distinction of quantities which are directly measurable by detection systems as *direct data* and the quantities or *derived data* derived through combinations or data analysis, will be made. In chapter 5, PD measurements using the conventional method of created defects in the HV laboratory are discussed. The defects are used to simulate insulation defects and the measurements in DC are analysed resulting in recognition graphs used for differentiating between the possible defects. Chapter 6 discusses the results of simultaneous measurements of PDs using the conventional method and RF techniques. The combined PD measurements on multiple defects are used to create plots of RF quantities to apparent charge. These plots are used for quantification of the relationship between the different techniques. Lastly, chapter 7 concludes the study and suggests future research related to the measurement of PDs in HVDC GIS using electrical partial discharge detection.

1.4 Thesis Objectives

The main objective of this research is to detect and recognize the presence of PDs in a GIS under DC voltage. To this end, electrical detection of the PD with sensors measuring PD based on the energy induced in the circuit, and the Ultra High Frequency (UHF) detection of Electromagnetic (EM) waves radiated at discharge activity are used.

The sensors were applied to detect the PD data. The data was analysed to recognize and distinguish the different types of PD created by GIS defects.

PD defect sources are created to mimic real insulation defects that might occur inside a GIS. The standardized procedure IEC 60270 of PD measurement has the advantage of calibrated measurements that can be used for more accurate classification of the defects. This method of measurement is only applicable off-line which implies turn-off costs and limited capabilities in effective maintenance strategies.

On-line PD monitoring of GIS using the UHF technique is already used for AC. To extend this technique to recognize insulation defects at DC voltage is the ultimate goal.

The specific primary objectives of this thesis are:

1. To investigate and interpret the physical behaviour of different PD types, namely corona, internal, surface and discharges due to floating components that can occur in a GIS in AC and DC.
2. Detection and measurement of the different types of PD in DC and the recognition of the PD types through analysis of the measurements.
3. To demonstrate the technique of the application of a UHF sensor to detect the different PD sources in a GIS whilst determining the limitations and potentialities of the UHF method for the recognition of PD under DC.

Chapter 2

Partial Discharge Phenomena in GIS

The dielectric medium inside a GIS, apart from the insulating spacers, is mainly composed of a gaseous dielectric in the form of an *insulating gas*. This gas contains plenty of free electrons as a result of the ion generating processes named *ionization* which constantly takes place in the gas. This ionization can be due to processes like external radiation, collisions between thermally excited gas molecules or as a result of *electron emission* from the metal surfaces of the electrical equipment to name a few.

The free electrons generated by these processes are critical for the initiation of a discharge as they are accelerated in the direction of the electric field. Along this path collisions with gas molecules occur leading to further ionization. This repetitive process leads to a multiplication of electrons, the so-called electron *avalanche* which results in a transfer of charges.

Dependent upon several conditions, two different mechanisms can lead to a discharge in a gaseous dielectric bridging the gas gap; The *Townsend-like* and *Streamer-like* discharge mechanisms.

The type of insulation defect combined with these discharge mechanisms result in discharges in the gas, solid insulator and the gas-dielectric interface. These PDs are explained in terms of *corona*, *internal discharges*, *surface discharges* and *floating component* initiated discharges.

2.1 Partial Discharge Physics

2.1.1 Ionization

The atomic structure of gas atoms can be described by the atom's model of Bohr-Rutherford in which the electrons follow orbits of different radius named shells around the nucleus. These shells are characterized by a set energy level and openings for orbiting electrons in which electrons from the outer shells have higher average energy than those in inner shells. An atom must acquire more energy in order for an electron to move from an internal to an external shell, while energy releases in the other way around.

The energy required for an electron to move from one shell to a higher energy shell is measured in electron-volts [eV]. For the atom to lose an electron from its outer shell, the maximum energy must be absorbed by the atom, named the ionization energy eV_i .

Ionization by collision

Ionization of unexcited atoms or molecules by electron impact is the principal mechanism of charge production in gas discharges. The applied electric field accelerates free electrons

in the direction of the field until a collision with a gas molecule takes place. The kinetic energy W_k of the accelerated electron is proportional to the mean free path λ , the statistical average distance between successive collisions which is inversely proportional to the gas pressure p .

$$W_k = eE\lambda \propto e \frac{E}{p} \quad (2.1)$$

The collision between the electron and the atom or molecule results in an exchange of kinetic energy. Based on the effect of the energy transfer, two types of collisions are identifiable:

1. **Elastic collision** has no loss of kinetic energy. No excitation or ionization takes place.
2. **Inelastic collision** happens when the gas atom or molecule absorbs enough kinetic energy from the collision with the incident electron to become either excited or ionized.

Excitation of an atom or molecule is only possible if the energy transferred to the atom or molecule is at least as high as the excitation energy eV_a representing the least amount of energy necessary for moving an orbital electron to a higher energy shell. This excitation energy differs between atoms and is in the order of a few eV . The process of excitation is represented by eq. (2.2).



A represents an atom and e the incident electron with kinetic energy. The energy transfer results in A^* , the atom in excited state. This state however is unstable and the atom reverts back to a lower stable state in less than a μs . The excited orbital electron will fall back to a lower energy shell and energy in the form of a single quantum of radiant energy called a photon is released represented by eq. (2.3). The photon energy is described by $h\nu$ with h the Planck's constant and ν the frequency of the radiation [11].



A visualization of formula eq. (2.3) by the Bohr-Rutherford model for a hydrogen atom is shown in fig. 2.1. In the case, that the transfer of kinetic energy is equal or higher than

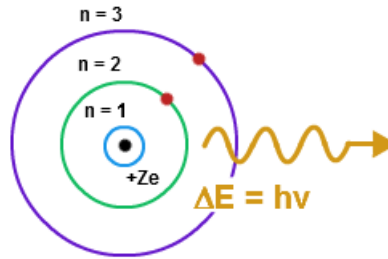


Figure 2.1: Niels Bohr model of the hydrogen atom radiating a photon.

the ionization potential eV_i of the atom, an orbiting electron of the atom is excited beyond the energy levels and is liberated from the atom resulting in another free electron e and a positive ion A^+ as shown in eq. (2.4).



Ionization energy eV_i also differs for the different gases used as insulation with for e.g. 15,5 eV for nitrogen and 12,2 eV for oxygen.

Photo ionization

Ionization through photons does not only occur due to the radiation emitted when excited atoms in the insulating gas return to their ground state. External radiation in the form of cosmic rays, x-rays and nuclear radiation also take place as most of these rays are able to penetrate through most conventional walls [12]. These travelling photons contain an energy content $h\nu$ and in the case of collision with a gas atom this energy is transferred. Ionization of the atom only takes place if the photon energy meets the requirement of eq. (2.5).

$$h\nu \geq eV_i \quad (2.5)$$

The resulting process of photon ionization can then be represented by eq. (2.6).



In the case of high-energy photons colliding with a gas atom, enough energy can be absorbed by an orbiting electron from the inner shells to become ionized. The missing electron will then be substituted by one of the next higher level for a more stable situation. This substitution is accompanied by the energy release in the form of photon energy less than the incident energy of the high-energy photon, but still able to excite or even ionize other atoms.

Thermal ionization

Heating gas to a sufficiently high temperature results in disassociation of its molecules into atoms. The higher temperatures also translate into more kinetic energy for the atoms resulting in a more chaotic movement. Collisions between the gas atoms start to occur and two processes along with it:

1. **Ionization** of the atom due to the kinetic energy transferred in the collision being higher than the ionization energy eV_i .
2. **Excitation** of the atom in the case of the collision not being energetic enough. The energy freed when going back to the ground state is in the form of radiated photons. Photon ionization of other atoms becomes possible.

In the case of flames and high pressure arcs, thermal ionization is the main source of ionization.

Ionization by metastable pieces

Certain atoms like those of inert gases and some of the elements in group II of the periodic table are able to achieve lifetimes of seconds for their atoms in metastable state in comparison to lifetimes of far below μs for other atoms. The metastable state is the state in which an orbital electron is excited to a higher energy level before reverting back to a lower more stable energy level [12]. These states are represented by A^m and are associated with energies eV^m . During this lifetime, these metastable atoms A^m or meta-stables can collide with another atom B and if its energy eV^m exceeds the ionization energy eV_i the reaction as shown in eq. (2.7) may occur.



For cases with $V^m < V_i$ the reaction would only result in excitation of atom B. Higher densities of meta-stables make collisions between them more likely to occur. Whenever the combined metastable energy exceeds the eV_i for one of the atoms, ionization of one of the

atoms will take place. A metastable atom could also be ionized when absorbing a photon as shown in eq. (2.8). The cumulative energy of both exceeds the ionization energy.



As ionization by metastable interaction comes into play long after the excitation of atoms it has been shown through research that these reactions are responsible for the long time lags of discharges observed in certain types of gases [13].

Ionization by nuclear particles

Nuclear radiation includes the radiation of α and β particles, as well as photons of γ rays. The radiated photons ionize in the same way as in photo ionization, while the particles will ionize by particle to gas atoms collision.

The ionization effects of particles heavier than electrons can be considered by applying the principles of elastic and inelastic collisions of which the most important particles are the protons and α particles. The direction of travel is barely influenced by the collisions because of the heavy mass of the particles.

Electron emission from electrodes

The electrodes inside the GIS consist of a metallic lattice composed out of positive ions in a sea of mobile valence electrons held together by a force between these electrons and positive ions called the metallic bond. Under normal circumstances a *potential barrier* keeps the valence electrons from separating from the metallic lattice. A minimum energy called *work function* of the metal must be exceeded before separation from the metallic lattice can take place. The work function lowers when the metallic surface is subjected to a strong electric field, making it possible for such a valence electron to overcome this energy barrier and escape through the surface of the metal. External factors that enhance the electron emission of metallic surfaces are:

1. **Low field strength** also lowers the work function of the metal. The energy necessary to overcome the potential barrier could be complemented by energy transfer from colliding ions accelerated by the electric field, heating of the metal (*thermionic emission*) or by bombardment of photons (*photoelectric emission*).
2. **High field strength** can decrease the barrier to such an extent that no external source of energy is necessary for field emission.
3. **Tunneling** the quantum mechanical effect of an electron passing through the potential barrier of the work function of the metal while lacking the necessary energy to surpass this barrier.

Protrusion and whiskers on the metal surface can enhance the local field up to 50 times the unaffected electric field [11]. Polishing and cleaning the equipment's surface is thus of utmost importance to avoid field emission as much as possible.

2.1.2 De-ionization

In the gas medium a concurring process to ionization takes place, called de-ionization. The free electrons are captured removing fast moving charge carriers from the gas medium. The mechanisms are described below.

Recombination

Negatively and positively charged particles have a chance for recombination into a more stable form whenever in the vicinity of one another. The potential energy and the relative kinetic energy of the recombining electron-ion or ion-ion pair is released as a quantum of photon radiation:



The e^- can also be a negative ion resulting in a ion-ion pair.

The rate of recombination is directly proportional to the concentrations of the positive (n_+) and negative ions or electrons (n_-). Higher pressures that lead to greater concentrations of the ions also result in a larger recombination rate.

Electron attachment

In gaseous state, certain neutral atoms and molecules can attach to a free electron to form a stable negative ion. These atoms or molecules are lacking one or two electrons in their outer shell to make this combination possible and are known as the electronegative gases.

Electronegative gases have the property of negative ion stability. A negative ion is stable for a longer period of time because the total energy of the negative ion is even lower than the atom in ground state.

The difference in total energy between the negative ion and the unexcited neutral atom is the *electron affinity* of the atom. Upon attachment this amount of energy is released either as photon or kinetic energy.

There are several methods of negative ion formation through attachment of which a few are:

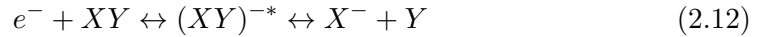
1. *Radiative attachment*: when the excess energy releases as a quantum upon attachment. Such a process is also reversible resulting in



2. *Attachment through three-body collision*: when the excess energy released upon attachment is acquired as kinetic energy W_k upon collision with a third particle.



3. *Dissociative attachment*: in the case of the excess energy upon attachment is used within a molecule to separate into a neutral particle and a negative ion.



The negative ions created upon attachment play an important role in the partial breakdown of technically interesting gases as shall be explained later in *corona discharges*.

The suppression of electrons from an ionized gas by attachments is expressed by the *attachment coefficient* η . The attachment coefficient is the number of attachments produced in the path of a single electron travelling a unit distance in the direction of the field.

De-ionization by diffusion

A non-uniform concentration of ions leads to a movement of ions from regions of higher concentration to a region of lower concentration to achieve an equilibrium. This process of diffusion has a de-ionizing effect in the regions of higher concentrations while at the same time an ionizing effect in the regions of lower concentration.

2.2 Breakdown Mechanisms in Gas

Depending on the gas pressure and the distance between electrodes, two different breakdown mechanisms are possible in a gas, namely:

1. **Townsend mechanism**
2. **Streamer mechanism**

Prior to breakdown a multiplication of electrons takes place called an avalanche which will be discussed in more detail.

2.2.1 Pre-breakdown phenomena in gases

Townsend primary ionization coefficient α

The different types of ionization all result in free electrons in gas that especially inside the GIS will experience an electric field. The ionizations by electron impact will become the principal mechanism of charge production in gas discharges. Therefore the *ionization factor* or *first Townsend ionization coefficient*, α is introduced that equals to the average number of ionizations per cm in the field direction as a result of ionization by electron impact. Taking into account that each ionization is a new electron, the ionization factor can then be described by eq. (2.13) [11].

$$\alpha = \frac{\text{number of electrons}}{\text{cm in the field direction}} \quad (2.13)$$

The ionization factor α is proportional to the gas pressure p because the number of collisions are proportional to the concentration of molecules per unit of volume. However, for ionization to take place, the kinetic energy of an electron as shown in eq. (2.1) should also exceed the ionization energy during collision. The mean free path λ of the electron is inversely proportional to the molecule concentration in gas, thus also inversely proportional to the gas pressure p .

Writing the ionization factor as a function proportional to the gas pressure results in eq. (2.14).

$$\alpha :: pf(W_k) = pf\left(\frac{E}{p}\right) \quad (2.14)$$

For many gas types this relation can be visualized according to fig. 2.2.

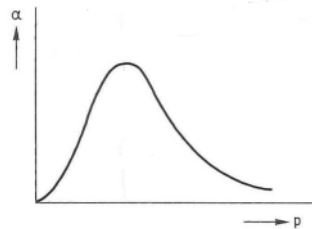


Figure 2.2: Ionization factor α as a function of pressure p [11].

At a certain pressure level the optimal ionization takes place. Below this level the ionization factor α drops along with the number of molecules for collisions to take place. Pressures above this level result in shorter mean free paths making the kinetic energy of the collisions less energetic.

The de-ionization processes capture free electrons as they travel along the electric field. Because of this, the available electrons cannot only be explained by the ionization factor,

but must also take into account η , the number of attachments produced in the path of a single electron travelling a unit of distance in the field direction.

$$\eta = \frac{\text{number of captures}}{\text{cm in the field direction}} \quad (2.15)$$

The effective ionization factor $\bar{\alpha}$ as a result can thus be calculated according to:

$$\bar{\alpha} = \alpha - \eta \quad (2.16)$$

Generation of electron avalanches

With only one or a few starting electrons available in the gas, accelerated in the direction of the field is enough for creating an *electron avalanche*. The accelerated movement of a starting electron ends in a collision with a gas molecule that can lead to ionization and an extra available free electron leaving behind a positive ion. The new electron together with the initial electron proceed along the field repeating the process of ionization. At a distance of x along the electric field, initial starting electrons N_x create an additional dN_x free electrons through ionization according to the effective ionization factor $\bar{\alpha}$ as shown in eq. (2.17).

$$dN_x = N_x \bar{\alpha} dx \quad (2.17)$$

In a uniform field with constant $\bar{\alpha}$ with an initial number of electrons N_0 the total amount of free electrons at distance x from starting point along the electric field becomes:

$$N_x = N_0 \exp(\bar{\alpha}x) \quad (2.18)$$

The number of electrons increases exponentially, and as they scatter somewhat in sideways direction, the avalanche increases also in thickness. Every ionization results in a fast moving electron, but also a much slower positive gas ion.

The avalanche consists at a given moment by the fast moving electrons in the head drifting towards the anode, while its wedge shaped tail, due to the diffusion of the electron swarm consist of the much slower positive ions drifting slowly towards the cathode as shown in fig. 2.3.

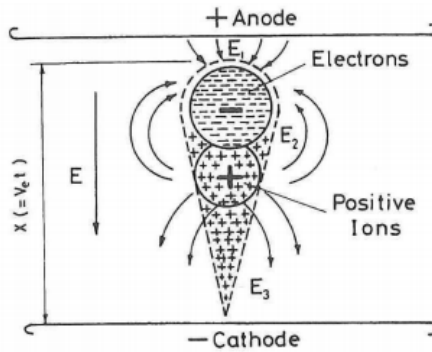


Figure 2.3: Distribution of charge carriers in an avalanche and their contribution to the applied uniform electric field $E_1 > E$; $E_2 < E$; $E_3 > E$ [12].

Feedback process

The avalanche finishes when the ions have entered the cathode. Avalanches by themselves do not cause breakdown, but will only result in leakage currents in the insulating medium.

For a breakdown to occur, the avalanche needs successor avalanches that need a *feedback* process to release their starting electrons called *secondary electrons*. The feedback process is initiated by secondary ionizing mechanisms as for example ionizations by secondary ionizing agents like positive ions accelerated towards the anode, excited atoms, photons or metastables.

The secondary ionizing agents are quantitatively presented by a coefficient defined as the average number of secondary electrons produced. Γ is called Townsend's second ionization coefficient and its magnitude depends on the type of gas, the electrode material and in part also to the function of $\frac{E}{p}$ in the same way as we had seen for α before, but with much smaller magnitude. From this we can calculate number of secondary electrons produced at the cathode during the life of the first avalanche by

$$N_0\beta = \Gamma(e^{\bar{\alpha}d} - 1)N_0 \quad (2.19)$$

The new electrons start the second generation of avalanches subsequently followed by another generation of avalanches resulting in a series of electron growth.

$$N_0 + N_0\beta + N_0\beta^2 + N_0\beta^3 + \dots \quad (2.20)$$

In the case that β grows larger than 1 this series will grow to infinite free electrons meaning that the gas *breaks down*. The condition for breakdown is thus defined by eq. (2.21).

$$\bar{\alpha}d > \ln(1 + \frac{1}{\Gamma}) \quad (2.21)$$

Townsend second ionization coefficient Γ

The Townsend second coefficient Γ represents a combined effect of several feedback mechanisms for the creation of secondary electron. To explain how this coefficient is calculated, two feedback mechanisms are treated more in-depth.

- **Feedback by positive ions** occurs when the positive ions of the avalanche are accelerated by the electric field towards the cathode. Upon collision with the cathode, a *secondary electron* is released with probability γ and has the ability to start avalanches. A feedback mechanism in which the original N_0 starting electrons leaving the cathode results in $N_0 \exp(\alpha d)$ electrons reaching the anode. During this process a formation of positive ions according to $N_0[\exp(\alpha d) - 1]$ takes place that collide with the cathode releasing secondary electrons according to:

$$N = N_0\gamma[\exp(\alpha d) - 1] \quad (2.22)$$

Every secondary electron could be responsible for a new avalanche.

- **Feedback by photo-effect** is the result of the photons from excited atoms reaching the cathode and releasing photo electrons. In the same way as we have defined the ionization factor α , the factor with which an excited atom will transmit a photon θ is:

$$\theta = \frac{\text{number of released photons}}{\text{length of path } \Delta x} \quad (2.23)$$

Not all photons are directed towards the cathode resulting in a maximum possible amount of photons reaching the cathode (θg). And of these photons the gas will absorb part μ so that the number of photons decrease by

$$\exp(-\mu x) \quad (2.24)$$

moving towards the cathode. The number of collisions with the cathode finally releases δ *photo electrons* that can start the avalanche process again as *secondary electrons*. Combining these processes together it is possible to state that with N_0 starting electrons from the cathode the number of secondary electrons by this process is

$$N = N_0 \frac{\theta g \delta}{\alpha - \mu} [\exp(\alpha - \mu)d - 1] \quad (2.25)$$

which can be rewritten with $\frac{\theta g \delta}{\alpha - \mu}$ as γ and if $\mu \ll \alpha$ to the well known:

$$N = N_0 \gamma [\exp(\alpha d) - 1]$$

Describing all the feedback mechanisms that take place in a gas in the same way and taking into account that every mechanism experiences ionization and de-ionization processes differently it is possible to retrieve the factor Γ as a combination of these mechanisms for which the condition for breakdown eq. (2.21) holds.

2.2.2 Townsend mechanism

The Townsend mechanism requires three stages to initiate breakdown of the insulating gas between the electrodes:

1. Creation of a *starting electron*.
2. Multiplication electrons leading to an *avalanche*.
3. *Creation of secondary electrons* by a feedback process.

The Townsend mechanism has its secondary electrons released from the cathode when ion or photon collision takes place. Avalanches starting at the cathode make their way towards the anode.

Paschen's law

Equation (2.21) shows the condition for breakdown as a result avalanches with a feedback mechanism. Rewriting results in the criterion for breakdown called the *Townsend criterion*.

$$\Gamma(e^{\alpha d} - 1) = 1 \quad (2.26)$$

Rewritten the Townsend criterion becomes:

$$\alpha d = \ln 1 + \frac{1}{\Gamma} \quad (2.27)$$

The breakdown condition is thus dependent on the critical values of the Townsend's first and second coefficient α and Γ , with α a function of the electric field $E = \frac{V}{d}$ and the gas pressure p and Γ a constant per gas type.

$$\alpha = p f\left(\frac{E}{p}\right) \quad (2.28)$$

Equation (2.27) can thus be rewritten to eq. (2.29).

$$p \cdot f\left(\frac{E}{p}\right) d = \text{constant} \quad (2.29)$$

The breakdown voltage is thus in terms of gas pressure p and electrode separation d and the breakdown voltage V_{bd} the same for every given value of pd so that the relation can be written as

$$V_{bd} = f(pd) \quad (2.30)$$

which is the well-known Paschen's law. From this relation, the visual representation of the breakdown voltages of gases as a function of pressure time distance, pd , correspond to curves as shown in figure fig. 2.4.

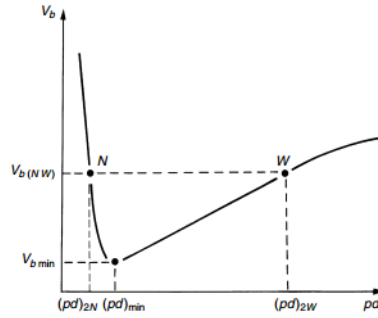


Figure 2.4: Breakdown voltage versus pressure spacing product pd for different gases [14].

The Townsend criterion does not seem to hold at high pressures and/or large electrode distance. The Paschen's curve must not be used for pd exceeding $1 \text{ atm} * 5 \text{ mm}$ [11] as then another breakdown mechanism takes over.

2.2.3 Streamer mechanism

The validity of the Townsend mechanism does not hold if the pressure or distance between electrodes is increased over $5 \text{ atm} * \text{mm}$. Characteristic differences take place between the breakdowns subjected to these conditions:

- The **time to breakdown** is too short to have been derived from the Townsend mechanism. Within the time of breakdown the slow moving ions cannot have reached the cathode yet to create secondary electrons.
- The **breakdown voltage** is not influenced by the cathode material, thus the feedback by the γ mechanism is not necessary for breakdown.
- The **breakdown channels** are sharp and narrow instead of diffuse as expected from the Townsend mechanism.

To explain these differences, the theory of the *streamer* mechanism has been independently developed by Raether, Meek and Loeb [15, 16]. The theory is based on the idea that the space charge formed in the avalanche starts to effect the electric field if it surpasses the critical length.

The number of ions in an avalanche increases exponentially towards the anode. The slow moving ions are still at the spot where they are formed when the electrons have already vanished forming a high concentration of positive ions at the tip of the avalanche superimposing an electric field onto the background electric field. If more than 10^8 ions are present, the electric field is greatly enhanced resulting in extra ionization and creation of photons taking place. The photo-ionization in adjacent gas atoms take place forming avalanches in the vicinity that merge with the main channel, *the streamer*, that gradually grows towards the cathode. Approaching the cathode, an intense electric field causes a burst of secondary and emission electrons bridging the gap. A mixture of the positive gas ions and the negative electrons form a conductive path breaking down the gas gap.

Two types of streamers can be formed when the critical concentration of ions is reached. There is the possibility of an **anode initiated streamer** where the positive avalanche reaches the anode and the residual space charges lead to enhancement of the electric field in

such a way that extra ionization and creation of photons cause nearby positive avalanches that combine with the streamer to bridge the gap.

The **mid-gap streamer** advances as an avalanche across the gas gap as seen in fig. 2.5. The enhanced field initiates avalanches on both sides of the streamer that help bridge the gap.

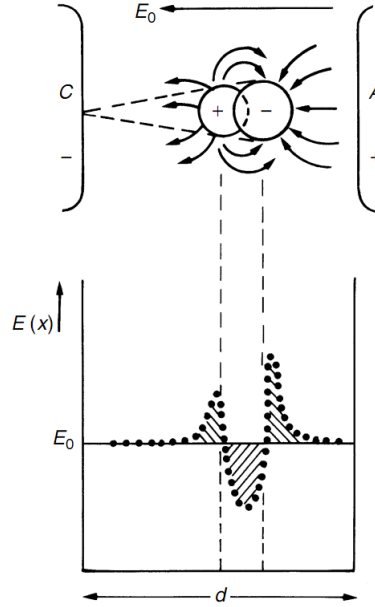


Figure 2.5: Field distortion caused by space charges in an avalanche [14].

The feedback mechanism in streamers depend on *secondary electrons* released in close vicinity of the streamer instead of starting electrons released at the cathode as is the case for the feedback mechanism for the Townsend discharges.

2.3 Partial Discharges in GIS

2.3.1 Partial discharge conditions

Partial discharges are caused by the *ionization* processes induced by the electric field in the insulation defect. The ionization process produces electron avalanches which do not necessarily develop into a PD. An avalanche develops into a PD whenever the growth of this avalanche by one of the discharge mechanisms grows enough in size to bridge the gap. This becomes possible if the local field exceeds a critical value, E_{crit} . In short, whenever the local field is below E_{crit} electron avalanches can occur, but will not develop into PD.

The development of PD due to a defect must satisfy two conditions:

- A starting electron is available;
- The local electric field exceeds the critical value.

The starting electrons can be supplied by external radiation or by previous discharges. The availability of starting electrons is based on a stochastic process [17] and therefore a time lag t_l occurs for an avalanche to take place after the local field reaches the critical value.

An important concept is the *inception* voltage U_i of a PD activity defined as the applied voltage at which repetitive PD are first observed in the test object. This voltage

corresponds directly to an applied field, which at the defect becomes specific value of the local field.

The defect enhances the local electric field E_i with a field enhancement factor f in comparison to an electric field where no defect is present E_0 . Equation (2.31) shows this enhancement.

$$E_i = f \cdot E_0 \quad (2.31)$$

The field enhancement factor depends in general on the relative permittivity of the dielectric which surrounds the defect and the shape of the defect.

In the event of a discharge, the local field is subjected to a drop as expressed by eq. (2.32),

$$\Delta E = E_i(t^-) - E_i(t^+) \quad (2.32)$$

with t^- and t^+ the times at which the PD respectively begins and ends. The magnitude of the PD is proportional to the drop in field as expressed by eq. (2.33) which explains the varying discharge magnitudes for partial discharges as the time lag t_l can lead to over-voltages and the defect drops to a non-constant residual voltage V_r before the discharge ceases as seen in fig. 2.6.

$$q \propto \Delta E \quad (2.33)$$

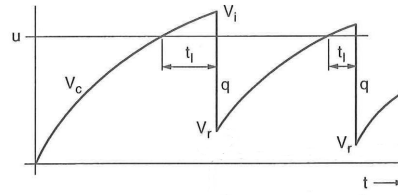


Figure 2.6: Statistical time lag t_l causes over-voltage then breaks down to a residual voltage V_r varying the discharge magnitude q for every PD [18].

2.3.2 DC electric field

The electric field in DC behaves different from AC conditions as the effect of space charges must be taken into account. The electric field at DC voltage, E_{DC} , across a dielectric, can be approached according to:

$$E_{DC} = E_\epsilon + E_\rho \quad (2.34)$$

with E_ϵ the field distribution inside the dielectric according to the permittivity, while E_ρ is the field as the result of accumulated space charge. Applying a DC voltage across a dielectric varies the electric field distribution within the insulation over the course of time before reaching a stabilized state.

Immediately after switching the voltage on, the insulation is stressed in an AC manner given by the voltage distribution according to the permittivity. This stage is named the **capacitive stage** and discharges during this stage can be calculated in the same way as for AC resulting in a value for E_ϵ .

Before reaching a steady DC field a transition period takes place between t_0 and t_1 as a result of the space charges influencing E_ρ as shown in figure 2.7. After charge accumulation has finished and only a steady DC field is left, a pure resistive field occurs in the **resistive stage**. The field E_{DC} is determined now by the distribution of the specific conductivity σ .

$$E_{DC}(t > t_1) = E_\sigma \quad (2.35)$$

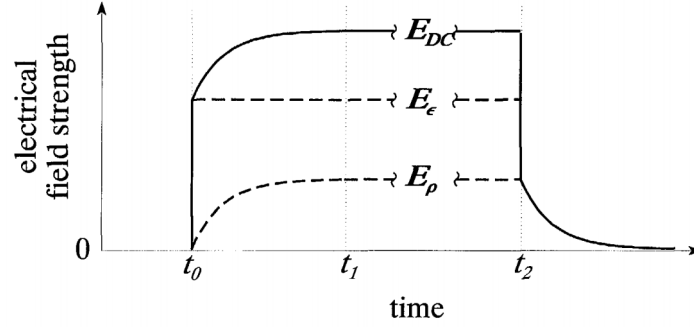


Figure 2.7: Different field situations at DC voltage [19].

Space charges

An essential parameter in the process to determine the internal electric field is space charge. Space charges accumulate at interfaces if a gradient exists in the conductivity σ or the permittivity ϵ , resulting in:

$$\nabla \frac{\epsilon}{\sigma} \neq 0 \quad (2.36)$$

The space charge accumulation takes place in the insulation [20] which is calculated from:

$$\rho = \sigma E \cdot \nabla \frac{\epsilon}{\sigma} \quad \text{for } t \rightarrow \infty \quad (2.37)$$

Depending on the characteristics of the interface two types of charges can accumulate [21] as seen in fig. 2.8.

- **Homocharge** - The polarity of the space charge is the same as that of the nearest electrode. The homo charge accumulates if the charge transport through the electrode/insulator interface exceed the transport through the bulk of the dielectric releasing the stress of the interface and increasing the stress in the insulator material.
- **Heterocharge** - The polarity of the space charge is opposite of the nearest electrode which occurs if the bulk insulator material transports charges more easily than they are extracted by the insulator/electrode interface. Heterocharges increase the electric stress at the interface while releasing the stress in the insulator material.

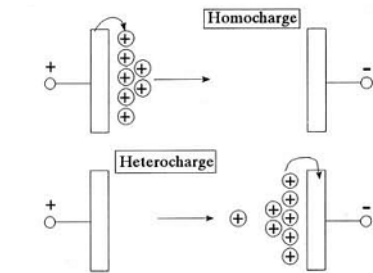


Figure 2.8: The accumulation of homocharge and heterocharge [21].

2.3.3 Corona discharges

Corona is a PD in gas caused by extremely inhomogeneous fields. The condition for exceeding the minimal breakdown strength is achieved locally at relatively low inception voltages and partially breakdown the gas long before a complete breakdown can take place.

There is no basic difference between corona at DC voltage compared to the discharges in AC. The DC electric field during PD is in the capacitive stage and not influenced by the space charges making it very similar to the AC field in the short time period to breakdown.

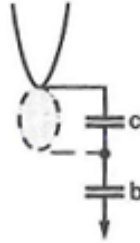


Figure 2.9: Equivalent circuit for *corona* discharges with *c* representing the gas volume to break down [11].

The discharge process of corona depends on the location of the protrusion and the polarity of the applied voltage. In this way corona is named *positive corona* if the discharge takes place due to a protrusion at positive voltage, while for *negative corona* to occur, the discharges take place near a protrusion at negative voltage. In the case of AC the corona taking place alternates the corona mechanisms depending on the voltage applied.

Negative corona mechanism

A diffuse discharge occurs around the sharp point from which the electrons are being pushed away leaving behind a positive space charge. At a certain distance away from the point, the electrons attach to gas molecules of electronegative gases such as air and SF_6 . These negative ions play a role in that they shield the sharp point from the electric field shown in figure 2.10 and as a result the discharge stops.

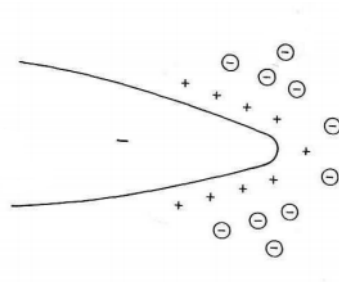


Figure 2.10: Negative corona: Negative space charges shield sharp point [11].

The space charge drifts away and the electric stress recovers so that the discharge can ignite again causing the recurrent behaviour of negative corona. The corona at the tip has a rapidly and steadily pulsating mode. This is known as *Trichel pulse corona*. Each current pulse corresponds to one main electron avalanche occurring in the ionization zone. In the case of a non-electronegative gas used in the gas gap, this recurrent behaviour will not result.

During the process of avalanche growth, some photons radiate from the core in all directions. Photoelectrons can be produced that start more avalanches that are directed away from the cathode. The motion of the electrons and negative ions away from the

cathode and at the same time the positive ions toward it correspond to the corona current pulses through the high-voltage circuit.

An increase of the applied voltage results in a higher repetition rate of the *Trichel pulses*, while the discharge magnitude stays approximately constant. A transition occurs to pulse-less discharges called "glow" when the repetition rate increases and the discharges cannot be distinguished from one another. Increasing the voltage further would cause pre-breakdown streamers to appear, which could develop into a complete breakdown or *spark*.

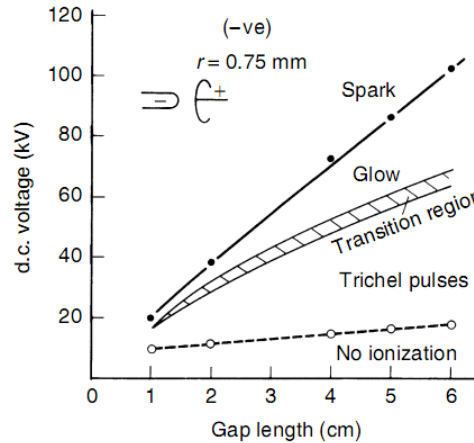


Figure 2.11: Negative rod-plane breakdown and corona characteristics in atmospheric air [14].

In fig. 2.11 the different discharge modes are shown for varying voltage and gap length.

Positive corona mechanism

The ignition value of starting positive corona called *inception voltage* is slightly higher than it is for negative corona. The reason for this is that positive corona develops at the anode with no cathode in the region with high field strength. Slightly above inception level, there exists a small volume of space at the sharp point where the field strength becomes high enough to cause ionization by collision in the gas. As a free electron is driven towards the sharp point by the electric field, it causes an electron avalanche. A cloud of positive ions is left behind very near the point and form an extension to the point at positive voltage. Under the right condition, the high field volume may suit the formation of streamers extending from the anode called: *burst-pulse streamers*. Too much of the positive space charge will begin to shield the region from the point lowering the high electric field causing the discharges to stop as shown in fig. 2.12. The ions afterwards drift away from the point and the region with high field strength is again in effect and the discharges can start again.

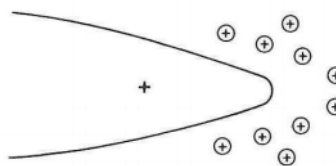


Figure 2.12: Positive corona: Positive space charges cause periodic extinction of the discharge [11].

Increasing the voltage increases the region of high electric strength around the point. As a result longer streamers emerge creating bigger discharges no longer extinguished by positive space charges. A further increase of the voltage and a cloud of negative ions may form near the anode surface such that the onset-type streamers become very frequent so that they overlap in space and in time, the discharge takes the form of a *glow* covering a significant part of the point surface. The corresponding current of this glow as it is measured in the HV circuit is a quasi steady current.

At even higher voltages the clouds of negative ions at the anode can no longer maintain their stability and become ruptured by long violent pre-breakdown streamers which are measured as high-amplitude current pulses. A further raise in voltage would eventually result in these streamers extending all the way to the cathode causing breakdown over the whole gas gap. The different discharge mechanisms as a function of voltage and gap length are displayed in figure 2.13.

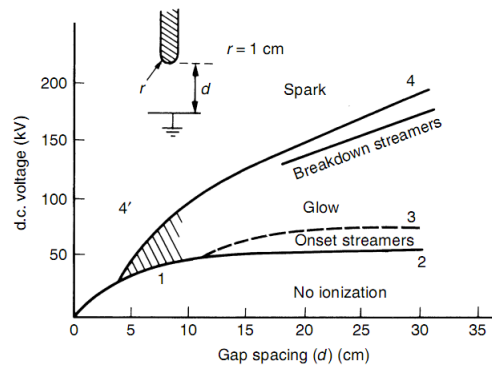


Figure 2.13: Positive hemispherical capped anode and plate cathode breakdown and corona characteristics in atmospheric air [14].

Comparison of negative and positive corona

The main parameter to describe PD activity and breakdown for a sharp point is the local field strength in which the tip is embedded. This results in inception of corona being a function of the applied voltage. The inception voltage for negative corona is lower than that of positive corona.

The breakdown of an electronegative gas is developed through a sequence of processes:

1. Generation of a starting electron
2. Streamer ignition at inception voltage
3. Pre-breakdown PD (streamers and arrested leaders)
4. Stepped leader propagation

Statistical time lag Positive corona (cathode directed) initiates in a shorter statistical time lag after inception voltage application than for negative corona (anode directed). For positive corona, the statistical delay is determined by the availability of the first electron close to the protrusion tip within the critical volume. The electron is generated by collisional detachment and is strongly dependent on the electric field.

Negative corona main mechanism of electron generation is determined by the field emission from the tip of the protrusion.

Influence of shape protrusion In negative corona the space charge present around the tip affects the local electric field. This has an effect on the discharge magnitude of the corona discharges. On the other hand it is noted that since positive corona is initiated by electron avalanches away from the tip, its influence on field distortion also influences the discharge behaviour. If the space charge in the vicinity is dominant, the tip will become shielded and the radius of the tip no longer contributes to the local field enhancing.

Discharge stages For both polarities the first high-magnitude discharge is followed by repetitive smaller pulses. In the pre-breakdown stage, large discharges re-strike in the same channel of the arrested leader. The re-striking occurs more frequently in negative corona conditions. The pre-breakdown stage of glow discharge is present for both polarities.

Shape discharges Positive streamers develop in relatively narrow channels due to the concentrating effect on the elementary avalanches directed to the streamer's head. Electron avalanches emerging from the negative streamer tend to spread radially [22]. For both polarities, the streamer radius is inversely proportional to the gas pressure.

2.3.4 Internal discharges

Internal discharges occur in the gas-filled inclusions of the solid dielectric that can range from voids, cracks and even defects of the molecular structure, because these inclusions have a lower breakdown strength than the solid. In the case of the permittivity of the inclusion also being lower than that of the solid insulation, the field intensity in the cavity is higher than in the dielectric making it the most likely region for discharge to occur under normal working stress.

The occurrence of an internal discharge takes place if the conditions of the voltage across the void exceeds the minimum breakdown voltage V_{min} such that the electric breakdown strength is exceeded so that a self-sustaining discharge can develop and a starting electron is present that is either supplied by external sources or by previous discharges to instigate an avalanche. The value of the breakdown strength is dependent on the dimensions and contents of the void, the pressure and temperature inside.

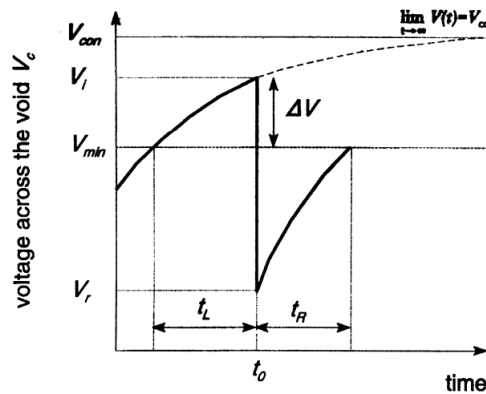


Figure 2.14: Voltage across a cavity in a solid dielectric [17].

The availability of starting electrons is based on a stochastic process and therefore a time lag t_l occurs for an avalanche to take place after the minimum breakdown voltage V_{min} has been reached. This phenomena results in fluctuations between discharge magnitudes and time in between the discharges. The time between discharge and the voltage across the void again reaching U_i is named the *recovery time* t_r as visible in fig. 2.14.

A discharge results in a conductive path between the surfaces of cavity of opposite polarity such that surface charges are deposited equalizing the voltages of these surfaces. The potential difference over the cavity decreases drastically falling back to a residual voltage V_r lowering the electric field and the discharge stops.

AC voltage

Partial discharges in solid insulators are the main cause of breakdown of the solid insulator in the case of AC voltage as they cause a slow erosion of the material [11]. Cavities in a dielectric can be represented by the equivalent circuit of a capacitive model as shown in figure 2.15 in which c represents the capacitance of the void, b the capacitance of the spacer in series with the void and a the capacitance of everything else. With an applied voltage over the dielectric sample a of V_a , the synchronous voltage across the cavity V_c is measured according to be:

$$V_c = \frac{b}{b+c} V_a \quad (2.38)$$

In the case of no time lag taken into account, a discharge takes places when V_c exceeds

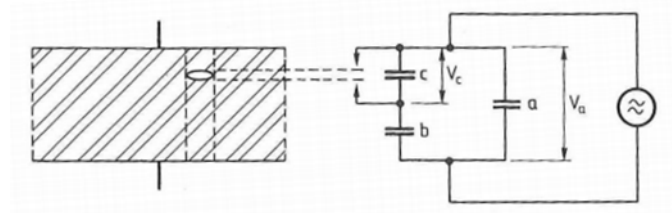


Figure 2.15: Capacitive model of internal void [11].

the inception voltage, V_c collapses to a low level residual voltage and the discharge extinguishes. The voltage across the void starts increasing again until the discharge level is reached resulting in the recurrent behaviour of partial discharges which is clearly visible in fig. 2.16.

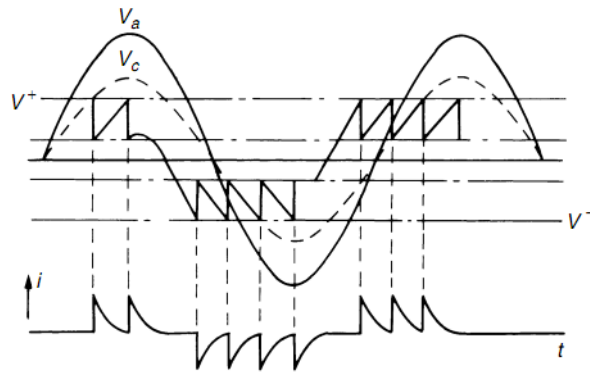


Figure 2.16: Sequence of cavity breakdown under AC voltages [14].

In the case of breakdown of the void, a current flows through the spark gap rather than through the capacitance c as can be seen in fig. 2.15. The current is composed of both $i_c(t)$ discharging capacitance c and $i_b(t)$ discharging stray capacitance b as can be seen in fig. 2.17. The current $i_b(t)$ flows through b and the test-object a . From this circuit we can distinguish between the internal charge taking place in the void and the external charge which is measurable on the electrode of the dielectric that has the void inside.

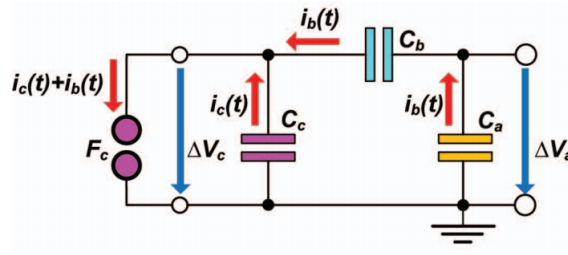


Figure 2.17: Transient currents flowing through capacitive model during discharge [23].

Internal charge q_c is equal to the time integral of the sum of the transient currents $i_b(t)$ and $i_c(t)$ causing the drop of voltage ΔV_c across the capacitance of c . For the insulation materials, the condition $C_a \gg C_c \gg C_b$ generally satisfies and the internal charge can be approximated by:

$$q_c = \Delta V_c (C_b + C_c) \quad (2.39)$$

The external charge is the charge that can be measured on the outside of the dielectric and represents the time integral of the transient current flowing through the series connection of both capacitances of b and a and according to the capacitive divider ratio comes down to:

$$q_i = \Delta V_a \cdot C_a \approx \frac{C_b}{C_a} \quad (2.40)$$

Combined with eq. (2.39) gives:

$$q_i = q_c \frac{C_b}{C_b + C_c} \approx q_c \frac{C_b}{C_c} \quad (2.41)$$

According to the condition of the capacitances in the sample $C_c \gg C_b$ it must be concluded that the charge that is detectable at the electrodes of the test object is in fact much smaller than the internal charge taking place:

$$q_i \ll q_c \quad (2.42)$$

The term apparent charge to describe the measurable external charge as is noted in the IEC60270 conventional PD detection method described fully in section 3.2.1 is proportional to, but not equal to the amount of charge that is involved at the internal discharge [23].

DC Voltage

The discharge behaviour after the DC voltage has reached its final value is no longer represented by the capacitive model of an internal cavity in fig. 2.14. The dielectric currents that flows through the system have to be taken into account which is done by extending the capacitive model for internal cavities with leakage resistances parallel to these capacitances so the model in fig. 2.18 can be used to represent the resistive and transition stages of the DC voltage across the cavity.

The classic *abc* diagram is extended with leakage resistances. A slowly growing voltage v_c over the defect occurs if these leakage resistances are linear equalling to:

$$v_c = \frac{R_c}{R_b + R_c} (1 - e^{-t/\tau}) V \quad (2.43)$$

Two processes simultaneously recharge the void once a discharge has occurred as seen in fig. 2.19. The void will be recharged by the dielectric current j_D of the sample which is represented by leakage resistance R_b . And the deposited surface charge from the discharge

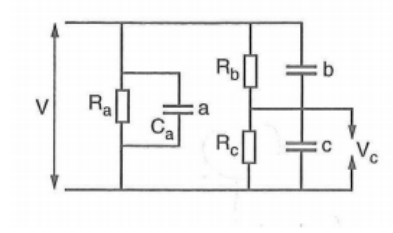


Figure 2.18: Classic *abc* diagram extended with leakage resistances [18].

redistributes itself resulting in a current j_c across the surface resistance of the void. This current is represented the leakage resistance R_c resulting in a time constant τ of the recharging process given by eq. (2.44) and visible in the voltage across the cavity in fig. 2.20.

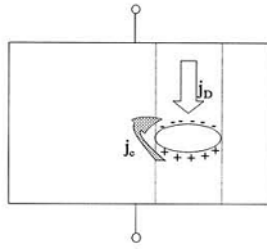


Figure 2.19: Recharging of a cavity by the dielectric current and the distribution of surface charges [21].

$$\tau = \frac{R_b R_c}{R_b + R_c} (b + c) \quad (2.44)$$

Whenever the voltage across the void reaches the minimum breakdown voltage u of the defect with no time lag t_l present, a breakdown takes place and charging of the void starts over again with a time between breakdowns t_r or the recovery time.

$$t_r = -\tau \ln\left(1 - \frac{u}{V_s}\right) \quad (2.45)$$

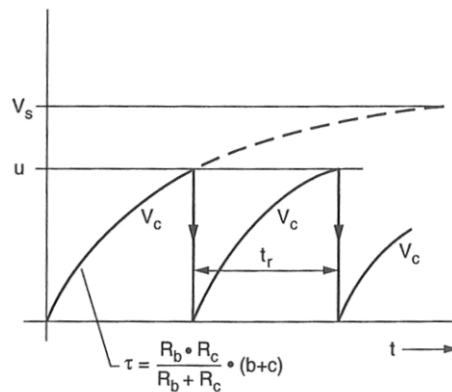


Figure 2.20: Partial discharges generated by DC voltage [18].

Comparison AC to DC

Recurrent behaviour In the case of breakdown in a cavity the voltage V_c across reaches the breakdown value and the gap breaks down. The capacitance c used in the *abc diagrams* for both AC and DC voltages discharges. Physically within the gap the breakdown result in charge transfer from one surface to the others. These charges are deposited on these surfaces counteracting the main field and the voltage difference over the gap decreases drastically.

In AC as the voltage rises further, the breakdown value is reached again and the partial discharges repeat in this way until the voltage reverses. The same process starts again in the other polarity.

In DC the applied voltage will not vary along with the main field over the gap. After charge accumulation from PD has taken place, the local field is minimal but slowly increases as the accumulated charges slowly disappear in the form of leakage currents. The potential difference increases between the two surfaces and the breakdown is reached eventually. A PD occurs and the whole process starts over again.

Initial free electron generation The free electron that initiates an avalanche inside of a cavity might come from two sources. These sources are volume ionization or field emission of charges near the void surface. For the very first discharge the electric field in the void is most likely too low for field emission, therefore the production of these starting electrons will come from cosmic or background radiation.

Other sources of free electrons come from de-trapping electrons from shallow traps on or near the surface of the cavity, electron injection from the electrodes, and space charges from previous discharges that are released due to impact ionization processes.

In AC the PD in an active cavity is dominated by the surface emission of de-trappable charges. The reversal of polarity result in these charges emitted from the cavity surface under the influence of the electric field becoming free electrons. The effect of trapped charges in DC result in a local lower electric field and reduce the probability of discharge. The generation of starting electrons will be mainly from volume ionization.

Discharge mechanism In the internal cavity exists a critical over-voltage above the inception level at which a critical space charge density is obtained within the cavity. Below this critical over-voltage the Townsend mechanism is operative while above the mechanism for streamer discharges prevails. The critical value of the over-voltage increases with decreasing gap, increasing thickness and permittivity, and increasing ignition voltage U_i of the air gap. Also the statistical time lag τ_s determines the over-voltage taking place and with that the type of discharge mechanism in the cavity.

The discharge magnitudes of the Townsend-like discharges are linearly related to the over-voltage while the magnitude of the streamer-like discharges are rather insensitive to the over-voltage. The streamers increase in magnitude with an increasing gap to bridge.

Two opposing forces also influence the characteristics of the discharge in the gap by varying the electric field in the gap. These are the:

- The ionization process in the gap enhancing the field by the positive ion space charge.
- The displacement current in the gap due to current flowing in the external circuit, reducing the electric field in the gap.

With lower over-voltages the positive ion space charge field is outweighed by the reduction of the electric field due to the displacement current. This results in a decrease of the size of consecutive avalanches.

Leakage currents Leakage currents of the charges that have been built up occur in either the dielectric through diffusion or recombination but also through conduction along the walls of the cavity. The conductivity plays an important role in the leakage currents flowing and the charge decay progress.

The effect of leakage current results in dispersion of the built up charge that in the case of AC results in less de-trappable electrons at polarity reversal and thus decreasing the repetition rate, while for DC the faster dispersion of charges result in a smaller recovery time for the voltage at which a discharge can occur. The resulting repetition rate increases with increasing current leakage.

Surface condition The condition of the surface is very important to the type of discharges that take place within the gap. In the case of an virgin cavity no cathode is available within the void. No secondary electrons can be initiated by the γ feedback mechanism to sustain a Townsend discharge in the cavity. For breakdown of such a cavity the voltage in AC and in DC must be increased for streamers to occur.

An aged cavity has had chemical changes in the surface due to deposition of PD by-products and moisture. These changes result in a lower surface resistivity forming layers that are borderline isolating and conducting. This semi-conducting layer performs as a cathode within the cavity from which secondary electrons can be freed by the γ mechanism making Townsend discharges possible.

An aged cavity has an increased conductivity and an increase of leakage currents as the surface charges along these conductive paths decay faster along the surface of the cavity [24, 25].

The inception voltage is also determined by the surface condition as the first discharge of the PD takes place without a physical cathode in the gap. A streamer discharge must take place at a higher voltage than necessary for inception of a Townsend discharge. This PD results in an deposition layer of charges on the surface functioning as a cathode such that Townsend discharges are possible. Below the inception voltage of the streamer mechanism Townsend discharges are still able to occur resulting in an extinction voltage lower than the inception voltage.

Repetition rate The PD in a dielectric under steady state DC conditions recurs as a result of the finite resistivity of the dielectric. A discharge event can succeed the previous discharge with a time interval Δt which is the sum of the recovery time t_r and the time lag t_l as can be seen in fig. 2.14. The discharge repetition rate n is calculated as the reciprocal of the time interval, resulting in

$$n = \frac{1}{\Delta t} \quad (2.46)$$

The maximum possible repetition rate is in the case of no time lag shown by fig. 2.20 resulting in

$$n = \frac{1}{t_r} \quad (2.47)$$

Using the recovery time as shown in eq. (2.45) x can be chosen to represent $x = \frac{v_s}{u}$ which also equals

$$x = \frac{\text{voltage over sample}}{\text{inception voltage of the sample}} \quad (2.48)$$

for which a large x follows

$$t_r \approx \frac{\tau}{x} \quad (2.49)$$

and the repetition rate to be written as:

$$n \approx \frac{x}{\tau} \quad (2.50)$$

The repetition rate increases linearly to the voltage over the sample [18].

Comparing the PD repetition rate of DC to AC voltages with amplitude V_r the extinction voltage, V_{min} the minimum breakdown voltage and V the voltage over the sample as they are shown in fig. 2.14 gives for AC a repetition rate of:

$$n_{AC} \approx \frac{C_b}{C_c} \frac{dV}{dt} \frac{1}{V_{min} - V_r} \quad (2.51)$$

and for DC:

$$n_{DC} \approx \frac{1}{\tau} \frac{C_b}{C_c} \frac{V}{V_{min} - V_r} \quad (2.52)$$

Equal repetition rates for both types of voltages occur when

$$\frac{dV}{dt} = \frac{V}{\tau} \quad (2.53)$$

At a 50Hz signal the repetition rates will be equal if $\tau = 3\text{ms}$. The time constant in practice is many orders of magnitude larger, thus higher repetition rates occur at AC voltages than at equal DC voltage.

2.3.5 Surface discharges

The net effect of placing a solid dielectric support into a GIS is a decrease in the breakdown strength of the overall system. The dielectric interface created by the solid support insulation representing a parallel insulation to the gas insulating medium is a very critical part of the electrical equipment used in high voltage applications.

Discharges take place along this interface when the tangential field strength exceeds the breakdown strength of one of the materials. Compared to internal discharges there is no spacial limitation making it possible for discharges to bridge long distances.

At low gas pressures it is more likely to see discharges start in the gas medium, but as the dielectric strength of the gas increases with increasing gas pressure, the likeliness of a discharge across the surface of the insulator becomes very high. These combined discharges are known as surface discharges.

The spacer placement in a GIS has an effect on the *pre-breakdown conditions* resulting in a decrease of the breakdown voltage U_{bd} and PDs measured at lower voltages, but also an effect on the *flash-over dynamics* for the PD and successive PDs as the discharges have already started. Pre-breakdown conditions change with the effect of the spacer on the electric field. An intense electric field may occur along the interface. This can be due to the spacer's profile, defects attached to it or surface charges deposited on it [26]. Flash-over dynamics of PD are influenced in the form of pre-energy on a surface. The surface may increase the electron gain coefficient $\bar{\alpha}$. As soon as a discharge is ignited, the channel grows more easily due to photo-ionization and or thermal ionization in the vicinity of the surface [27].

The repetitive nature of surface discharges is explained by charge deposition taking place on the surface along the discharge path. The charges result in a local decreased field at the discharge location. The condition for PD ceases to exist and the PD extinguishes. The condition for PD is once more reinstated when the deposited charges decay.

The insulation condition of the surface of the spacer can deteriorate as a result of multiple defects. The deteriorated insulation decreases the onset voltage of discharges and must be prevented as much as possible. In all cases the dielectric strength is influenced by field distortions which can be grouped according to [28, 29]:

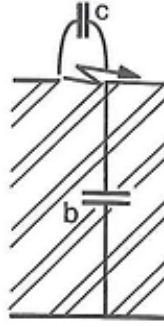


Figure 2.21: Equivalent circuit for *surface* discharges with **c** representing the part of the surface that flashes over [11].

- **Triple junction** indicates the conductor-spacer-gas junction where any poor contact, i.e. a gas layer between the spacer and the conductor result in a field intensification due to the difference in permittivity. Such a defect on the cathodes has more influence on the flash-over voltage due to the supply of initial electrons for an avalanche [30].
- **Conductive particles** attached to the surface of the spacer result in more deterioration. Defects on the spacer make the surface irregular and the conductive particle is a triple point defect that also decreases the distance over the spacer surface for PD.
- **Irregular dielectric surface** The distortions of the field by defects become stronger with increasing dielectric strength, therefore the effect is greater at a higher designed stress. With spacers present, the intensifications of the triple junctions at the surface irregularity also depend on the permittivity ϵ of the spacer material, these become stronger with increasing ϵ .
- **Static charges** on the spacer surface change the voltage profile over the surface. Intense electric field may occur midway at the interface as a result. The same effect will also occur with conductive parts attached to the spacer surface. These local accumulations of charge can supply energy to PD on their path resulting in longer discharge paths as was emphasized in [31], but can also result in micro discharges at the electrode surface.

Comparison AC to DC voltage

Triple point The triple point refers to the point of contact between the spacer, the electrode and the gas. The geometry of this intersection severely affect the breakdown characteristics [32]. An increase of electrical stress can easily result because of poor contact creating gaps between the electrode and spacer.

The electrical stress caused in the triple point is expected to be of more importance for starting a flash-over under time-varying fields (AC) as the triple point stress is then enhanced by the capacitive voltage division. For DC fields, the flash-over voltage was observed to be higher with the triple point at the cathode than it was at the anode. This is expected to be the result of electron deposition on the spacer reducing the stress on the cathode supporting higher fields.

Electrostatic shielding at this triple point is essential in the design to locally increase the breakdown strength. Figure 2.22 shows such a shielding example to reduce the field strength at the intersection of spacer to electrode.

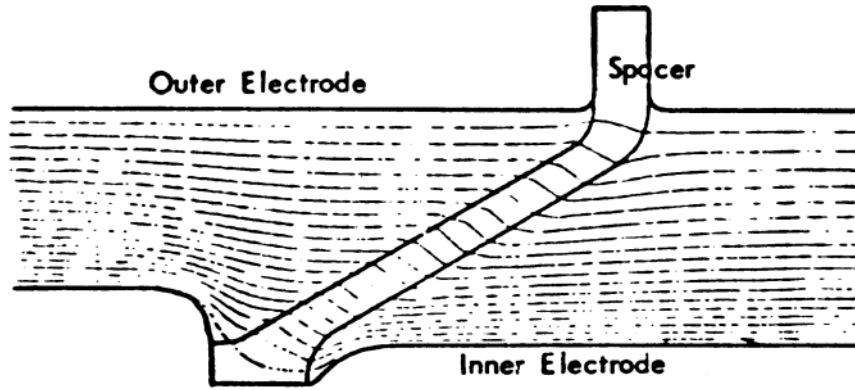


Figure 2.22: Spacer and potential distribution [29].

Voltage waveform and polarity The performance of the spacer is heavily influenced by the type of voltage across as the electric field distribution is determined by the resistivity of the spacer and the gas for DC voltages, while for AC and impulse voltages the field is predominantly capacitive and a capacitive division becomes important.

Charge accumulation The accumulation of space charge on the spacer is a phenomenon extensively studied to show that the breakdown strength is affected both in AC and DC, but especially at polarity reversal.

Charges on the dielectric surface can significantly affect the propagation of a surface discharge. Charge accumulation on an insulator surface modifies the electric field distribution in the gap. As a result the initiation and propagation of discharges in the vicinity will be influenced. Accumulation of charge on the gas-dielectric interface could occur through the following mechanisms:

- Volume or bulk charging.
- Surface charging
- Field emission

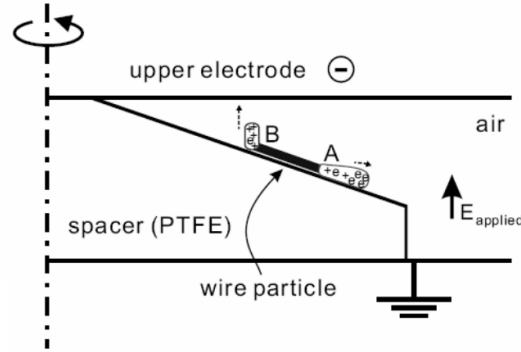
The characterizing parameter of *volume and surface charging* is the *charging time constant*, $\tau = \epsilon\rho$. The dielectric constant ϵ does not vary greatly between solid and gas insulators, making the resistivity ρ the main influencing component in the charging mechanism [33]. The *volume and surface resistance* on the other hand are both dependent on the electric field and temperature, but independent of the voltage polarity. The charging time constant is very long for DC voltage (around 15 hours) and the decay time is even longer [34].

Charge accumulation enhances by protrusions on the metallic parts of the system through *field emission*. The emitted charge migrates along the field lines depositing on the spacer surface. Differences compared to volume and surface charging are: The charging time is much shorter and the voltage polarity start influencing the charge distribution. As was noted in [33] the charge accumulation become much more visible at negative polarity.

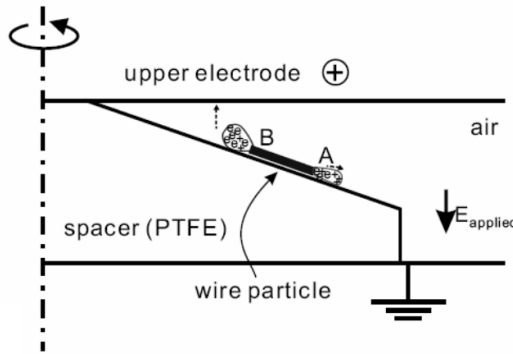
Particle contamination During operation of a GIS the spacer can be contaminated by free conductive and non-conductive particles, water vapor and decomposed SF_6 by-products [32]. Particle contamination of the surface of the spacer effect the breakdown strength negatively, but is also different for the type of spacer geometry that has been

used. In many cases it is noted that when conducting particles are present, these become the dominant mechanisms of charge accumulation on the spacer.

In the case of an conductive particle inside a GIS, the Coulomb force exerted on the particle could lift it towards sensitive areas like the high field electrode or spacer that could lead to a reduction of the insulation strength [32]. Due to PD activity of the sharp particle edges, there is also the possibility of charge accumulation.



(a) Negative voltage application.



(b) Positive voltage application.

Figure 2.23: Charge phenomenon with metallic particle on spacer [35].

A conducting particle on the spacer will result in charge accumulation on the spacer surface that reduces the breakdown strength. The behaviour of the PD varies with the polarity of the voltage applied resulting in:

- *Negative voltage* applied at the conductor results in the electric field at the tips of the particles increased. Negative discharges appears at the lower tip causing a negative flow of charge that start to accumulate on the spacer surface as is shown in fig. 2.23a. The particle is positively charged and positive discharges start to ignite from tip B. Rather than depositing upon the surface, these charges will drift up towards the electrode resulting in a predominantly negatively charged spacer due to PDs.
- *Positive voltage* applied will also result in negative discharges appearing at point B before positive discharge start to occur at point A as is seen in fig. 2.23b. The discharges at point B will be spread out more radially than before so more charge accumulation will take place at the surface. The positive discharge at A will also be accumulated at the surface making quite a different field distribution possible as was the case with the negative voltage .

2.3.6 Floating Components

Floating components within a high voltage system occur whenever a conductive component is tied to no well defined electrical potential also known as *floating*. In some cases the difference in potential between the conductor and the floating component can exceed the breakdown value of the gas resulting in a discharge over the gas gap insulating the two. The discharge results in a conductive path between the conductor and the floating component generating surface charges near the discharge location equalizing the voltages such that the potential difference disappears and the condition for discharge ceases to exist.

Introducing a conductive component in an electric field will result in the polarization of the component as seen in fig. 2.24a. Charges are induced on the surface of the components and as a result the voltage of the component is determined by capacitive voltage division as fig. 2.24b shows. Unlike the model used for internal discharges where the defect itself breaks down and is represented by capacitance c in the *abc* model in fig. 2.15 for floating components the regions between the defect and the conductors become the critical parts of the system. The accumulated charge at the surface affect not only the voltage, but based on the shape of the conductive component also the local electric field that can exceed the breakdown strength of the gas gap.

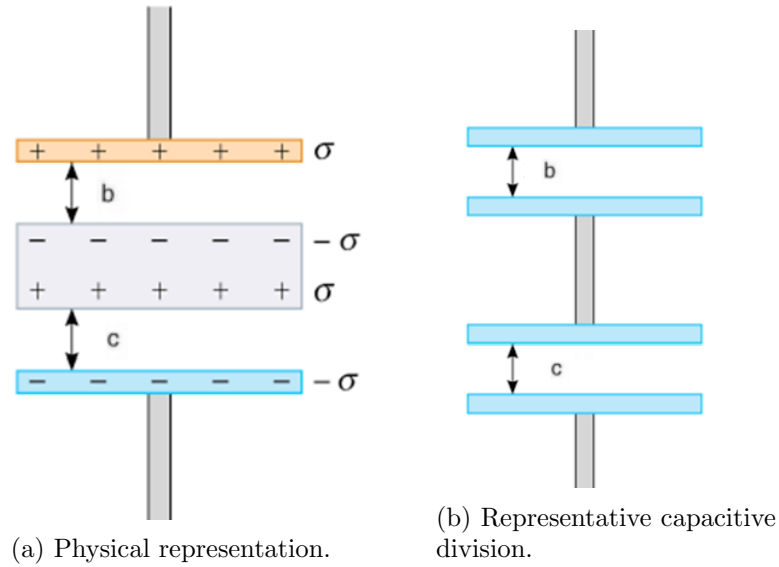


Figure 2.24: Conductive component inside a GIS.

The presence of a floating component results in a distortion of an electric field. As the floating component has a single voltage potential, the thickness of the components results in a bigger distortion due to the capacitive division.

A difference in the dielectric constant for the insulation between the floating component and the conductors has an increased difference in the capacitance and the voltage across the critical gap. An example of which is visible in fig. 2.25 where an epoxy spacer with metallic insert supporting a conductor has an ineffective contact to the electrode.

Comparison AC to DC voltage

Recurrent behaviour In AC the potential difference in the gas gap increases or decreases with the applied voltage to the electrode while the voltage of the floating component is set to a certain level within that time. Upon reaching the inception voltage the gas gap breaks down and the floating component is equalized to the voltage of the electrode by charge accumulating on the surface conducted through the discharge. With varying

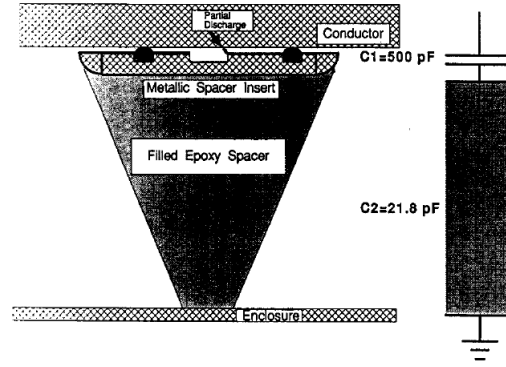


Figure 2.25: Epoxy spacer supporting the conductor with an ineffective connection between conductor and spacer insert [36].

voltage the PDs repeat in the same manner until polarity reversal takes place and the same process ignites with different polarity. The accumulated charges barely decay in the time between the discharges.

The constant voltage of applied DC should result in a potential difference over the gas gap that exceeds the ignition voltage before a PD can take place. A charge transfer takes place that deposits charges on the surface of the floating component negating the main electric field. The field strength between the component and the electrode drops drastically and the discharge extinguishes. As the accumulated surface charges slowly decay in the form of leakage current, the field increases until exceeding the breakdown strength of the gas gap and discharges again. Taking this into consideration the capacitive model of fig. 2.25 can be extended with leakage resistances to take the leakage current into account.

Initial free electron generation The starting electron necessary for initiating discharges are more abundant than is the case for internal discharges. The starting electron comes either from within the gas volume or the electrodes through field emission or radiation. The time lag τ_s is much smaller and a sequence of breakdown should be quite similar to fig. 2.16 for AC, while for DC like in fig. 2.20. The very small time lag results in a negligible over-voltage and the charge magnitude of sequential PD should be very close together.

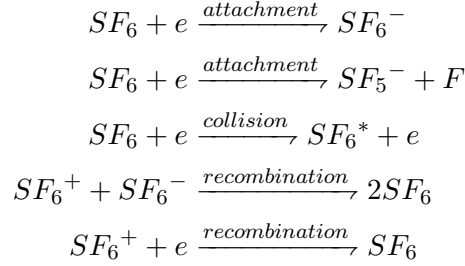
2.4 Insulating Gases

Insulating gases are dielectric materials in gaseous state that have a major role to play in the insulation of the GIS. The main purpose of such a gas is to prevent or rapidly quench electric discharges. This is done with gases that have affinity for electrons (electronegativity). Electronegative gases in essence capture free electrons turning them into negative ions through a multiple of ways [14]. The electron attachment is a competing phenomenon with ionization and if large enough can prevent the condition for breakdown to be reached inside the gas.

Of the electronegative gases, SF_6 , even though it is a green house gas, is the most widely used due to the following properties: it is incombustible, it is not poisonous, it has no colour and odour and it is not aggressive towards the electrical components. However high temperatures caused by electrical discharges do cause the creation of aggressive and poisonous by-products [32, 37]. Besides the attachment of electrons to ions, SF_6 has the advantage over air that the heavier weight and larger diameter of the molecules reduces the *mean free path* λ of the electrons in a field and resists them from getting enough energy

to ionize other molecules by collision. The mobility of the ions is lower and the possibility of recombination of them is increased while at the same time decreasing the formation of charged particles in space.

The processes unfavourable to the growth of a discharge channel in the insulating gas of SF_6 can be described as:



SF_6 can withstand higher electrical stress as a result and in homogeneous electric fields, the electrical strength of SF_6 can be around 3.0 times that of air at the same pressure [38].

For comparison of the insulating gases the ionization coefficient from the Townsend formula can be calculated per gas in the form of:

$$\frac{\alpha}{p} = Ae^{-\frac{B}{E/p}} \quad (2.54)$$

With constant A the saturation coefficient and B the inelastic collision barrier as collected from several experimental results for different gases by Heylen [39] as shown in table 2.1.

Gas	A [$cm^{-1}Torr^{-1}$]	B [$V/cmTorr$]	E/p [$V/cmTorr$]	Author
CO_2 (20°C)	4.6	182	32 - 120	Teich and Sangi
SF_6 (20°C)	13.63 50	298 940	90 - 400 400 - 1500	Bhalla and Craggs Teich and Sangi
Air (20°C)	3.5 8.1	200 249	25 - 60 37 - 143	Prasad Masch

Table 2.1: Townsend primary ionization constants [39]

Chapter 3

Measurement Setup and Detection Systems

3.1 Measurement Setup

3.1.1 Test Object

The test object to be investigated in the experiments consists of defects placed inside a section of a 380 kV single phase GIS. This was done to simulate the conditions of PD inside of an operating GIS.

The GIS construction is as follows: an aluminium conductor with a length of 510 mm and a radius of 35 mm is enclosed by a metallic enclosure with an inner radius of 150 mm. The enclosure is directly connected to the ground and on the inside coated with a thin non-conductive layer. The conductor is connected to the HV source through a bushing filled with nitrogen at 4 bar.

The inside of the GIS presents a coaxial system resulting in field distribution described by:

$$E(r) = \frac{U}{r \ln \frac{r_{out}}{r_{in}}} \quad (3.1)$$

with r_{out} the radius of the enclosure, r_{in} the radius of the inner conductor and $E(r)$ with $r_{out} > r > r_{in}$ the electric field that varies with radius. The equation shows that the field strength near the HV electrode can be significantly higher than near the enclosure as a result of the coaxial system.

3.1.2 High Voltage Circuit

In this research a comparison is made between the PDs of different defects while enduring AC and DC stresses. To accomplish this a HVAC and a HVDC source are used.

HVAC circuit

The HVAC circuit as is shown in figure 3.1 consists of a HV source in the form of a 200 kVA *single phase oil-insulated transformer*. The primary voltage is manually controlled through a regulating transformer connected to the grid based on a HV reading measured by a voltage divider on the connected in parallel to the test object C_a and the coupling capacitor C_k .

The oil transformer is operated in resonance. This is done by tuning a *resonance coil* at the primary side of the HV transformer to achieve resonance condition with the capacitances at the HV side of the circuit.

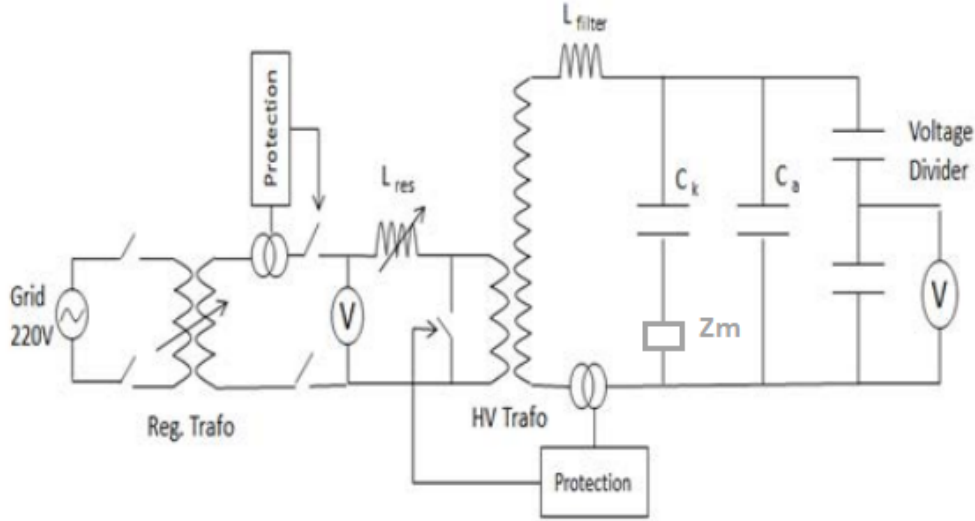


Figure 3.1: HVAC electric scheme.

To protect the voltage source in the case of a breakdown of the test object, two protection devices have been installed into the circuit. The first device trips when current peaks are detected at the HV side. The primary winding of the LV side of the transformer is short-circuited de-energizing the HV side. The short-circuit current flowing in the primary circuit is limited by the tunable inductance. In this way the test object will never suffer high stresses for too long a period of time and at the same time the transformers are protected as well.

HVDC circuit

The HVDC used for the measurements in the HV laboratory was supplied by a Heinzinger PNC 1000000 high-precision power supply.

It operates by rectifying the AC grid voltage that afterwards is converted to a 30 kHz AC voltage that feeds the transformer to generate a HV. On the HV side the voltage is multiplied and rectified by a multi-stage cascade converter. The ripple on the resulting voltage is reduced by a HV-filter. On the output side both the current and voltage are measured continuously to compare to the input settings of the user. A feedback loop to the Pulse Width Modulation (PWM) control keeps the voltage and current the same as in the settings. The supply can produce a voltage up to 100kV in both polarities simply by inverting the rectifier box.

The output of the HVDC power supply is connected to another capacitance C_{filter} of 25.5nF to suppress the HF noise produced by the DC source. Between the filter capacitance C_{filter} and the coupling capacitance C_k , a water resistor of 2 M Ω is fitted to reduce the current that could flow in the eventuality of a breakdown as visible in figure 3.3. At the end of the circuit the test object C_a is connected via the bushing.

3.2 Partial Discharge Detection

The PD inside a GIS result in a fast rising charge displacement that can be measured electrically by two methods. These are the measurements according to the:

- Conventional method - IEC 60270

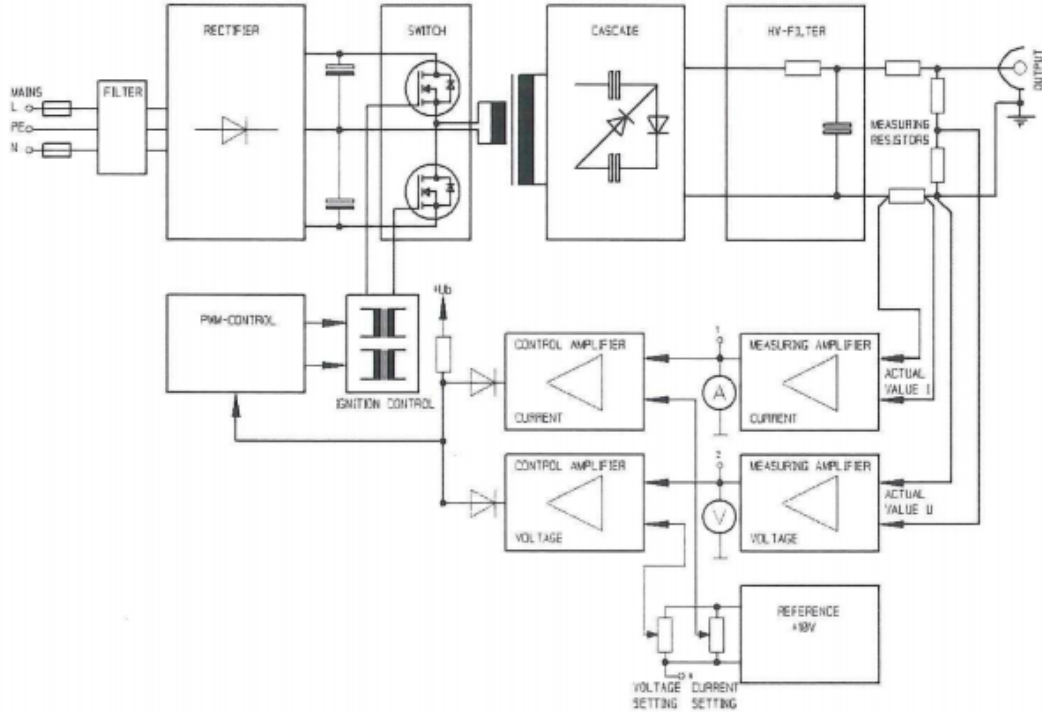


Figure 3.2: Simplified diagram Heinzinger PNC 1000000 DC source [40].

- Non-conventional method - VHF/UHF

The conventional method is based on the measurement of the current pulse that flows through the circuit. The non-conventional method which is based on the measurement of the EM waves that are excited by the very rapid PD. These signals propagate inside the GIS structure from the PD location towards a transducer with frequencies that can range up to more than 3 GHz.

3.2.1 IEC 60270 - Conventional Detection Method

The conventional method of detection of PD according to the IEC 60270 standard [41] is based on the measurement of the apparent charge. The apparent charge measured has a smaller magnitude and does not have a strict linear relationship to that of the real discharge as is shown for the calculation of charge in section 2.3.4, but a direct measurement is not physically possible. The apparent charge is still of great use for condition assessment of the test object by detecting the occurrence of a discharge taking place and differences in magnitude of the measured apparent charge also correspond to differences in magnitude of the PD in the test object.

Coupling mode

The main components of PD measurement circuit according to the conventional method are the *test object* C_a , the *coupling capacitor* C_k , the *coupling device* CD for connecting to the measurement instrument, and a *noise filter* Z . According to the IEC standard, there are two basic coupling modes depending on the connection of the CD in the circuit.

The CD in series with the test object as is shown in fig. 3.4 has the advantage of the stray capacitances of the HV side increasing the overall value of C_k . Higher sensitivity in

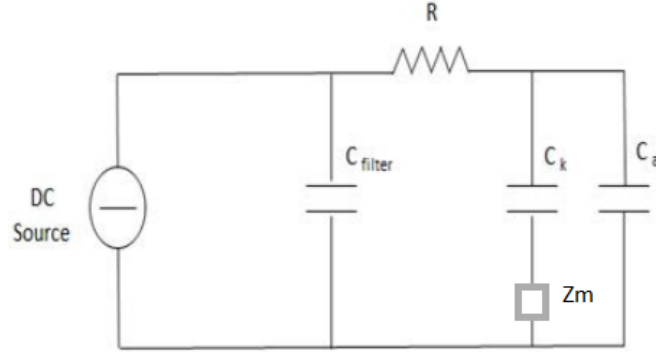
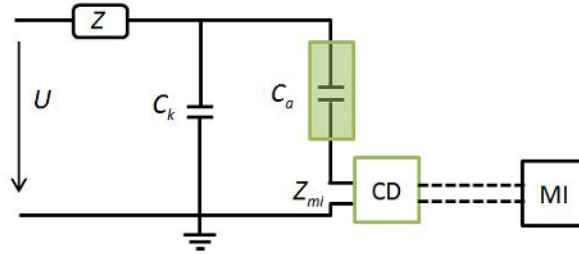
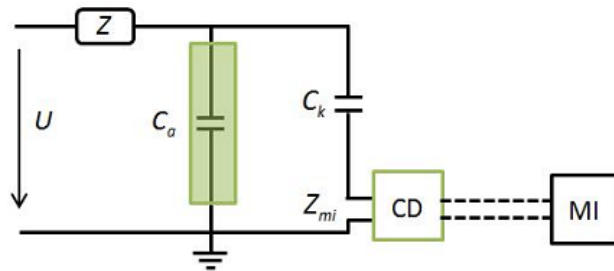


Figure 3.3: HVDC electric scheme.

the measurement [14] is achieved. In the case of breakdown of the test object however, a high current will flow through Z_{mi} that could result in damage of CD.


 Figure 3.4: Basic coupling device in series with test object C_a [14].

The arrangement of CD in parallel with C_a as shown in figure 3.5 is more commonly used and has also been used in the HV laboratory as breakdown of the test object was a real possibility. In many cases changing the ground connection is also not a possibility for the test object making the parallel connection more practical.


 Figure 3.5: Basic coupling mode in parallel with test object C_a [14].

The function of the coupling capacitor C_k connected in parallel to C_a is to create a discharge loop in which the high transient current of the PD flows. An additional noise filter Z suppresses noise generated at the HV side.

The choice of coupling capacitor C_k has to fulfil a few requirements for accurate PD measurements [42]:

1. **PD free** up to the highest test voltage level.

2. **Low inductance** in order to transmit the high frequency PD signals without excitation of disturbing oscillations that effect the current waveform.
3. **Sufficiently high capacitance** C_k to minimize the effect of stray capacitances of the measuring circuit on the reduction of PD magnitude transferred to the coupling device.
4. **Good sensitivity** achieved by the relation $\frac{C_k}{C_a} > 0.1$.

The value for the coupling capacitor used in the laboratory was 1 nC.

Coupling Device (CD)

The coupling device transfers the electric current to a usable voltage signal for the measurement instrument to detect. The CD is a very important part of the measuring circuit as it influences the PD pulse shape. The coupling devices used in the HV laboratory in combination with the conventional detection circuit are:

- Quadrupole
- High Frequency Current Transformer (HFCT)

The Haefely quadrupole serves to separate the high frequency current of the partial discharge signals from the power frequency current of the capacitor, but can also suppress the high frequency noise picked up by the measuring circuit. With an internal circuit as is shown in fig. 3.6 a resonant parallel circuit is created with a transfer impedance specifically high for the frequencies of interest acting as a bandpass filter to the incoming signals.

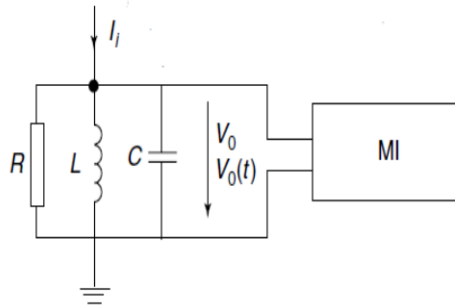


Figure 3.6: Resonant parallel circuit connected to measuring device.

Another method of measuring the high frequency PD currents is with a HFCT sensor clamped around the ground wire in the loop formed by C_k with the test object. Inductive sensors are galvanic isolated from the circuit and have a large bandwidth compared to the quadrupole operating over a bandwidth of 30 kHz - 30 MHz (IEC 60270 compliant) and 1 MHz - 60 MHz (WB detection). In the same way as the quadrupole, the power frequency current is also suppressed.

Charge evaluation

The sensors convert the high frequency PD current to a measurable voltage for the measuring instrument. This voltage waveform is dependent on the transfer function of the sensor used. It is possible to do a charge evaluation of the PD signal within a specified bandwidth. The method according to the IEC 60270 standard is to evaluate within a narrow band or a wide band by passing the measured signal through an IEC filter. The resulting peak

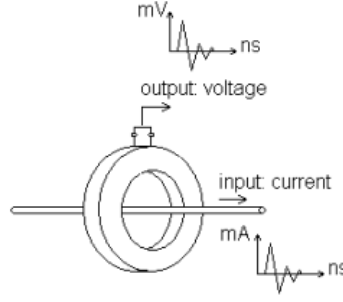


Figure 3.7: Schematic of a HFCT measuring an impulse current [43].

value is proportional to the apparent charge of the discharge. The bandwidth specified for these filters are:

Wideband:

$$30kHz \leq f_1 \leq 100kHz \quad (3.2a)$$

$$f_2 < 500kHz \quad (3.2b)$$

$$100kHz \leq \Delta f \leq 400kHz \quad (3.2c)$$

Narrowband:

$$9kHz \leq \Delta f \leq 30kHz \quad (3.3a)$$

$$50kHz \leq f_m \leq 1MHz \quad (3.3b)$$

For the wide band method the outer limits of the bandpass filter are f_1 and f_2 with a frequency range Δf specified. The second type of IEC filter is a narrow bandpass filter that uses a very narrow bandwidth compared to the wide band method of Δf with a mid-frequency of f_m . Between the two filters there is a difference in the pulse resolution time, the shortest time possible between consecutive pulses. The pulse resolution time is inversely proportional to Δf [41] with times for the wide-band method of less than 10 μs and for the narrow band exceeding 80 μs . The method used in the laboratory for measurements on the GIS is the wide-band method.

Calibration

The measurement of the apparent charge q_a is carried out through the reading of the transient voltage appearing across the test object terminals. With the techniques previously explained a reading R_i proportional to q_a is retrieved by the measuring instrument. The calibration procedure allows to express R_i in terms of pC. A known charge q_0 is injected in the test object terminals causing a reading of R_0 in the detector. The scale factor is determined by:

$$S_f = \frac{q_0}{R_0} \quad (3.4)$$

A reading for the apparent charge as a function of R_i can be calculated by:

$$q_a = S_f R_i = q_0 \frac{R_i}{R_0} \quad (3.5)$$

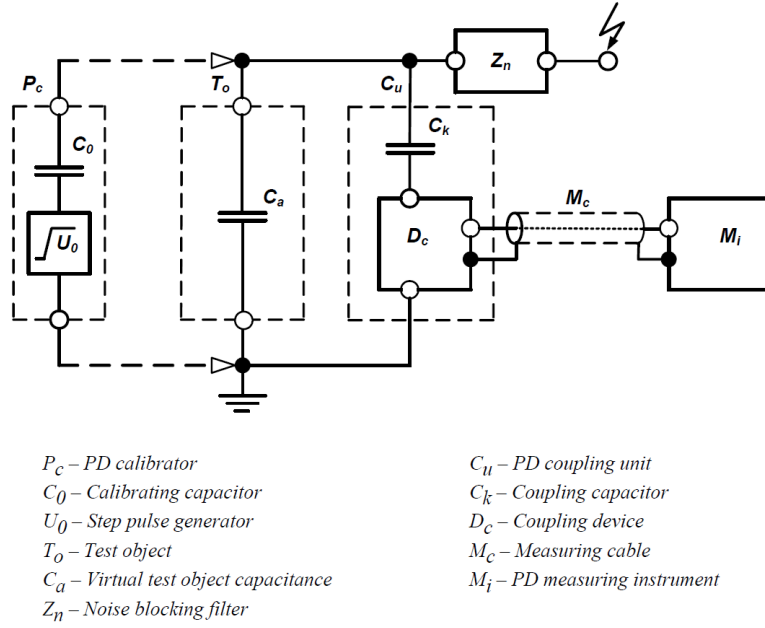


Figure 3.8: Major components of common PD measuring circuits [42].

3.2.2 Ultra High Frequency (UHF) - Non-conventional Detection Method

Electromagnetic radiation

The PD is basically an acceleration and deceleration of charged particles by the electric field. This movement causes time-varying electric and magnetic fields travelling outwards from the position of these charges known as electromagnetic radiation.

To demonstrate the excitation of EM radiation, Gauss's law and Ampere's law are used. The magnitude of the electric field is calculated by the Gauss's law for electricity as shown in eq. (3.6) which states that the charge enclosed by a Gaussian surface is proportional to the closed surface integral of the volume enclosing field lines of the charges as the electric field point radially outwards from the charge.

$$\nabla \cdot \vec{E} = \frac{\rho}{\epsilon_0} \quad (3.6)$$

The magnetic field component of the electromagnetic radiation is generated due to Ampere's law seen in eq. (3.7). The movement of the charge result in a magnetic field. The fields of a moving particle are visualized in fig. 3.9.

$$\nabla \times \vec{B} = \mu \vec{J} \quad (3.7)$$

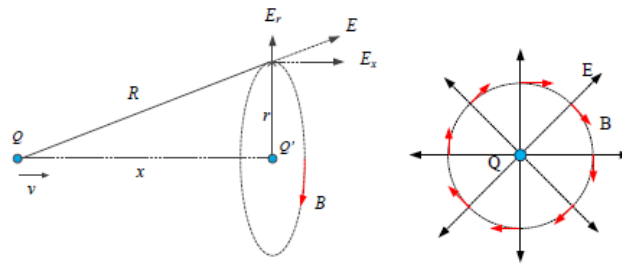


Figure 3.9: Electric and magnetic field of a moving charge particle Q [44].

The EM radiation is picked up by a sensor a distance away from the source. Figure 3.10 shows the case of a single charge as the source of the radial continuous field lines at rest at point A. Upon accelerating to point B, the electric field lines will update within a discrete time. The information related to the new position propagates as a wave pulse that gradually updates the field lines. The distortion of the field lines due to transmission of information is called a *kink*. The energy from the force that accelerates the charge is partly expended to propagate the kink in the field.

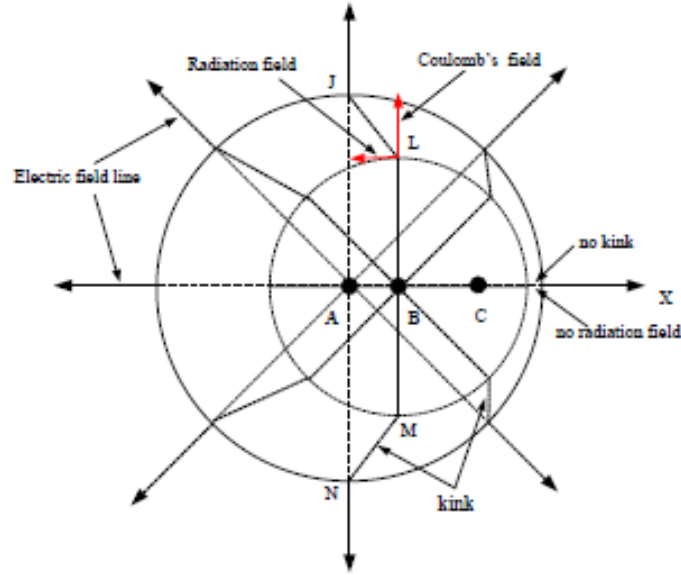


Figure 3.10: Electric field line distortion (kink) due to charged particle acceleration [45].

In the kink region the electric field is composed of two components with E_t the transverse component of the electric field and E_r the radial Coulomb field. According to the Poynting vector $\vec{S} = \vec{E} \times \vec{H}$ representing the direction of propagation and power of an EM wave that has a radial direction transferring energy away from the charge only the transverse component of the electric field is responsible for radiation as visible in fig. 3.11. The relation between the two components of the electric field in the kink region as seen in fig. 3.11 is shown in eq. (3.8).

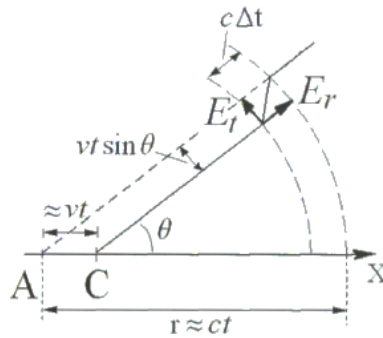


Figure 3.11: The components of the electric field at an arbitrary angle θ caused by an accelerated charge towards point A continuing to point C with constant velocity [46].

$$\frac{E_t}{E_r} = \frac{vt \sin \theta}{c \Delta t} = \frac{at \sin \theta}{c} = \frac{ar \sin \theta}{c^2} \quad (3.8)$$

With $E_r = \frac{q}{4\pi\epsilon_0}$ and N the number of charges it is possible to describe the tangential field as:

$$E_t = \frac{Nq}{4\pi\epsilon_0} \frac{a \sin \theta}{c^2 r} \quad (3.9)$$

From eq. (3.9) it can be concluded that the emitted radiation from a PD is proportional to:

- The changes of the PD current pulse: faster acceleration a of the electrons (i.e. steeper current pulse), or the larger number of charges N in the discharge (i.e. the larger pulse amplitude) result in a higher amplitude of the radiated field.
- The inverse of the distance r to the transducer.
- The angle of observation θ : The radiated electric field is maximum along the line perpendicular to the accelerated charge of the PD.

The transient EM signals emitted by a PD propagate in the GIS which acts as a low loss transmission wave-guide between the inner and outer conductor. Depending on the geometry different boundary conditions are imposed upon the waves that interfere the electromagnetic fields resulting in different modes of propagation that still fulfil the Maxwell's boundary conditions. These are:

- The transverse electromagnetic modes (TEM), that have no electric and magnetic field in the direction of propagation.
- The transverse electric modes (TE) with no electric field in the direction of propagation.
- The transverse magnetic modes (TM), which have no magnetic field in the direction of propagation.

The TE and TM are referred to as the higher order propagation modes and only propagate in the wave-guide when the frequencies of the waves exceed a certain cut-off frequency f_c . Below this level these propagation modes are rapidly attenuated.

UHF detection system

The main concept of the RF PD measuring technique is that PD pulses, due to their short duration and rise times in the nanosecond regime, generate electromagnetic radiation at various frequencies within the range of the RF spectrum. The generated EM radiation then propagates from the defect along the wave-guide and is picked up by the proper RF coupling electrodes.

The three modes of electromagnetic coupling used in detection of PD signals are:

1. Capacitive coupling: The voltage across the capacitance between the detecting circuit and the PD source can be measured with high impedance equipment.
2. Inductive coupling: The mutual inductance between the source and the detection circuit result in the current induced in the detection circuit by the magnetic field.
3. Radiated coupling: The type of coupling in which an electric current is induced in the detection circuit by electromagnetic radiation produced by the EM source.

The receiver sensor functions by extracting power from the field in the vicinity and delivering it to a load or terminating impedance. The electrical characteristics of the sensor are constant within a certain frequency range depending on the design. The bandwidth of the sensor is described by its *transfer impedance* that results in a frequency response for every PD signal to be measured by the detection unit.

The sensors used in the GIS for detecting RF signals are divided into internal and external sensors. The internal sensors are mounted in slots in low field regions at power frequency. The internal sensor is specifically designed to not enhance the electric field in the region resulting in designs of aluminium disc antennas. The external sensors are mounted in the dielectric windows of the GIS that create openings in the metal enclosure that permit the propagation of the EM wave outside the coaxial wave-guide structure of the GIS.

The internal sensors have higher sensitivity and are less subjected to external noise compared to the external sensors. The measurements of RF signals that have been done in the HV laboratory of the TU Delft have only been carried out with an internal antenna as the sensitivity of that type is maximal.

3.2.3 The PD current pulse

During a PD, Electrons initially at rest are accelerated and decelerated rapidly by the electric field resulting in a short current pulse [47, 17]. The high mobility of the electrons lead to very fast rise times into the nanosecond range, while the ionic components show rise times of some hundred of nanoseconds [47]. The spectral energy of pulses of short duration reach up to the UHF frequencies of the spectrum. The shorter the PD current pulses the more spectral energy appears at higher frequencies [48].

To show the effect of the pulse duration on the frequency dependent emitted electromagnetic energy a Gauss type model for the PD current pulse can be used defined according to the mathematical expression eq. (3.10) [43].

$$i(t) = a \cdot t^n \cdot e^{b \cdot t^m} \quad (3.10)$$

Parameters a , b , n and m define the pulse shape characteristics from the rise time to the decay time.

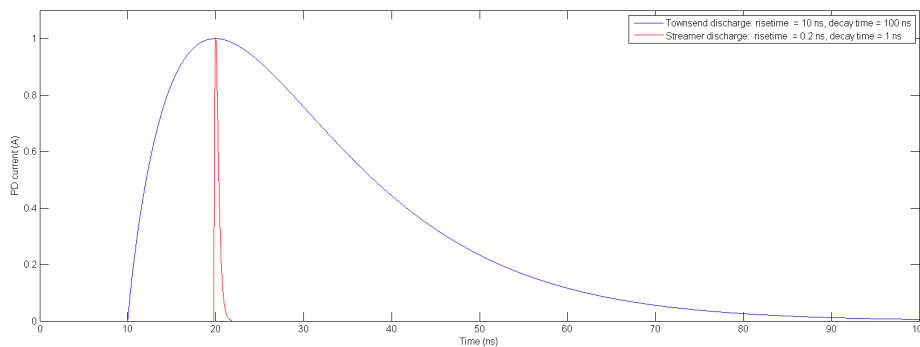


Figure 3.12: Representations of PD current pulses as a result of the Townsend and Streamer mechanism.

The physical conditions at the defect resulting in the PD are responsible for the duration and the characteristics of the PD current pulses. The physical parameters that define these conditions can range from the electric field, temperature, physical properties of the surface in vicinity of the defect etc. The PD mechanism also has an effect on the shape of the PD current pulse. The characteristics of these pulses are:

- Townsend-like discharges: The formation of the discharges is a slow process with rise times as long as several tens of nanoseconds and the duration can last several hundreds of nanoseconds [17].
- Streamer-like discharges: Discharges with a steep front (decades of picoseconds) and a short duration (approximately a nanosecond).

Based on the above information a representative PD current pulse can be built as shown in fig. 3.12. The normalized frequency spectrum of these pulses displayed in fig. 3.13 show that the maximum frequencies differ greatly from one another and that the frequencies of the Townsend PD will not be detected in the Very High Frequency (VHF)/UHF range as the frequency range is starting at 30 MHz.

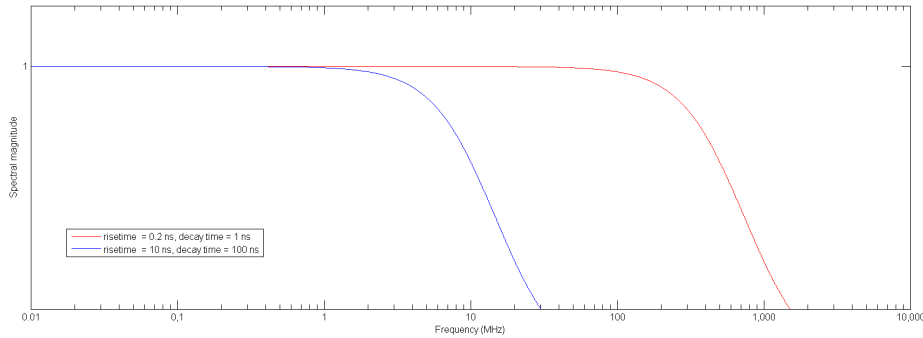


Figure 3.13: Normalized spectra of Gaussian PD current pulses.

In the VHF/UHF range it is expected that the following discharges can be detected [46]:

- high electrical stresses (surface and positive corona discharge).
- discharges in gases at high pressure (e.g. gas bubbles in oil).
- in virgin cavities.

3.3 Detection Units

3.3.1 Techimp PDBaseII

The Techimp PDBaseII is a digital detection unit with 4 PD input channels with a sampling rate of 200 MS/s and a dynamic range of 75 dB.

Galvanic separation between the acquisition unit and the user is accomplished via a fibre optic decoupling system.

For every channel the PDBaseII is able to display the signals in three different bandwidth modes. These are:

- IEC 60270, 30 kHz - 400 kHz;
- WB (Wide band), 16 kHz - 48 MHz;
- WB + HPF (High Pass Filter), 2.5 MHz - 48 MHz;

The user can connect to the PDBaseII via analysis software that enables the visualization of each *pulse waveform* acquired as shown in figure 3.15a. The *pulse spectrum* is derived by the Fast Fourier Transform (FFT) over the pulse waveform. These plots



Figure 3.14: Techimp PDBaseII acquisition unit.

are both used for the creation of the T - F map that plots each acquired pulse based on the equivalent time-length and equivalent frequency as shown in 3.15d. Every recorded pulse is also displayed in a phase resolved pattern resulting in a *Phase Resolved Partial Discharge (PRPD)* pattern that is very useful for defect recognition in AC applications.

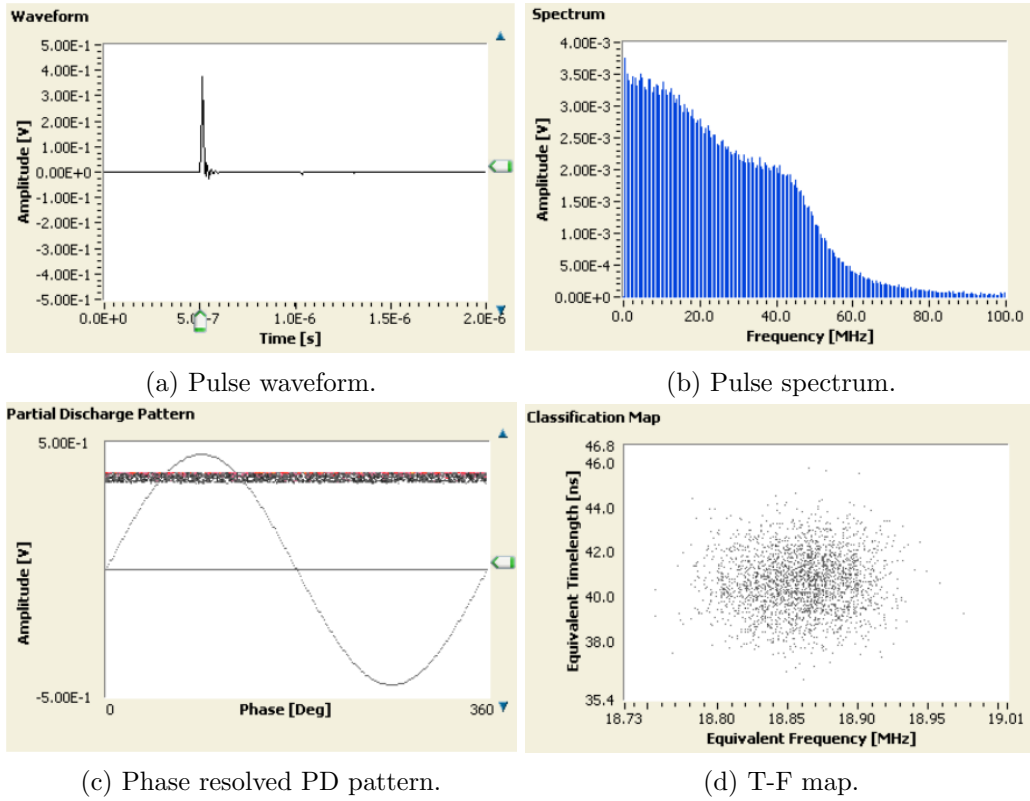


Figure 3.15: Different visualizations of PD pulses.

The PRPD pattern used to display multiple discharges displays these based on PD magnitude and phase of occurrence. The intensity of multiple discharges is represented by a colour scale as displayed in fig. 3.16 with black corresponding to an intensity of a single discharge, while blue to 40 or more pulses.

The accompanying software for the PDBaseII is specifically designed for PD detection in AC applications. DC analysis of the PD captured by the PDBaseII was done in MATLAB with the extracted pulse waveform data in combination with the discharge time.



Figure 3.16: Techimp PDBaseII intensity scale.

3.3.2 Agilent E4403B

The Agilent E4403B is a Spectrum Analyser (SA) with a working frequency range from 9 kHz to 3 GHz. The SA can display the spectrum over the whole frequency span in *full span mode* but also in a tunable narrower span. Using the narrowest span to use as Resolution Bandwidth (RBW) over a certain frequency is named the *zero-span mode*.

The fundamentals of SA operation are described in detail in chapter A. Terms concerning the SA used in this section are explained in-depth in appendix A.

The SA was only used in combination with the UHF antenna. The high frequency content of the signals measured by this sensor are lost by the limited bandwidth of the PDBaseII. The internal antenna is connected to the SA via a low losses coaxial cable. The signal is amplified by a pre-amplifier for further processing. The pre-amplifier has a flat 30 dB gain over the frequency range of interest which for our measurement is up to 3 GHz. The responses of the amplifiers used are shown in appendix B.



Figure 3.17: Agilent E4403B spectrum analyzer.

The SA is a digital device with a finite amount of sampling points. The frequency spectrum is calculated by averaging the frequency content of the input signals within the *sweep time*. In the ideal case the input signals should be stable and continuous within the time of a sweep, but partial discharges have short impulses and have a stochastic nature. For optimal detection of PD depending on the type of PD measured the research of S. Meijer [4] has shown that the following parameters must be changed accordingly:

- Sweep Time (ST)
- Total time of measurement
- Time domain settings

Sweep time

The time required for the local oscillator to scan the signal across the desired span of frequencies within the RBW is called the ST.

The full spectrum of impulse signals are difficult for a SA to acquire. This because of the low rate of occurrence of these signals and that RBW filter of the SA is made up of electronic circuits that require a discrete time to charge and discharge. Decreasing the

frequency span will result in greater accuracy but at a loss of the frequency spectrum measured. Increasing the ST taking into account that the average of the spectrum is displayed yields a better result. An investigation into the influence of the ST on the detection of impulse signals on a HP8590L SA has been done in further research of Meijer[49].

Total time of measurement

The stochastic nature of PDs results in many variations of the captured frequency spectrum during each ST. Averaging multiple sweeps of discharge activity diminishes the stochastic nature. The recurring frequencies will become more important while single disturbances less.

Time domain settings

The SA can also be employed for time domain analysis of PD. Measuring in zero-span mode within the frequency content of PDs it becomes possible to obtain phase resolved patterns in AC or time resolved patterns in DC.

3.3.3 Tektronix DPO7354C

The Tektronix DPO7354C is a digital oscilloscope with 4 input channels that can be recorded simultaneously. The signal waveforms are sampled with a sampling rate of up to 40 GS/s with bandwidth modes of 3.5 GHz, 2.5 GHz, 1 GHz and 500 MHz.

The specifications of this oscilloscope make it an ideal detection system for capturing the fast transient nature of the UHF waveform accurately. By applying a trigger level above the noise level initial separation of noise from the PD waveforms becomes possible.

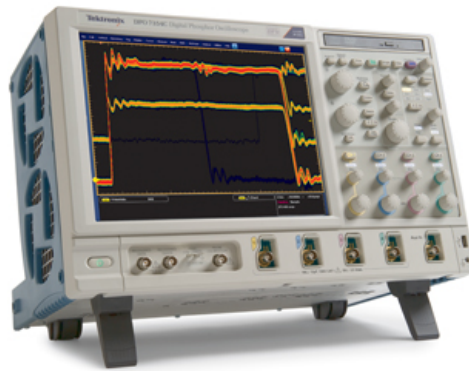


Figure 3.18: Tektronix DPO7354C Oscilloscope.

For PD analysis in DC the time domain information of discharges is important. The FastFrameTM segmented memory acquisition mode with a capture rate of more than 310.000 *wfm/s* result in accurate waveforms with no loss of time information. The trigger level forces the oscilloscope to only capture waveforms of pertinence making it possible for patterns of discharges with a low repetition rate to be captured over a large amount of time.

Further processing is necessary with MATLAB, but with the waveform of each discharge distinguishing between different sources is easier and the frequency spectrum per signal can be derived which was not possible with the spectrum analyser.

In contrary to the other detection devices, the multiple channels of the oscilloscope allows simultaneous capture of signals from different sensors.

3.4 Noise

The measurement of PD can be influenced by disturbances that can either modify, interfere or suppress. These disturbances can be *externally generated* known as Electromagnetic Interference (EMI) or *internally generated* referred to as noise.

Sources of EMI are numerous, ranging from information sent intentionally over frequency bands (e.g. mobile telephony, radio transmission) to the switching action of power electronic instrumentation.

The dimension of the measuring circuit affects the coupling with external interferences. The large dimension of the measurement set-up used yields the larger disturbances induced by magnetically coupled interferences.

Noise in the circuit can originate from many different sources. Based on the nature of the noise source it is possible to differentiate between two types of noise:

- **Differential-mode noise**, in which the source of noise is located in series with the circuit.
- **Common-mode noise**, the noise source being external to the measurement circuit but still injects noise signals via a parallel circuit created by stray capacitances.

Reducing the effect of disturbances in the HV lab was possible to an extent by doing the experiments in a cage shielding from external disturbances. Disturbances were however also originating from inside the cage. The electronic circuitry used within or the connection to the AC grid can result in disturbances flowing through the ground loop increasing the noise level. It is advisable to keep the ground loops to an absolute minimum and in this case it was achieved by powering the detection components through insulating transformers. The insulating transformer is equipped with a shield between the primary and secondary windings as shown in fig. 3.19. This reduces the stray capacitances that cause high frequency disturbances. Improved performance have also been noticed by connecting the transformers in series.

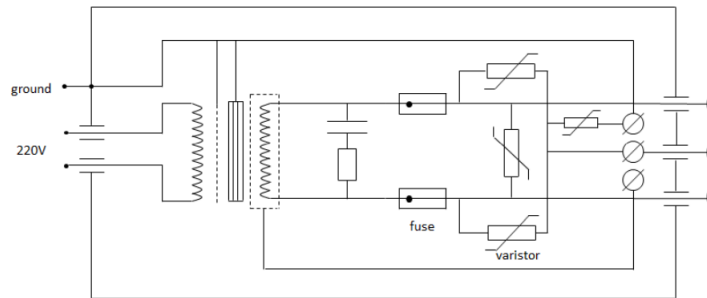


Figure 3.19: Electric circuit of the insulating transformer.

The HV laboratory is the ideal location to suppress external noise and EMI to the highest extent, but nevertheless the measurements were not disturbance-free. Measurements in the field are much more influenced by disturbances, and separation of noise by filtering based on extracted features as seen section 4.2 becomes more important.

Chapter 4

Partial Discharge Analysis

The detection and recognition of PD is chosen as a fundamental tool for the equipment risk and condition assessment. The monitoring of PDs can be done in multiple domains with a multitude of sensors. The PD monitoring behind application can however be simplified to a monitoring scheme as seen in fig. 4.1.

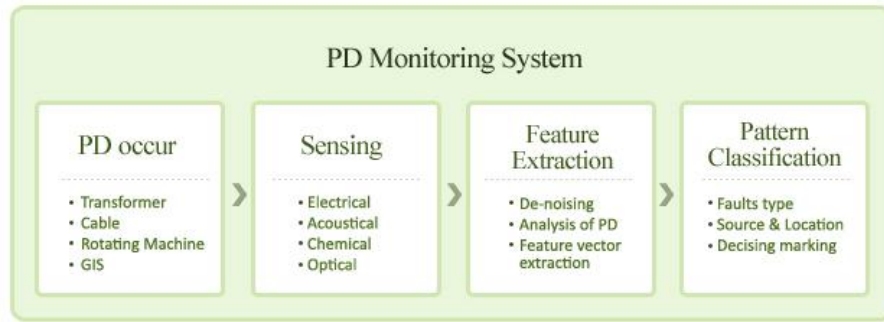


Figure 4.1: General PD monitoring scheme [3].

Detection and acquisition of PDs consists of sensing the PD occurrence through installed sensors and saving the measurements. The recognition system extracts characteristic features from the measured data for comparison to the characteristic features of know defects. Classification of the measured data ensues resulting in the recognition of the defect responsible for PD.

4.1 PD features

The data measured from PD activity varies according to the detection system used. Depending on the type and bandwidth of the sensor and the methods used for data collection of the PD detection system, the PD data can vary greatly. The collection of this type of data using minimal signal analysis is the first step in the recognition of defects is named *direct data*.

For AC, the Cigré Task Force 15.03.08 had been established for the creation of a “standard data format for GIS PD software applications”. HVDC has not been the object of a similar study, but using this research as a reference, a list of direct data based on the method of detection is presented in table 4.1.

Certain characteristic features can be extracted from the collection of PD direct data to aid in the recognition and classification of PD source types. This data is very dependent upon the feature extraction techniques used for deriving from the direct data. As a result this list of *derived data* is non-exhaustive and a selection of possible extractable features divided into the signal information available for feature extraction is shown in table 4.2.

	<i>Direct data</i>
<i>Signal Waveform</i>	$i(t)$, time resolved PD waveform q_i , apparent charge
<i>Signal Amplitude</i>	q_{max} , discharge maximum q_{min} , discharge minimum q_{mean} , discharge mean W_p , integrated energy value
<i>Signal Sequence</i>	N , number of discharge T_i , time of discharge occurrence
<i>Signal Spectrum</i>	A , amplitude f , frequency

Table 4.1: List of data directly measured by detection systems.

4.2 Feature Extraction

This thesis researches the classification of PD based on several characteristic features and the recognition of defects in DC is based on the analysis of the pulse waveform and the pulse sequence.

4.2.1 Pulse waveform analysis

Pulse-shape parameters

The pulse shape of a PD is heavily influenced by the mechanism and the magnitude of the discharge. Also the location of the discharge and the sensor used for detection vary the shape of the pulse.

With the use of this information it becomes clear that certain wave-shape parameters should have a correlation to the parameters influencing the PD behaviour making them of interest to be extracted from the pulse.

A selection of the waveform parameters of interest are shown in fig. 4.2 and are:

- t_r , the rise time of the pulse that indicates the fast behaviour of the PD.
- P_k , the peak value of the pulse. The polarity of the signal is also within this data.
- t_d , the decay time of the waveform. The tail of the waveform can give information about charge magnitude, but also about the geometry of the circuit.

TF - map

The pulse shapes within a given measurement are heavily affected by the nature and location of the PD source. Based on this assumption a technique was developed to separate the acquired signals in clusters which are homogeneous with respect to their pulse shape.

Each waveform is synthesized by means of two quantities. The derived quantities are the equivalent time-length (T) and equivalent bandwidth (W) of the waveform. The definition of these quantities is described by Montanari et al. in [50] and expressed by eq. (4.1) and eq. (4.3).

	<i>Derived data</i>
<i>Time-based</i>	N_s , repetition rate Δt , inter-time of discharges $H(\Delta t)$, inter-time distribution Δt_{min} , minimum inter-time Δt_{max} , maximum inter-time Δt_{mean} , mean inter-time
<i>Discharge power</i>	Δq , difference q_i and q_{i-1} $H(q)$, magnitude distribution
<i>Waveform</i>	T , equivalent time-length F , equivalent bandwidth t_r , rise time t_d , decay time Pk_{max} , maximum peak Pk_{min} , minimum peak S , polarity of the signal
<i>Frequency Spectrum</i>	MP , measured power AP , average power Pk_{max} , maximum peak Pk_{min} , minimum peak N_{peak} , number of peaks

Table 4.2: Derived data based on feature extraction of signal information.

$$T^2 = \frac{\sum_{i=1}^K (t_i - t_0)^2 \cdot s_i(t_i)^2}{\sum_{i=1}^K s_i(t_i)^2} \quad (4.1)$$

K is the number of samples used for the digital representation of the waveform, t_i the time associated with the i -th sample, s_i the signal amplitude corresponding to the i -th sample in time domain and t_0 , an average weighted time of all the waveforms within the measurement as calculated in eq. (4.2).

$$t_0 = \frac{\sum_{i=1}^K t_i \cdot s_i(t_i)^2}{\sum_{i=1}^K s_i(t_i)^2} \quad (4.2)$$

In eq. (4.3) f_i is the i -th sample frequency while $X_i(f)$ is the i -th component of the signal, obtained through the FFT.

$$W^2 = \frac{\sum_{i=1}^K f_i^2 \cdot |X_t(f_i)|^2}{\sum_{i=1}^K |X_t(f_i)|^2} \quad (4.3)$$

Each pulse can be represented as a single point in a two dimensional map called the classification map. The pulses originating from identical sources form clusters within this map making it possible to separate different PDs and external disturbance sources from one another by applying fuzzy clustering algorithms [51].

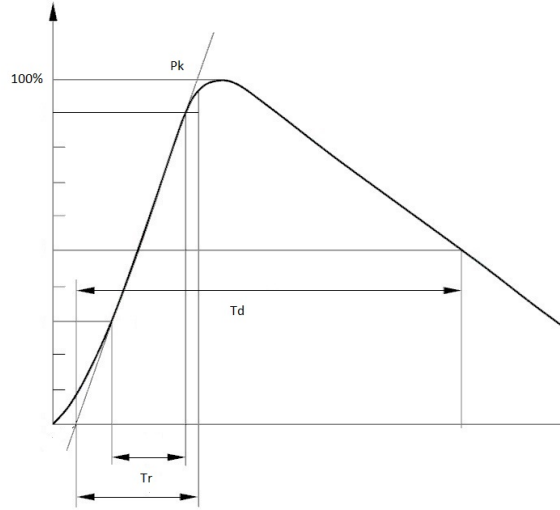


Figure 4.2: Derived data of pulse waveform.

4.2.2 Pulse sequence analysis

The pulse sequence analysis looks into the relationship of the discharge and the preceding and succeeding discharges. Measurement of PD in the pulse sequence result in the basic quantities: discharge magnitude q_i and the time of discharge occurrence t_i . An analysis with these quantities at the base results in recognition graphs specific to insulation defects.

The time/lag recovery model

The occurrence of PD causes accumulation of charge near the discharge location resulting in a drop of the local field strength. If the local field strength drops below the minimal breakdown field strength E_{min} , the discharge extinguishes. As was seen in fig. 2.14 and explained in section 2.3.4, the local electric field reaches the minimum breakdown field again in a recovery time t_R , but the discharge occurs if a starting electron is available after a time lag t_L . This time lag results in an excess field ΔE which is proportional to the discharge magnitude q . This information can be used to form the principles of the discharge model developed by *Fromm* [19] as shown in the eq. (4.4) and eq. (4.5) with the charge as a function of the time lag and the recovery time as a function of the charge.

$$q = f_1(t_L) \quad (4.4)$$

$$t_R = f_2(q) \quad (4.5)$$

The discharge occurrence at t_i has a time lag $t_{L,i}$ and affects the recovery time $t_{R,i}$. Using the basic quantities acquired there cannot clearly be differentiated between the time lag and the recovery time. The deduced quantities used are, the time between the discharge at t_i and its predecessor is $\Delta t_{pre(i)}$ and the time between the discharge and successor is $\Delta t_{succ(i)}$ of which the relation to the time lag and recovery time is shown respectively in equations (4.6), (4.7).

$$\Delta t_{pre(i)} = t_{R,i-1} + t_{L,i} \quad (4.6)$$

$$\Delta t_{succ(i)} = t_{R,i} + t_{L,i+1} \quad (4.7)$$

The range of amplitude is discretized in a number of intervals and for each element q_i of an interval the time to previous discharge $\Delta t_{pre(i)}$ and the time to successive discharge $\Delta t_{suc(i)}$ is calculated. The time to previous and successive discharges are averaged separately from each other. to calculate a mean time to previous $\overline{\Delta t_{pre}}$ and successive discharge $\overline{\Delta t_{suc}}$ as is shown in eq. (4.8) and eq. (4.9). Plotting these parameters to discharge level produces recognition graphs in which the effect of time/lag recovery can be seen.

$$\overline{\Delta t_{pre}} = \frac{1}{n} \sum_{i=1}^n (t_{R,i-1} + t_{L,i}) \quad (4.8)$$

$$\overline{\Delta t_{suc}} = \frac{1}{n} \sum_{i=1}^n (t_{R,i} + t_{L,i+1}) \quad (4.9)$$

The memory effect

The PD behaviour can also be affected by what is known as the *memory effect*. This effect is shown in the relation of the magnitude of the discharge to the magnitude of the successive discharge. Classification can be made on the graphs showing the relation between the magnitude of a discharge level q and the average magnitude of the successive discharge. The graphs can show whether the magnitude of discharges are independent of previous discharges or if there exist a positive or negative correlation between successive discharges.

The range of amplitude is discretized in a number of intervals and for each element q_{t_i} of an interval the successive time wise discharge $q_{t_{i+1}}$ exists. The successive discharges of each interval are averaged and a mean successive discharge is calculated for every discretized level of discharge magnitude as seen in eq. (4.10) with n the number of discharges within a interval.

$$\frac{1}{n} \sum_{i=1}^n q_{t_{i+1}} = \bar{q}_{suc} \quad (4.10)$$

Chapter 5

Experimental Results I: DC recognition of PD defects

For this research defects have been created to simulate the PD sources of *internal discharge*, *surface discharges* and *discharges due to floating components*. These defects have been measured in AC and DC in the TU Delft HV laboratory. The result of these measurements is presented in this chapter along with a discussion focusing on the discharge physics followed by a comparison between AC and DC.

The measurements of the PDs for both AC and DC have been done through the calibrated conventional IEC method of PD detection with the quadrupole as seen in section 3.2.1. In parallel to the calibrated measurements, a HFCT sensor has also been used for acquiring the time resolved waveforms of the PD. This has been done to verify the polarity of the PD pulse and for better separation of noise signals via the *TF-map*.

The PD measurements in AC are presented in PRPD patterns. Research on the behaviour of the types of PD in AC based on the PRPD patterns will be used to determine the validity of the defects created to simulate the different types of PD.

The discharge magnitude q and the time interval between successive discharges Δt are the basic parameters for PD detection in DC in this experiment. The PDs are represented by repetition rate (N/s) and recognition graphs showing the discharge-probability density. More intricate ways of presenting the PD data comes from knowledge of the physical discharge processes taking place for every PD and realizing that a discharge in DC is a space charge phenomena. The inception of PD is governed by the presence of an initial electron and by the electric field exceeding a threshold field for PD inception.

PDs can be affected by the discharge preceding them. This is the *memory effect* [52] of PDs which influences the charge magnitude and the time a discharge occurs. The presence of this effect affects the basic parameters revealed in the correlation of magnitude of the charge q and the average magnitude of the previous charge \bar{q}_{pre} . In the same way, the time in between the discharges results in recognition plots based on the charge q and the average time to previous discharge $\bar{\Delta t}_{prec}$ or the average time to successive discharge $\bar{\Delta t}_{succ}$. Recognition plots using these parameters are presented for each type of PD to determine whether this method can be used for classification of the defect in DC.

5.1 Floating Components

To simulate the discharges of floating components inside the GIS a conductive metallic part was suspended from the inner conductor by a fishing line to become electrically floating as depicted in fig. 5.1.

The metallic part has a smooth surface so the electric field is not locally enhanced by protrusions. The part does however have a length of 40 mm in the direction of the electric

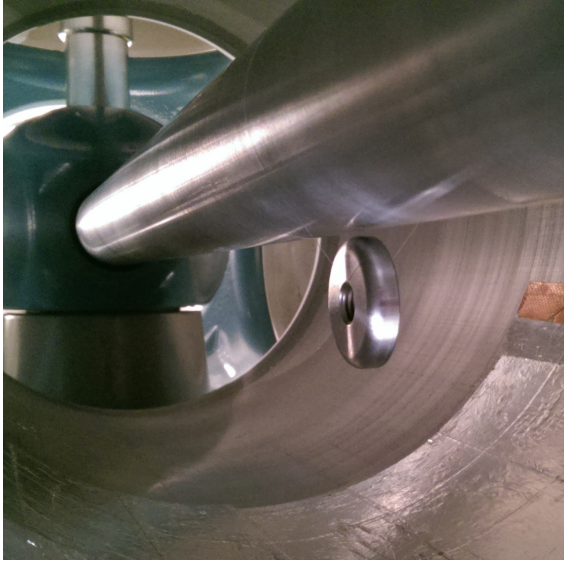


Figure 5.1: The metallic component suspended from the inner conductor by fishing line.

field resulting in a field distortion as the voltage of the whole component is considered equal.

The insulating gases used during this experiment are humid air at 1 bar and a more realistic gas formulation for the GIS of SF_6 at 1.1 bar.

The distance of the metallic component is taken in reference to the inner conductor and is always chosen closer to the inner than the outer conductor. The reason for this is that the discharges are as a result of the electric field and are more likely to occur near the inner conductor at lower voltages as was stated in section 3.1.1.

5.1.1 AC Voltage

The trends of the discharge magnitude and the repetition rate per voltage period of the discharges for both air and SF_6 are shown fig. 5.2. The PDs are as a result of the potential difference between the conductor and the floating component exceeding the breakdown strength. A discharge occurs in the high field region during which a charge transfer takes place between the conductor and the electrically floating particle. The transfer of charge reduces the local electric field and the PDs stops as the voltage difference ΔV decreases below inception level.

Figure 5.2 shows an increasing repetition rate as a result of a voltage increase for both gases. Within a voltage cycle, the difference in voltage between the floating component and conductor increases faster resulting in more discharges. The charge magnitude as seen in fig. 5.2a and fig. 5.2b show a constant discharge level for varying voltages. This discharge level is determined for a big part by the breakdown strength of the gas gap and is for SF_6 larger than for air.

With this type of defect it was noticed that there was no difference between the inception and extinguishing level. For this defect the voltage difference between the floating component and the electrode needs to exceed the breakdown strength of the region resulting in an inception voltage that has a single discharge in the positive half of the waveform and also one in the negative half of the waveform. A comparison of the inception voltages with varying distance of the floating component to the electrode and the type of gas is shown in table 5.1.

The discharge pulses of the floating component ignite in the leading quadrants of the positive and negative half cycles of the voltage wave visible in fig. 5.3. At these points

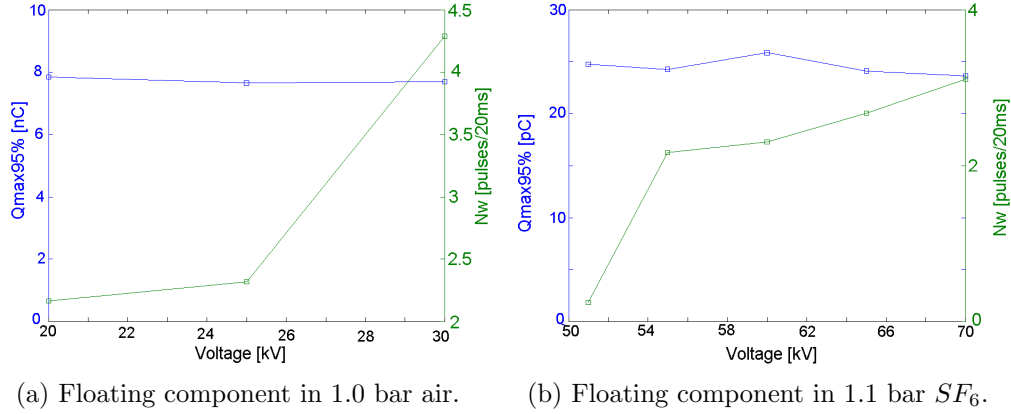


Figure 5.2: Trends of the 95% discharge magnitude and 50 Hz repetition rate at different voltage levels.

	d = 4mm	d = 7mm
Inception V_{rms} [kV]		
1.0 bar air	20	45
Inception V_{rms} [kV]		
1.1 bar SF_6	51	56

Table 5.1: Comparison of the inception voltages of floating components discharges for different gas formulations and distances to electrode.

the difference in potential exceeds the breakdown strength first resulting in discharges of similar magnitude.

In the case of the gap being symmetrical and no time lag present, the discharges would occur at the same point on the phase of the voltage, but as we clearly see in figure 5.3b, this is not the case for this defect. A characteristic curved pattern is visible in which discharges occurring at high voltages on one polarity result in a discharge at a lower voltage at the other polarity and vice versa.

The application of higher voltages lead to more repetitions per cycle while the discharge magnitude stays constant as can be seen in figure 5.4a. The pattern as a result of a progressive advance or retard of the point of discharge on the cycle is still visible.

The PRPD patterns of the floating component at different voltage levels are shown in table 5.2. The discharges of positive and negative polarity as a result of the AC voltage waveform have been analysed separately from on another. The magnitudes of the PDs is constant for different voltages. Looking at the intensity of the PRPD pattern, the 1st and 3rd quadrant of the voltage waveform are the most likely times for discharges to occur.

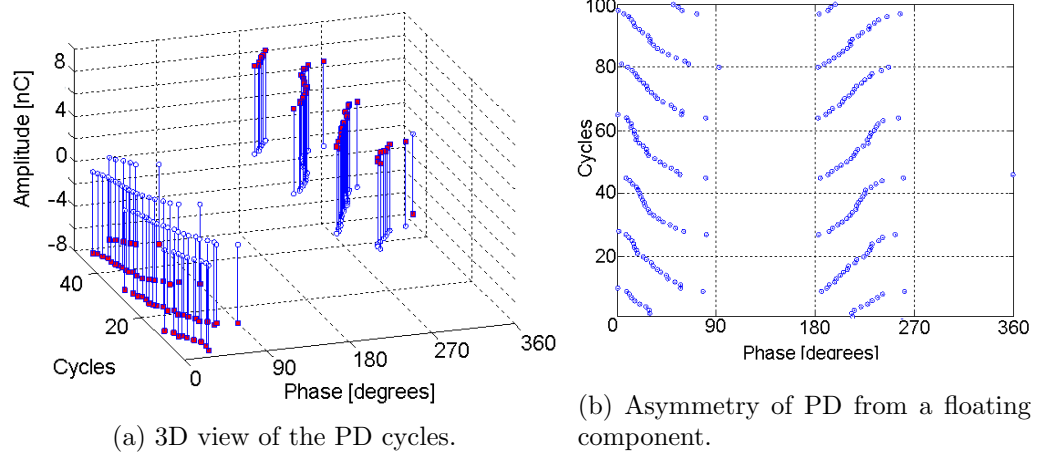


Figure 5.3: Cycles of PD from a floating component at 20kV in 1.0 bar air.

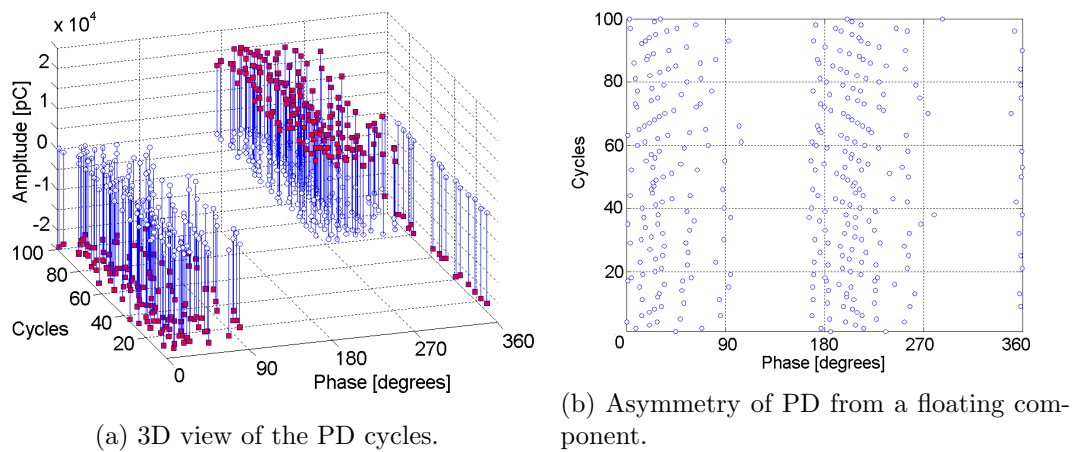
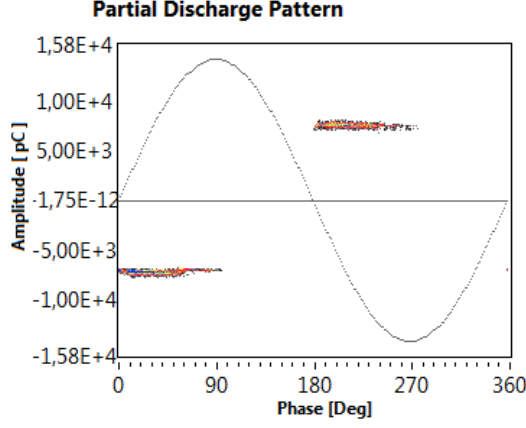
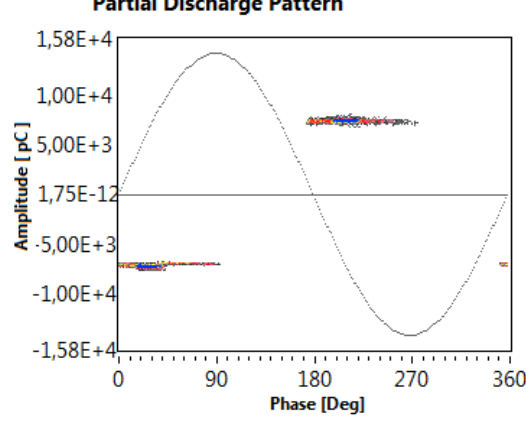
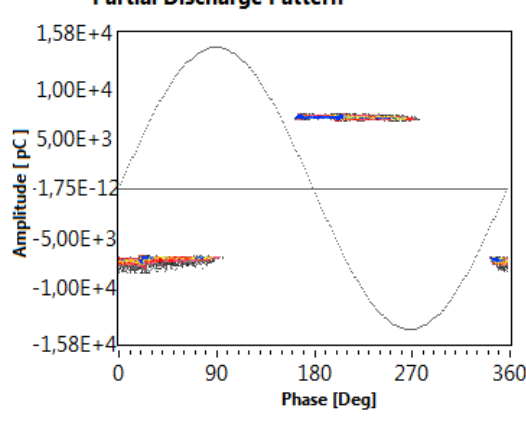


Figure 5.4: Cycles of PD from a floating component at 70kV in 1.1 bar SF_6 .

Table 5.2: Phase-resolved partial discharge patterns for a floating component in 1 bar air with distance of 4 mm from inner conductor.

Discharge data			PRPD pattern	
	Pos cycle	Neg cycle		
Q_{max} [pC]	8139	7769		
Q_{mean} [pC]	7679	7214		
Q_{min} [pC]	6906	6659		
Repetition rate [N/s]	52.819	55.211		
V_{rms} [kV]	20			
Q_{max} [pC]	8139	7646		
Q_{mean} [pC]	7512	7176		
Q_{min} [pC]	6906	6659		
Repetition rate [N/s]	58.943	60.534		
V_{rms} [kV]	25			
Q_{max} [pC]	7646	8506		
Q_{mean} [pC]	7270	7238		
Q_{min} [pC]	6782	6659		
Repetition rate [N/s]	107.931	106.256		
V_{rms} [kV]	30			

5.1.2 DC Voltage

Within the voltage range of the DC source no PDs were detected while the GIS was filled with SF_6 gas. The following measurements were accomplished in air at atmospheric pressure. Taking into account that the DC voltage range is limited, it was decided to suspend the floating component 4 mm from the inner conductor for the DC measurements.

Negative DC voltage

The application of negative voltage resulted in discharges measured around 50 kV. These started initially with a very low discharge magnitude and a very low repetition rate as shown in table 5.3. As the applied voltage increased, the discharge magnitude increased exponentially along with the repetition rate of the discharges.

Voltage [kV]	Q_{min} [pC]	Q_{max} [pC]	$Q_{max95\%}$ [pC]	Repetition rate [N/s]
-50	27	164	164	0.009
-58	34	6507	5140	2.168
-60	24	50317	40808	206.109
-65	22	12898	6194	7350.379

Table 5.3: Discharge magnitudes of floating components in 1.0 bar at different negative DC voltage levels. Detection by means of quadrupole calibrated according to *IEC 60270*.

The trend plot in fig. 5.5 shows a drop in charge magnitude increasing the voltage beyond 60 kV. This is due to the limited power the DC power supply can deliver. The feedback system of the power supply will try to reaching the set voltage level, but as the amount of necessary injected power increases with increasing PDs, the voltage setting is never reached and even drops below 60 kV which has an effect on the charge magnitude.

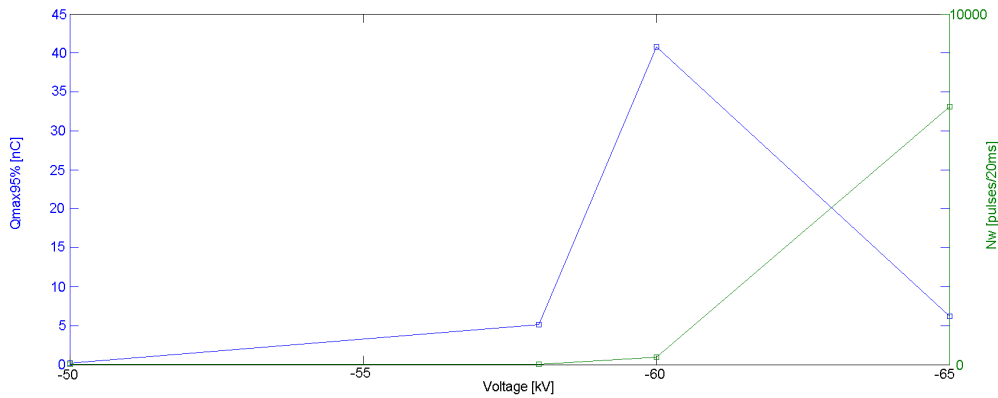


Figure 5.5: Trend lines of the 95% discharge magnitude and repetition rate at different negative DC voltage levels 1.0 bar *air*.

The time resolved pattern of the floating component PD at 58 kV in fig. 5.6 shows two distinct discharge levels. The PDs are classified as discharges with a magnitude below 2000 pC and above 4000 pC.

The PD originates at the inner conductor and makes its way to the floating component. A charge transfer occurs affecting the surface charge of the discharge surfaces. The electric field in the gas gap drops below the critical level and the discharge extinguishes.

It was noticed that the transfer of charge is not achieved by a single discharge, but accomplished through a rush of partial discharges within a small amount of time called *discharge trains*. The many discharges in a sequence can be identified as the vertical lines visible in fig. 5.6.

Figure 5.7 zooms in on a single discharge train. Two levels of discharge magnitude are clearly visible. The discharge trains start with a discharge of high magnitude and continue alternating between discharges of high and low magnitude until the discharge train stops.

The DC recognition graphs result in valuable information for recognizing PDs of floating components in DC. The magnitude distribution in fig. 5.8b clearly shows the two

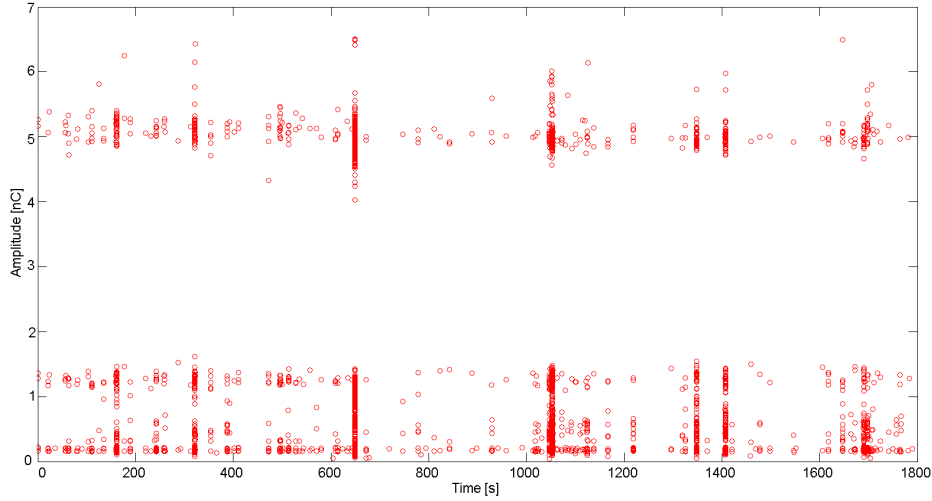


Figure 5.6: Time-resolved PD pattern of floating component at -58kV in 1.0 bar *air*.

different magnitudes of discharges taking place and that those of low magnitude are more numerous.

The plots of the mean successive discharge magnitude as shown in fig. 5.8a show the sequence of these discharges in more detail. Three areas of discharge magnitudes become are of interest:

- 0 - 1000 pC, the successive discharges are in an average magnitude of higher than 2000 pC indicating that these discharges are frequently succeeded by a discharge of the high magnitude.
- 1000 - 2000 pC, sees an average discharge magnitude of around the same discharge magnitude which indicates that these discharges are succeeded by similar discharges.
- above 4000 pC, are the discharges of high magnitude. The average successive magnitude clearly shows that these are most likely followed by the discharges of the lower discharge magnitude. One point is the exception showing a high average discharge magnitude succeeding a discharge of 6500 pC. This however is a very rare occurrence as seen in the discharge magnitude distribution.

Information concerning the time between the discharges can be gathered from fig. 5.8c and fig. 5.8d. The mean time to preceding discharge plot in fig. 5.8c shows high average times for values between 4800 pC and 6000 pC. This is an indication of discharge trains starting with discharges of these magnitudes. The higher time in between the discharges allow for longer DC charging that result in increased PD magnitudes.

Below 1000 pC, average times are also calculated that are exceeding the times measured within the discharge trains. This is a contribution as is visible in fig. 5.6 of single discharges taking place in between these discharge trains.

The plot of the mean time to successive discharge in fig. 5.8d shows low average times for discharges of above 4000 pC. These PDs are followed within short succession by another discharge.

Magnitude levels below 2000 pC have high average times. These discharges are most likely at the end of a discharge train or are single discharges. The time to another single discharge or discharge train results in the high average time.

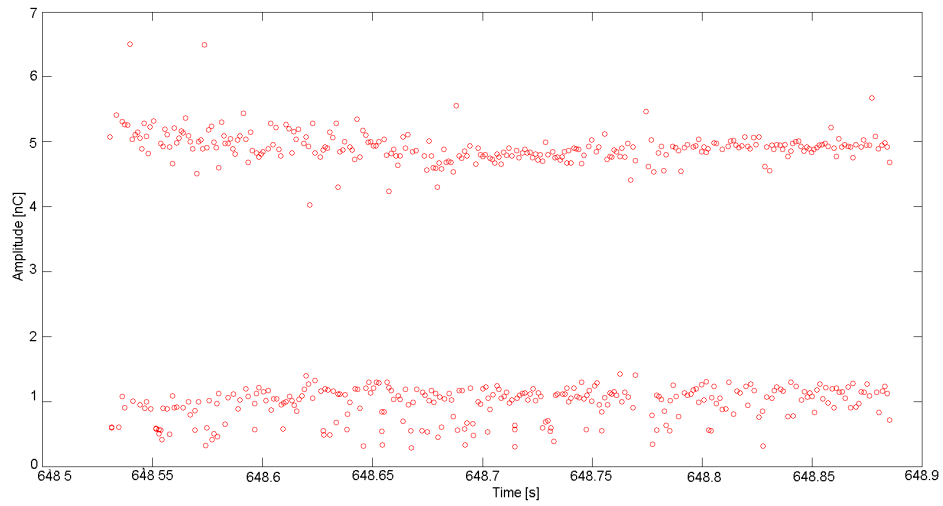


Figure 5.7: Time-resolved pattern of rush of floating component PD activity at -58kV in 1.0 bar *air* as shown in fig. 5.6.

The recognition plots follow the same behaviour for the higher voltages. The repetition rate of the discharge trains increases and as the voltage increases the clear separation of high and low magnitude discharges disappears gradually.

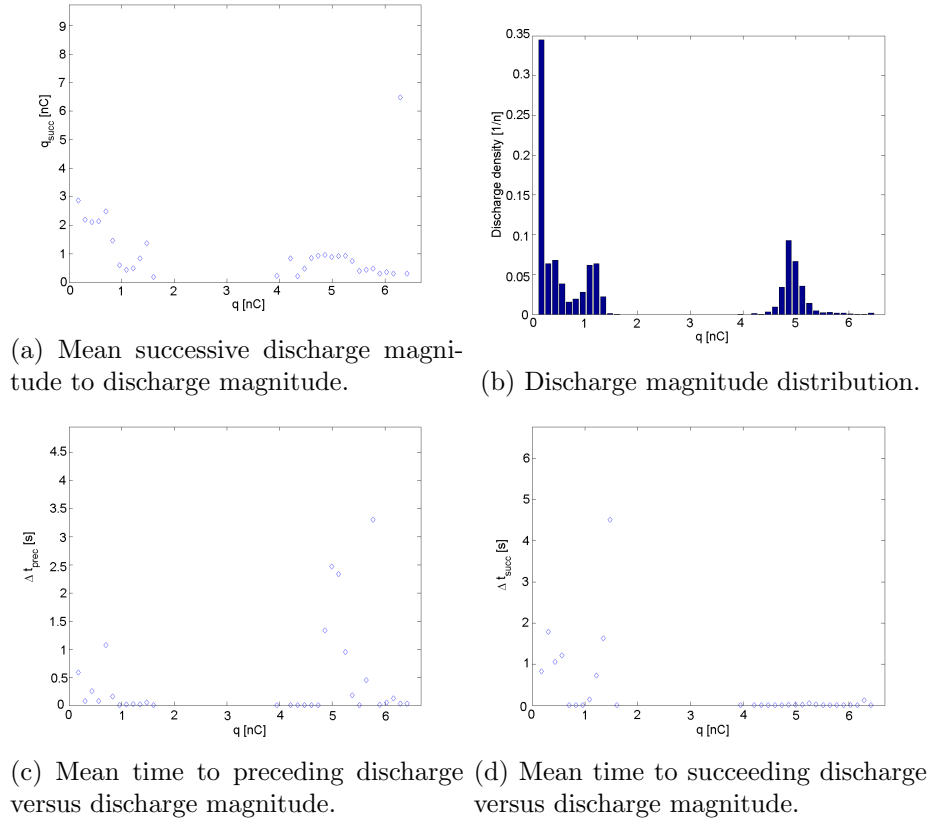


Figure 5.8: DC recognition plots for discharges of a floating component at -58kV in 1.0 bar *air*.

Positive DC voltage

Measurements of the floating component with positive DC voltage applied were inconclusive for DC PD recognition. The reason being that extremely large discharges were measured that could not be attenuated enough to prevent clipping of the measuring instrument and resulted in inaccurate captures of discharges. These high discharges coincided with loud cracking sounds audible outside the GIS.

The inception voltage of these discharges is around 55 kV and a time resolved discharge pattern shows a few of these discharge trains igniting at an applied voltage of 55 kV in fig. 5.9. The sensor used was the HFCT sensor and based on the waveforms some of the captured points were removed from the plot. With these modifications the plot still shows discharge trains and also a double layer of PD magnitudes as was seen under negative DC stress.

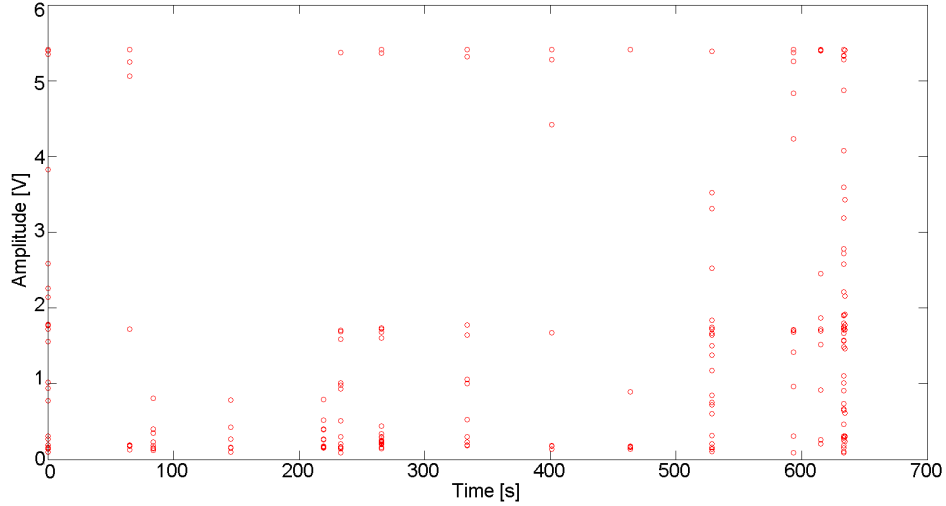


Figure 5.9: Time-resolved PD pattern of floating component at 55kV in 1.0 bar *air*.

5.1.3 Discussion

The inception levels for PDs in DC are much higher than for AC. The trends of the increasing voltages for AC have shown a constant magnitude for the PDs for both polarities. The repetition rate did increase with increasing voltages for AC, which was also the case for the PDs in DC. Unlike the PDs of AC, the magnitude of the discharges in DC did increase very fast with increasing voltages.

The information of the DC recognition plots is dominated by the discharge trains. In DC, the conditions for PD are much less apparent resulting in higher charge build-up before PDs take place. The charge deposited by the discharges affect the local electric field and disrupt the condition for PD. A discharge train results and for the case of a floating component in negative DC at a distance of 4 mm from the inner conductor a double layer of discharges emerges as seen in fig. 5.7. The electron avalanches leave behind a cloud of positive ions. Driven by the electric field this cloud will move toward the cathode locally distorting the field as explained in section 2.2.3 seen in fig. 2.5. A local field exceeding the breakdown value can result in the gas gap breaking down as explained for *corona discharges* in section 2.3.3. The shielding effect reduces and the next discharge again bridges the gap between the conductor and the floating component.

Measurements of a floating component with a distance of 7 mm have shown a decreased effect of the cloud of positive ions as seen in the time-resolved pattern of the discharges shown fig. 5.10a. The discharges increase with the distance along with the positive ions. The time of travel however increases for the ions and within that time recombination and diffusion of the ions occur decreasing the distortion of the positive ion cloud local electric field.

The vertical resolution of the PD detector when capturing signals in the nano Coulomb range made it difficult to separate the discharge of low magnitude from possible noise signals. There was however an increase measured in low magnitude PD activity during the discharge trains. This hints that there is still double level of discharges albeit much smaller as the PDs did not exceed 500 pC.

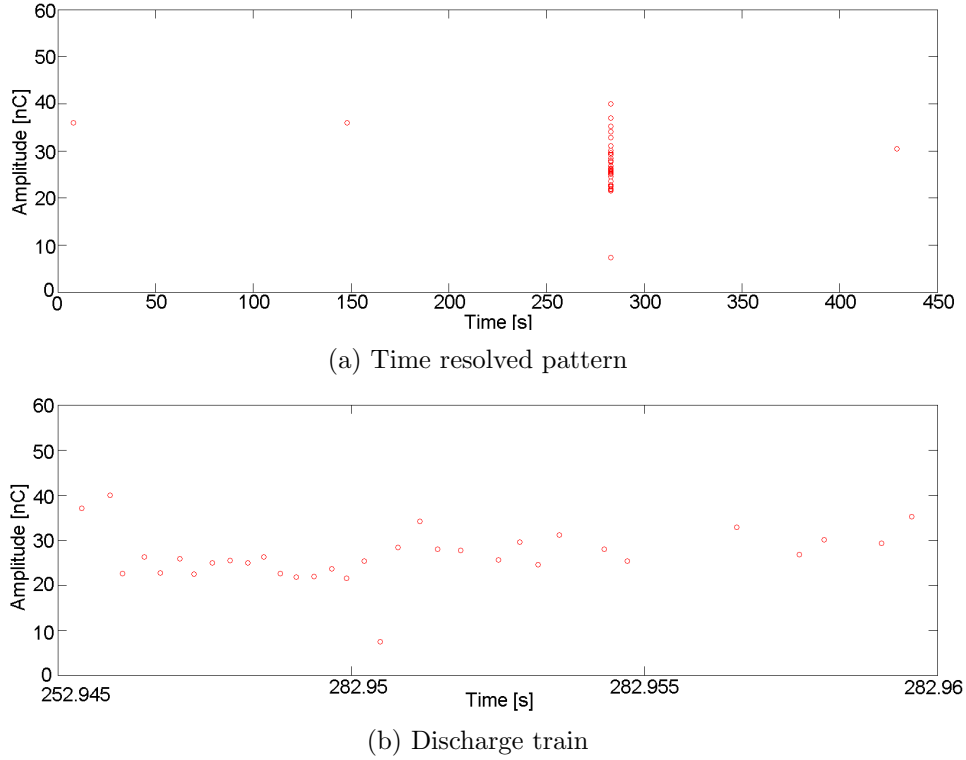


Figure 5.10: Floating component PD activity at -70kV in 1.0 bar *air*.

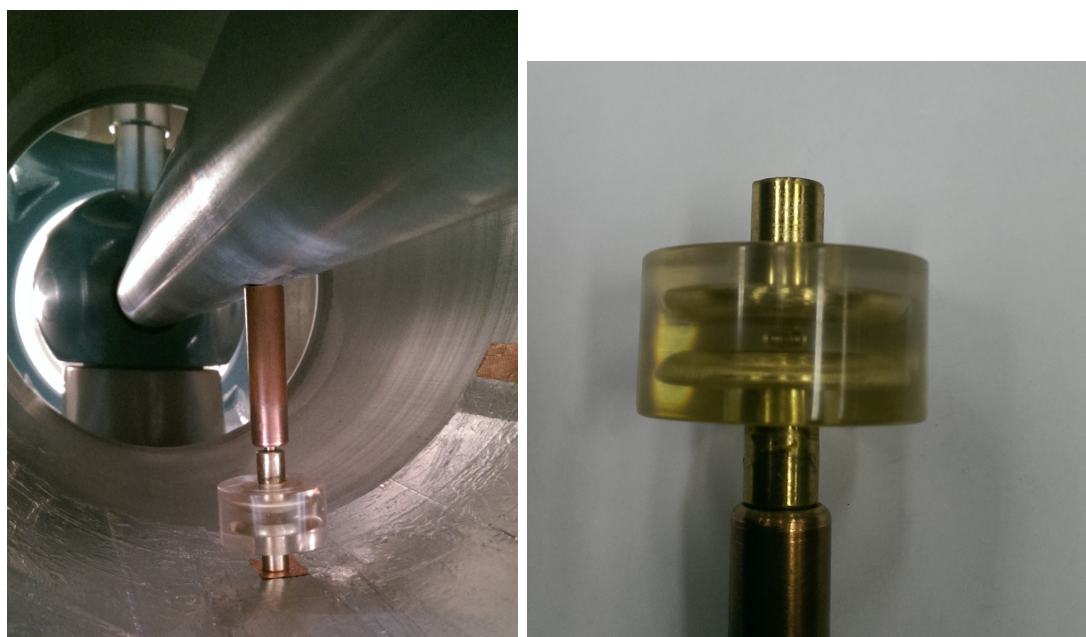
5.2 Internal Discharges

The simulation of internal discharges within a spacer have been achieved by connecting an epoxy spherical void sample to the inner and outer conductor of the GIS as seen in fig. 5.11a. The sample consists of two round shaped stainless steel electrodes (of pseudo-Rogowski profile) cast into epoxy to have an even distribution of electric field lines in the centre of them. In between the electrodes, an air cavity is found in the epoxy which is the defect to measure.

The air cavity results in a higher electric field within the air bubble as a result of the lower permittivity than the adjacent epoxy region. The local electric field within the sample is not dependent on the type of gas in the GIS and the inception voltage of the internal discharges was sufficiently low, thus all the measurements have been done in air at atmospheric pressure. Furthermore it must be noted that the sample used in the laboratory had been used in the past for many experiments and thus considered to have a very aged cavity that is assumed to behave different from a virgin cavity.

5.2.1 AC Voltage

The inception voltage of the defect under AC is 6.3 kV and internal discharges were measured ranging up to a few nC. Upon lowering the voltage it was noticed that the discharges disappeared at an extinguishing voltage of 5.5 kV. The trends of the measurements at different voltage levels are displayed in fig. 5.12. Because of the size of the cavity and the discharges of great magnitude being measured it was decided to not stress the sample to a great extent. The voltages levels have been chosen quite close to one another and looking at the repetition rate no great differences are measured. However, the 95% discharge magnitude behaves rather differently than expected. As seen in the trend the magnitude of the discharges initially increases with the voltage applied from 7 kV to 9 kV, but before



(a) The internal cavity sample connected to the inner and outer GIS conductor.

(b) Close-up of the internal cavity.

Figure 5.11: The epoxy spherical void components used for simulating internal discharges.

reaching 11 kV the magnitude drops. These differences are also noticed in the PRPD patterns with their parameters separated for negative and positive voltage in table 5.4.

As was shown in section 2.3.4 the occurrence of PD within the cavity relies on two basic conditions. That the electric field within the cavity has reached the inception field, but also that an initial electron is available to start a discharge mechanism. For polymer type insulation materials there is an inherent shortage of these electrons thus a time lag occurs in which the voltage increases further across the void before a starting electron is available. The resulting PRPD patterns shows discharges taking place over the whole phase where the voltage across the cavity exceeds the inception level. As seen in all the patterns the maximum amplitude in phase of the discharges follow the voltage waveform. This is due to over-voltages of the spherical cavity introduced by the time lag.

In the PRPD waveform at 9 kV, the discharges are occurring very grouped at higher magnitudes than measured at 11 kV. Despite this, the repetition rate of the PDs at 11 kV is higher. This could be to an increase of initial free electrons as a result of field emission from the cavity surface. The void accumulates de-trappable charges from the previous PD along the surface. The change in polarity results in an electric field that forces the charge into the cavity becoming a starting electron. This type of electron generation also explains the phase of the grouping of the discharge as seen in the PRPD patterns of the 9 kV and 11 kV voltage levels.

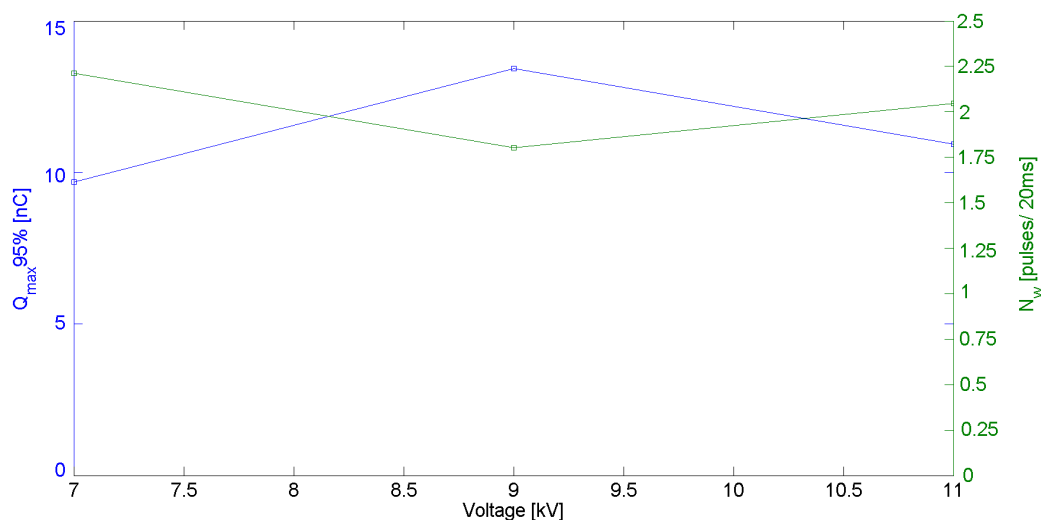


Figure 5.12: Trend lines of the 95% discharge magnitude and 50 Hz repetition rate at different voltage levels of spherical cavity sample.

Table 5.4: Phase-resolved partial discharge patterns for internal discharges in spherical cavity sample.

Discharge data

	Pos cycle	Neg cycle
Q_{max} [pC]	10442	8793
Q_{mean} [pC]	8231	6146
Q_{min} [pC]	1099	687
Repetition rate [N/s]	47.816	62.616
V_{rms} [kV]	7	

PRPD pattern

Partial Discharge Pattern

PRPD pattern for 7 kV. The plot shows Amplitude [pC] on the y-axis (ranging from -1.76E+4 to 1.76E+4) versus Phase [Deg] on the x-axis (ranging from 0 to 360). The data points form two main clusters: one in the negative phase (around 270 degrees) and one in the positive phase (around 90 degrees). The amplitude ranges from approximately -1.76E+4 to 1.76E+4 pC.

Partial Discharge Pattern

PRPD pattern for 9 kV. The plot shows Amplitude [pC] on the y-axis (ranging from -1.76E+4 to 1.76E+4) versus Phase [Deg] on the x-axis (ranging from 0 to 360). The data points form two main clusters: one in the negative phase (around 270 degrees) and one in the positive phase (around 90 degrees). The amplitude ranges from approximately -1.76E+4 to 1.76E+4 pC.

	Pos cycle	Neg cycle
Q_{max} [pC]	14425	14288
Q_{mean} [pC]	11826	11749
Q_{min} [pC]	1923	3435
Repetition rate [N/s]	45.22	44.902
V_{rms} [kV]	9	

Continued on next page

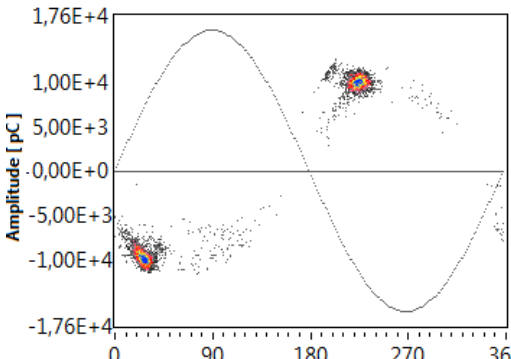
Table 5.4 – Continued from previous page

Discharge data

	Pos cycle	Neg cycle
Q_{max} [pC]	12639	11540
Q_{mean} [pC]	10047	9555
Q_{min} [pC]	2885	1374
Repetition rate [N/s]	50.591	51.881
V_{rms} [kV]	11	

PRPD pattern

Partial Discharge Pattern



The figure is a Partial Discharge Pattern (PRPD) plot. The vertical axis is labeled 'Amplitude [pC]' and ranges from -1,76E+4 to 1,76E+4, with major ticks at -1,76E+4, -1,00E+4, -5,00E+3, -0,00E+0, 5,00E+3, 1,00E+4, and 1,76E+4. The horizontal axis is labeled 'Phase [Deg]' and ranges from 0 to 360, with major ticks at 0, 90, 180, 270, and 360. The plot shows a dense distribution of data points forming two main clusters. One cluster is located in the positive phase region, centered around 90 degrees and 1,00E+4 pC. The other cluster is located in the negative phase region, centered around 270 degrees and -1,00E+4 pC. Both clusters are highlighted with red circles. A dashed sine wave is overlaid on the plot, representing the AC voltage waveform.

5.2.2 DC Voltage

Negative DC voltage

The inception voltage for PDs inside the cavity of the epoxy sample is -24 kV. This is the same level at which the PDs extinguish.

An increase in voltage sees an increase in the discharge magnitude and also a slight rise in the repetition rate as is visible in table 5.5. The trend lines of the 95% discharge magnitude and the repetition rate are displayed in fig. 5.13.

Voltage [kV]	Q_{min} [pC]	Q_{max} [pC]	$Q_{max95\%}$ [pC]	Repetition rate [N/s]
-24	17	75	75	0.071
-28	15	742	304	0.132
-32	7	914	523	0.112
-36	10	1096	568	0.151

Table 5.5: Discharge magnitudes of a spherical cavity sample at different negative DC voltage levels. Detection by means of quadrupole calibrated according to IEC 60270.

The time resolved pattern in fig. 5.14 shows a concentration of discharges at low discharge magnitudes but also a large scatter in the magnitude. The aged cavity walls of the void are expected to have a higher surface conductivity as a result of carbonization and chemical changes.

In cavities the low availability of starting electrons also influences the repetition rate and the time to build-up charge. The discharge magnitude distribution in fig. 5.15b shows the low probability of the high discharges, the PDs that haven't been influenced by the charge decay.

The characteristic graph between the *mean successive discharge magnitude to the discharge magnitude* shown in fig. 5.15a shows no correlation between the parameters. For the PDs in this cavity, the magnitude is largely independent of the previous PD that has taken place. A high discharge results in a bigger transfer of charge and with it a bigger accumulation of charge that influences the time to next PD by an increase in time lag.

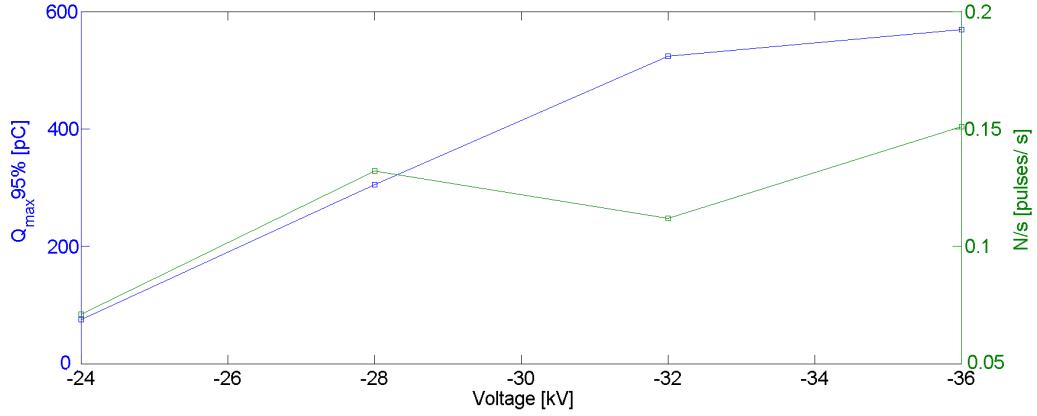


Figure 5.13: Trend lines of the 95% discharge magnitude and repetition rate at negative DC voltage levels for a spherical cavity sample.

For this type of defect however the magnitude of the discharge again seems independent to the time preceding the PD as is visible in fig. 5.15c in the same way that the magnitude of the discharge seems independent of the time to the next PD in fig. 5.15d. This is as a result of the charge decay greatly influencing the charge accumulation taking place inside the cavity resulting in recognition plots that differ from those of virgin cavities where the charge decay is less.

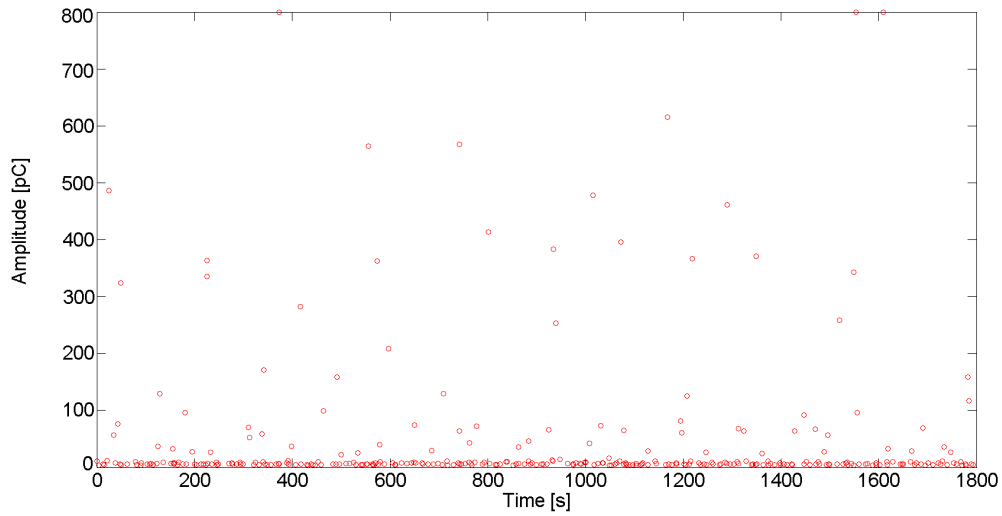
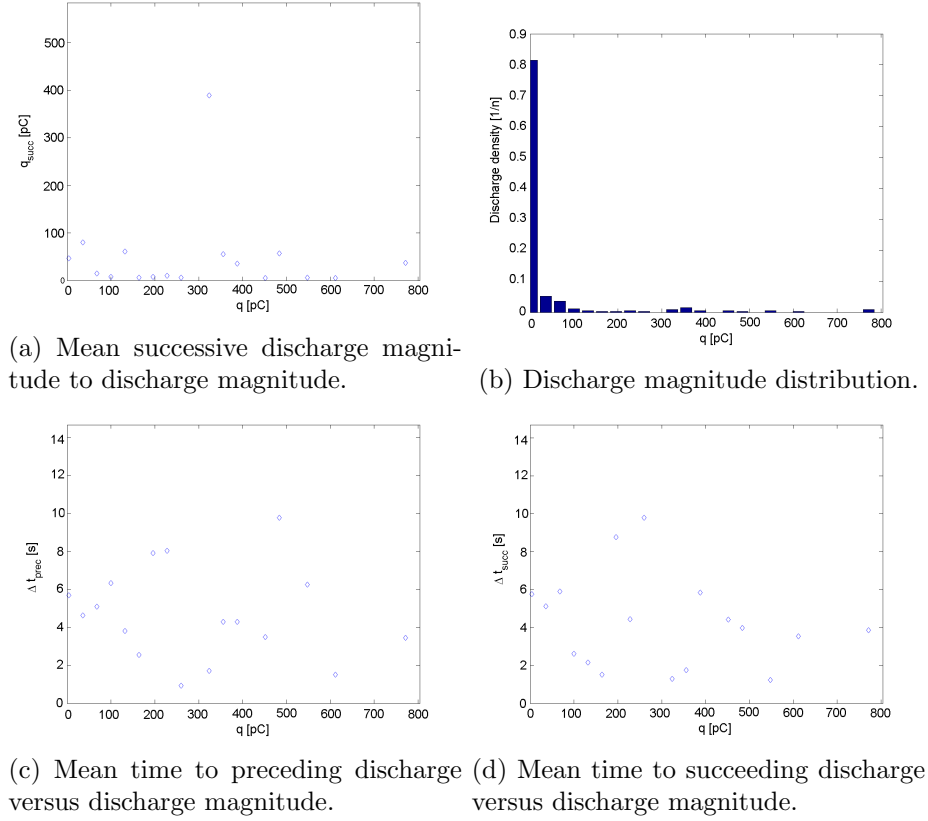


Figure 5.14: Time-resolved pattern of discharges in a spherical cavity sample at -30kV .


 Figure 5.15: DC recognition plots for discharges of a spherical cavity sample at -30 kV.

Positive DC voltage

For positive DC voltage, the inception and extinguishing voltage are both 17 kV. These internal discharges behave in the same manner as in the case of negative applied voltage with an upward trend in the discharge magnitude and also a slight rise in the repetition rate as is visible from the data in table 5.6 and fig. 5.16.

Voltage [kV]	Q_{min} [pC]	Q_{max} [pC]	$Q_{max95\%}$ [pC]	Repetition rate [N/s]
17	2	132	95	0.052
19	5	104	101	0.083
23	3	269	143	0.067
25	3	304	175	0.086
30	4	595	234	0.151

Table 5.6: Discharge magnitudes of a spherical cavity sample at different positive DC voltage levels. Detection by means of quadrupole calibrated according to IEC 60270.

Looking at the time resolved pattern of the discharges as shown in fig. 5.17 and the discharge magnitude distribution in fig. 5.18b it becomes visible that the PDs are concentrated at low discharge magnitudes with the number PDs decreasing with the PD magnitude.

As was also seen for negative DC, there seems to be no correlation between the discharge magnitude and the mean successive discharge magnitude as portrayed in fig. 5.18a.

Research by Fromm [19] on cavities has shown that the PD magnitude in cavities is determined by the *time lag*.

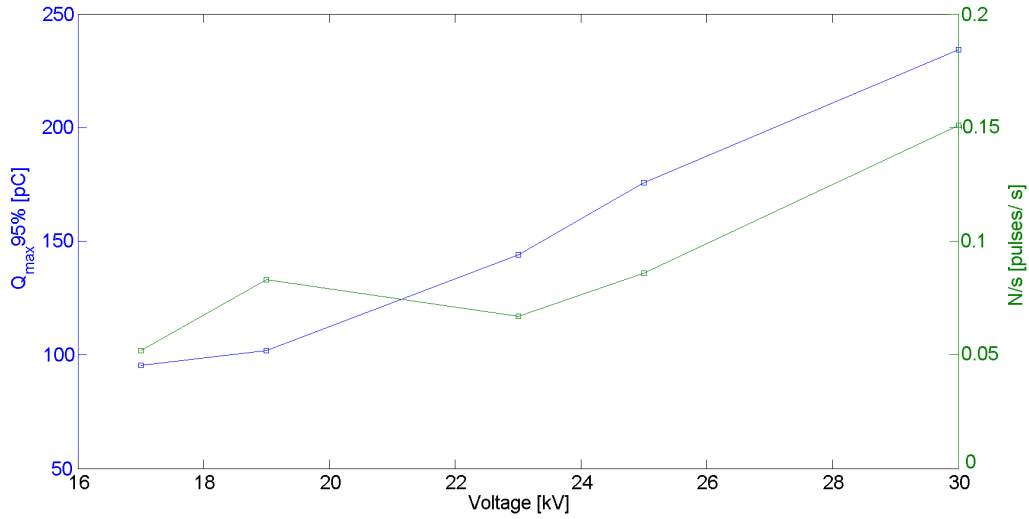


Figure 5.16: Trend lines of the 95% discharge magnitude and repetition rate at positive DC voltage levels for a spherical cavity sample.

The recognition graphs in average time to previous and successive discharge to the discharge magnitude in fig. 5.18c and fig. 5.18d for the PD magnitude below $< 400\text{pC}$ show a positive correlation to the time. An increase in the time lag Δt_{pre} leads to a higher electric field at discharge resulting in an increased magnitude of the PD. The magnitude of a PD is also related to the charge transfer and thus the deposited charge on the surface. For the successor PD this results in an increase in the time Δt_{succ} .

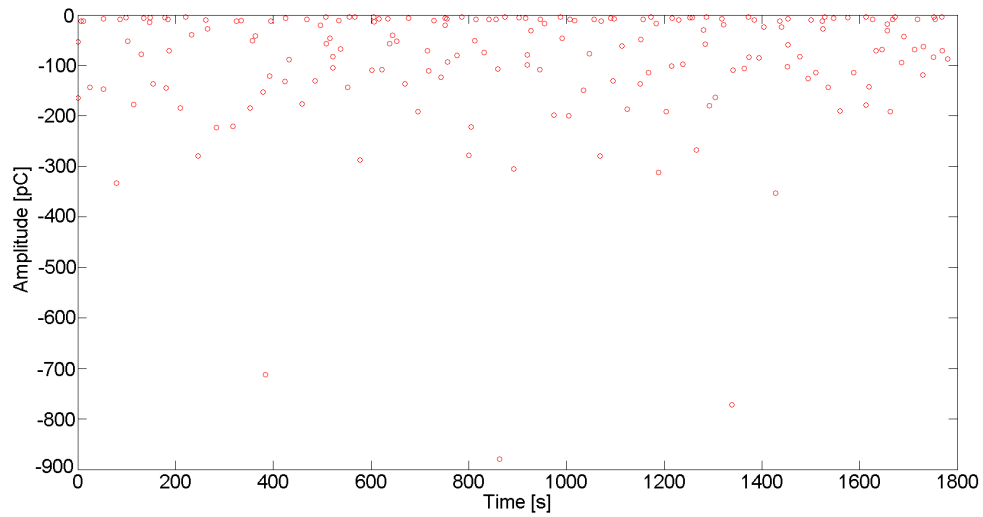


Figure 5.17: Time-resolved pattern of discharges in a spherical cavity sample at 30kV.

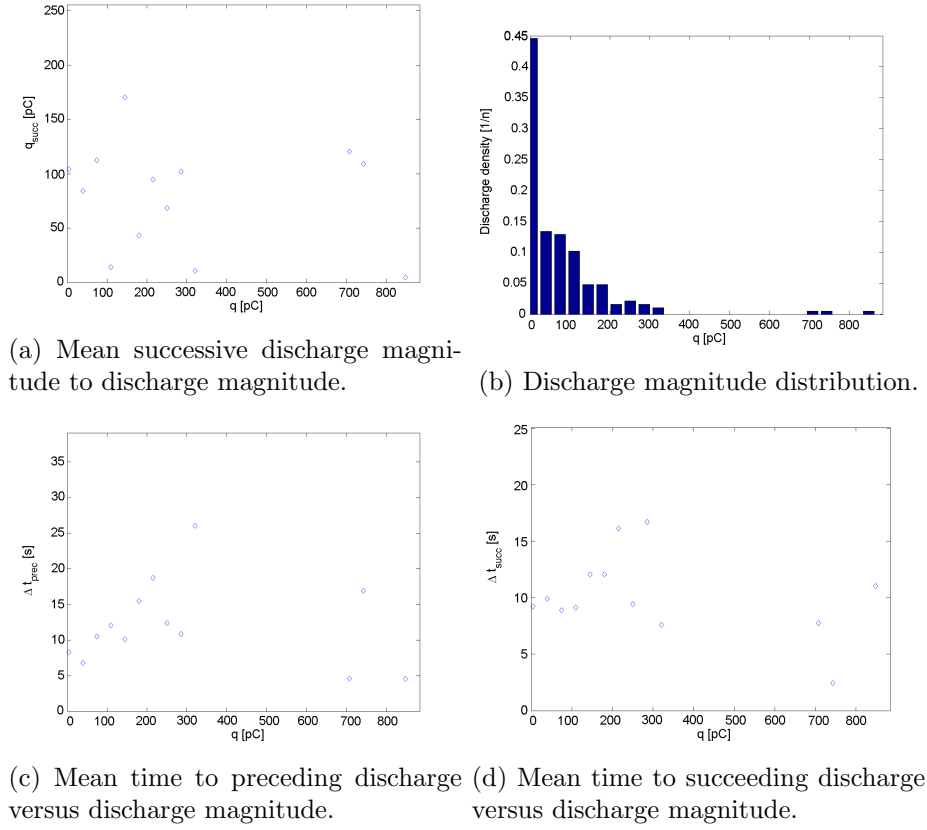


Figure 5.18: DC recognition plots for discharges in a spherical cavity sample at 30kV.

5.2.3 Discussion

The inception voltage of the internal discharges under DC voltage of 17 kV is slightly higher than that of AC with an inception voltage of 14 kV (peak). In theory it is quite possible that discharges in DC also take place at voltages as low as the AC inception voltage because the initial free electrons from both is due to either cosmic or background radiation. However, in DC the recovery time t_r between the discharges near infinity as calculated by equation (2.45). Charge decay also has a greater effect on the accumulated charge in DC than in AC resulting in a lowered electric field that results in higher inception voltages necessary for discharges to occur.

The magnitude of the discharges in AC are very high in comparison to the discharges in DC. The discharge magnitudes in AC being many times larger than discharges in DC at even twice the peak value. This phenomenon is explained considering the role of space charge generated by the electron avalanche reducing the field in the ionization volume and the discharge magnitude in DC. As the charge slowly builds up, the time lag t_L to discharge results in only a small excessive field ΔE . The polarity reversal of AC results in an enhancement of the ionisation coefficient by metastable species generated by previous discharges.

Looking at the DC recognition graphs of both DC polarities there is no correlation between the magnitude of the discharge q and that of the successive discharge \bar{q}_{succ} . The relatively long time lags make t_l the most contributing factor to the PD magnitude [19]. This is visible in the $\Delta t_{prec} - q$ relation for the internal discharges in positive DC voltage as shown in fig. 5.18c. Up to 400 pC there is a positive correlation. For the discharges above 600 pC this relation no longer holds. This is due to a different discharge mechanism taking over. Time resolved measurements have shown that both Townsend en Streamer

discharge take place. The Streamer discharges have a higher discharge magnitude and are recognized as the discharges measured above 600 pC. The PDs due to the Streamer mechanism have very narrow discharge channels and unlike the Townsend discharges do not result in the complete discharging of the void. The characteristic discharge parameters mean time lag \bar{t}_l and the mean recovery time \bar{t}_r retrieved from the DC voltage model for cavities become invalid as the model is not valid for streamer discharges.

The relation $\overline{\Delta t_{succ}} - q$ shows the same positive correlation for the internal discharges in positive DC voltage as shown in fig. 5.18d. The supposed streamer discharges exceeding the 400 pC do not lead to higher times to the next discharge. For Townsend discharges the higher discharge magnitudes result in bigger recovery times before a discharge is again possible. The Streamer mechanism leads to part of the cavity to discharge and as a result a successive discharge can ignite within a short time at another part of the surface what is known as multiple site discharging.

The PD inter-times recognition graphs for the internal discharges in DC negative voltage have no clear information within them. The difference between measurements in the polarities could possibly be due to a change in the condition of the cavity surface used as the cathode. Conduction over the surface is affected and with that the charge decay and charge accumulation. The recognition graphs do not take into account these complex phenomena making aged cavities difficult to recognize based on these plots.

5.3 Surface Discharges

Surface discharges are achieved over the surface of a cylindrical polymer type rod wedged between the inner and outer conductor of the GIS as seen in fig. 5.19a.

To avoid discharges other than surface discharges, good electrical conduction is necessary between the conductors and spacer. Electrical connection to the inner conductor is created by metallic tape connected via the top of the spacer extended to the surface on the side of the spacer. The effective distance between the conductors over the spacer is 85 mm.

The effect of a conductive particle on the surface of the spacer is also investigated. An aluminium particle tied to the middle of the spacer by fishing line as shown in fig. 5.19b is used to simulate the case of a free moving particle that has attached itself to the spacer.

The insulating gas used during the measurements of surface discharges over the spacer were humid air at 1 bar and a more realistic gas formulation of 1.1 bar SF_6 .

5.3.1 AC Voltage

The inception levels for surface discharges measured in AC for different gas formulations are shown in table 5.7. The electro-negative SF_6 increases the breakdown strength resulting in higher voltages necessary to achieve discharges.

	1.0 bar air [kV]	1.1 bar SF_6 [kV]
Inception V_{rms} [kV]	25	40

Table 5.7: Comparison of the inception voltage for surface discharges over cylindrical spacer using different gas formulations.

The trends of the discharge magnitude and the repetition rate for both air and SF_6 show an interesting course. There is an upward trend for both the charge magnitude and the repetition rate of the PDs per cycle for increasing voltages with air as insulating gas as shown in fig. 5.20a. The increased magnitude of the discharges at a higher voltage is a

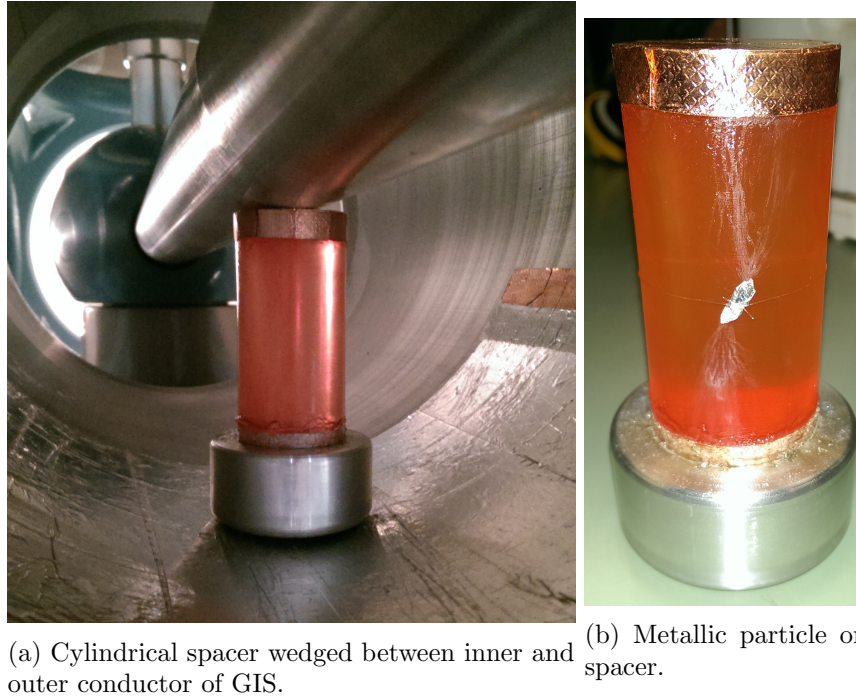


Figure 5.19: The cylindrical spacer and components used for simulating surface discharges.

result of the increased electric field extending the discharge region. Longer paths over the surface of the spacer are bridged by the PD.

The PD also deposits charge that can result in more free electrons for discharges over the same surface. The repetition rate increases as the inception field recovers faster and more times within a cycle with increasing applied voltage.

A decreasing trend is seen in fig. 5.20b for the discharge magnitude of the surface discharges taking place in SF_6 . However, the repetition rate of the PDs is increasing for increasing voltages. The electronegative gas increases the inception voltage as the breakdown strength enhances. At the same time the charge magnitude of the discharges decreases with applied voltage in comparison to the PDs in *air*. The electronegative gas recombines with the accumulated space charge resulting in negative ions reducing the local electric field and with it the propagation of the discharges over the surface. The shorter paths result in lower magnitude of the discharges. The reduced charge magnitude trend in SF_6 with increasing voltage could be as a result of the increase in discharges per cycle. The increased surface charge deposited will result in more electron attachment of SF_6 molecules shielding the regions of high electric field.

The PRPD patterns of the surface discharges at multiple voltage levels in *air* are shown in table 5.8. When the electric field at the surface of the electrode exceeds the breakdown strength of gas, ionisation of air near the surface of the electrode occurs. With increased applied voltage, the number of electron ionizations increases and the avalanche can grow longer along the spacer surface. The positive applied voltage sees a faster increase in the discharge magnitude. The PDs originate from the outer conductor which is extended by an extruded metal connection as visible in fig. 5.19a and fig. 5.19b. This interface affects the discharges as a *triple point*.

A triple point results in more electrons readily available from which avalanches develop. The electric field builds up along the path of the electron avalanche increasing the range of the surface discharges. The discharges at negative voltage extinguish along a shorter path over the surface resulting in smaller charge magnitudes. The build-up of surface charge can take place after a shorter time period increasing the repetition rate.

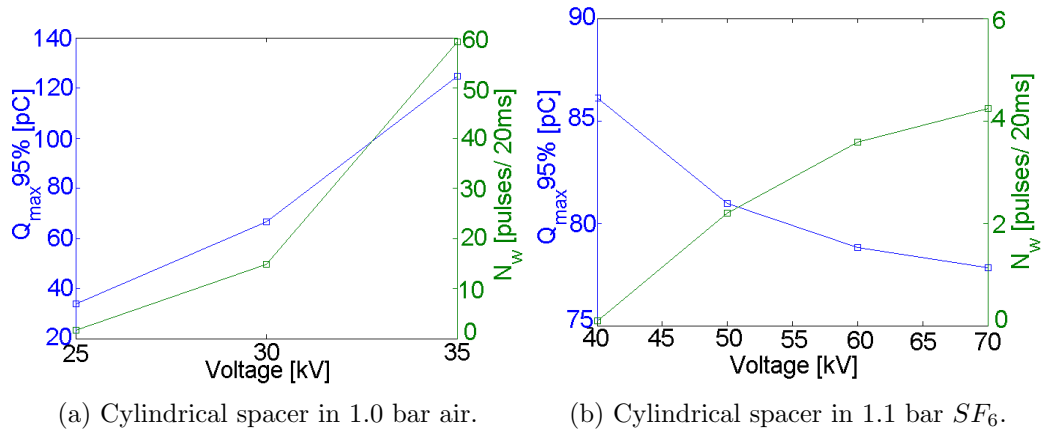


Figure 5.20: Trends of the 95% discharge magnitude and 50 Hz repetition rate at different AC voltage levels.

Table 5.8: Phase-resolved partial discharge patterns for surface discharges over cylindrical spacer in 1 bar air.

Discharge data			PRPD pattern	
	Pos cycle	Neg cycle	Partial Discharge Pattern 	
Q_{max} [pC]	28	53		
Q_{mean} [pC]	17	19		
Q_{min} [pC]	5	4		
Repetition rate [N/s]	39.319	45.433		
V_{rms} [kV]	25			
	Pos cycle	Neg cycle	Partial Discharge Pattern 	
Q_{max} [pC]	75	343		
Q_{mean} [pC]	16	44		
Q_{min} [pC]	5	2		
Repetition rate [N/s]	522.821	213.756		
V_{rms} [kV]	30			

Continued on next page

Table 5.8 – Continued from previous page

Discharge data

PRPD pattern

	Pos cycle	Neg cycle
Q_{max} [pC]	203	757
Q_{mean} [pC]	24	83
Q_{min} [pC]	7	1
Repetition rate [N/s]	2028.115	621.853
V_{rms} [kV]	35	

Partial Discharge Pattern

The PRPD plot shows the relationship between the amplitude of partial discharge (pC) and the phase angle (Deg). The x-axis represents the phase from 0 to 360 degrees, and the y-axis represents the amplitude from -1,00E+3 to 1,00E+3 pC. The plot shows a sinusoidal wave with a peak amplitude of approximately 1,00E+3 pC and a trough of -1,00E+3 pC. The data points are clustered around the zero line, indicating a symmetrical pattern.

In SF_6 as seen in table 5.9, the PRPD patterns of surface discharges at positive and negative voltage cycles become very symmetrical with only small variances in the charge magnitude and the repetition rate.

 Table 5.9: Phase-resolved partial discharge patterns for surface discharges over cylindrical spacer in 1.1 bar SF_6 .

Discharge data

PRPD pattern

	Pos cycle	Neg cycle
Q_{max} [pC]	92	84
Q_{mean} [pC]	74	66
Q_{min} [pC]	42	22
Repetition rate [N/s]	2.145	2.325
V_{rms} [kV]	40	

Partial Discharge Pattern

Amplitude [pC]

Phase [Deg]

Continued on next page

Table 5.9 – *Continued from previous page*

Discharge data			PRPD pattern
	Pos cycle	Neg cycle	
Q_{max} [pC]	87	84	
Q_{mean} [pC]	60	65	
Q_{min} [pC]	39	39	
Repetition rate [N/s]	57.990	51.852	
V_{rms} [kV]	50		

	Pos cycle	Neg cycle	
Q_{max} [pC]	92	87	
Q_{mean} [pC]	51	56	
Q_{min} [pC]	32	29	
Repetition rate [N/s]	95.512	82.095	
V_{rms} [kV]	60		

	Pos cycle	Neg cycle	
Q_{max} [pC]	92	74	
Q_{mean} [pC]	64	53	
Q_{min} [pC]	32	29	
Repetition rate [N/s]	98.129	108.614	
V_{rms} [kV]	70		

Partial Discharge Pattern

Partial Discharge Pattern

Partial Discharge Pattern

5.3.2 DC Voltage

No surface discharges are measured over the spacer within the voltage range of the DC source with the GIS filled with SF_6 gas. The following results are all from measurements done in *air* at atmospheric pressure.

Negative DC voltage

The inception of surface discharges with the application of negative DC voltage starts at -53.7 kV. The discharges start with a relatively high repetition rate which increases with the voltage. This is visible in the upward trend for the repetition rates seen in table 5.10. There is also an upward trend for the charge magnitude with increasing voltage. This trend keeps on till the applied voltage reaches -67 kV. The DC power supply is not able to deliver the necessary power and the voltage lowers to -62 kV.

Voltage [kV]	Q_{min} [pC]	Q_{max} [pC]	$Q_{max95\%}$ [pC]	Repetition rate [N/s]
-53	9	46	30	194.379
-63	8	61	54	282.952
-67	8	112	47	4104.238

Table 5.10: Discharge magnitudes and repetition rate surface discharges over cylindrical spacer at increasing negative DC voltage levels. Detection by means of quadrupole calibrated according to *IEC 60270*.

Decreasing the voltage from this state results in a downward trend for both the discharge magnitude and the repetition rate as seen from the data table 5.11. The trend lines displayed in fig. 5.21 show linear relation with the applied voltage. The same relationship holds for increasing voltage.

Voltage [kV]	Q_{min} [pC]	Q_{max} [pC]	$Q_{max95\%}$ [pC]	Repetition rate [N/s]
-67	7	185	124	11867.361
-60	18	149	61	3350.125
-57	20	78	42	223.101
-54	15	143	37	80.123
-50	9	35	32	0.749

Table 5.11: Discharge magnitudes and repetition rate surface discharges over cylindrical spacer at decreasing negative DC voltage levels. Detection by means of quadrupole calibrated according to *IEC 60270*.

A difference is spotted in the magnitude and the repetition rate of the PDs occurring at similar voltage levels but approached by either increasing or decreasing the voltage level. This is of interest as it shows that the surface changes temporarily due to previous discharges. The net effect for this spacer result in higher repetition rates and longer paths for the discharges resulting in higher discharge magnitudes. The change in surface condition also results in a lower *extinction voltage* as the surface discharges extinguish at 50 kV.

A time resolved PD pattern of the surface discharges before reaching the flash-over voltage is shown in fig. 5.22. The surface discharges display an erratic pattern that changes in time.

A discharge level in between 30 and 60 pC is visible in which most of the surface discharges take place. This is seen in the discharge magnitude distribution in fig. 5.23b. This differs from the surface discharges seen after flash-over at a voltage level of 60 kV of which the time resolved pattern is shown in fig. 5.24. The magnitude distribution shown in fig. 5.25b reveals a concentration of the discharges around the same level as was seen for the surface discharges before flash-over but also higher magnitude PDs occurring at a lesser frequency.

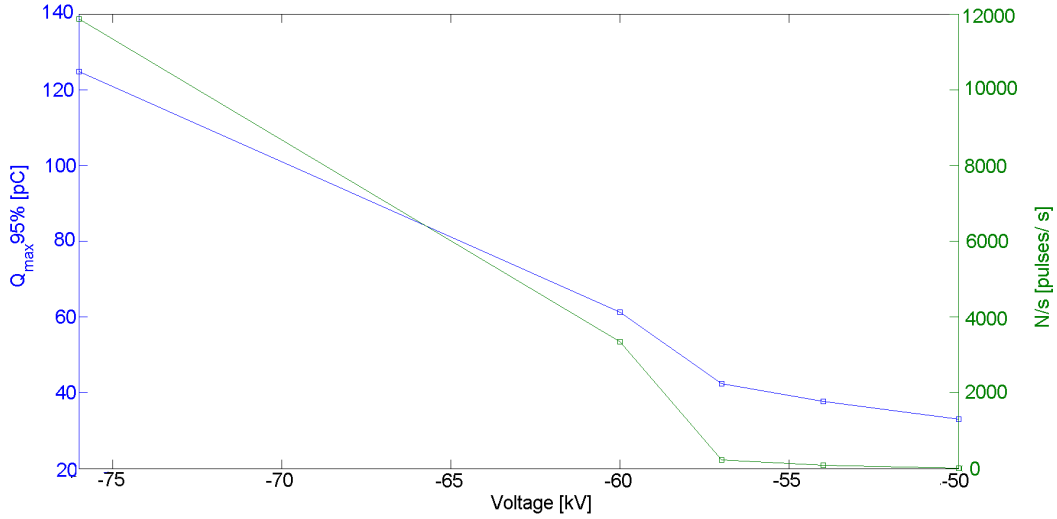


Figure 5.21: Trend lines of the 95% discharge magnitude and repetition rate at decreasing negative DC voltage levels for surface discharges over a cylindrical spacer.

The differences between the two cases of surface discharges based on the rest of the recognition graphs is very small. A positive correlation is seen for both in the discharge magnitude and the mean successive discharge magnitude as shown in fig. 5.23a and fig. 5.25a.

Longer discharges result in successive PDs of higher magnitude. The large discharges result in more charge deposited on the surface extended over a wider area. These charges could result in a field opposing the applied one, but also in electrons that are more easily freed to extend the discharge path.

The DC-recognition graphs based on the inter-times for both before and after flash-over shows the effect of discharge trains. An overlap of these graphs to the magnitude distribution shows higher times to preceding and successive discharges for the discharge levels of the PDs in between 30 and 55 pC pre flash-over in fig. 5.23c and fig. 5.23d and post flash-over in between 20 and 40 pC in fig. 5.25c and fig. 5.25d.

This can be interpreted as the discharges occurring normally at a certain stable discharge level. The time between these discharges is relatively high. Then discharge trains occur with a large variations in discharge magnitude. The times between these PDs is very small.

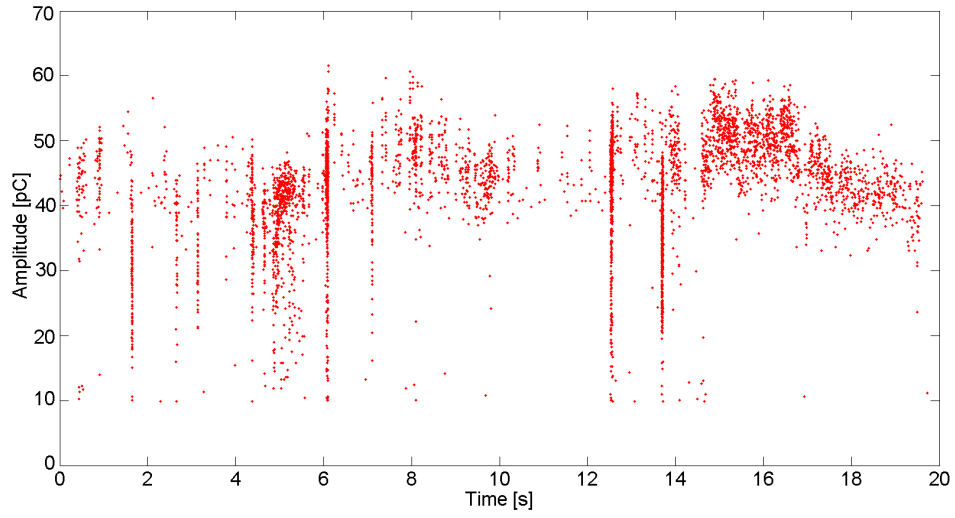
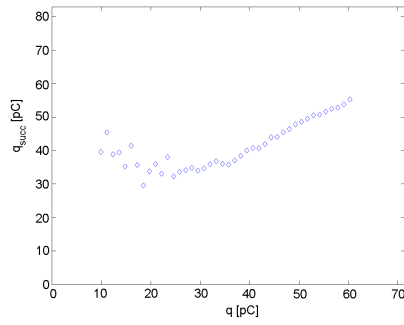
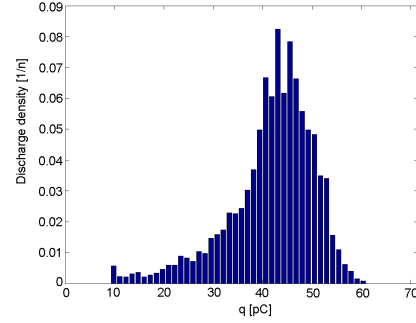


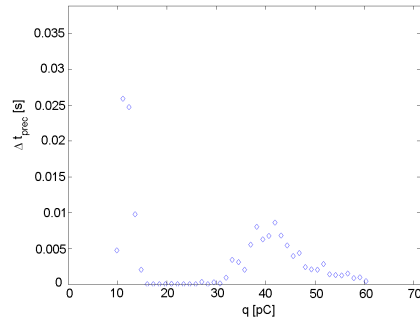
Figure 5.22: Time-resolved pattern of surface discharge before flash-over at 63kV.



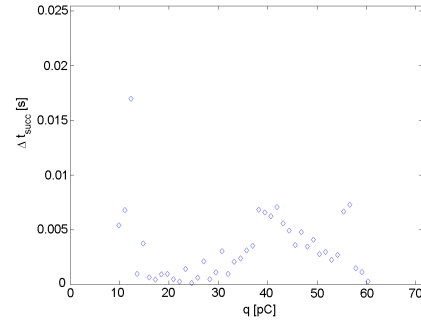
(a) Mean successive discharge magnitude to discharge magnitude.



(b) Discharge magnitude distribution.



(c) Mean time to preceding discharge versus discharge magnitude.



(d) Mean time to succeeding discharge versus discharge magnitude.

Figure 5.23: DC recognition plots for surface discharges before flash-over at 63kV.

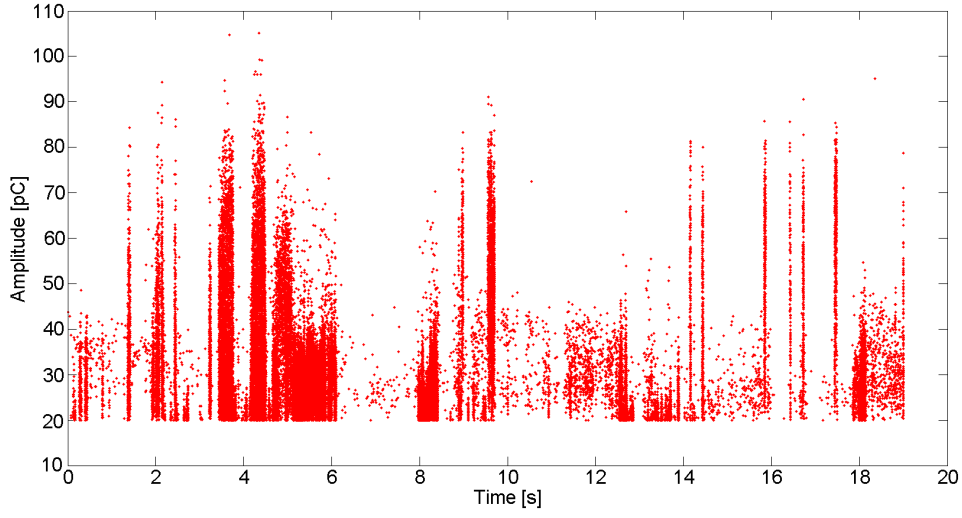


Figure 5.24: Time-resolved pattern of surface discharge after flash-over at 60kV.

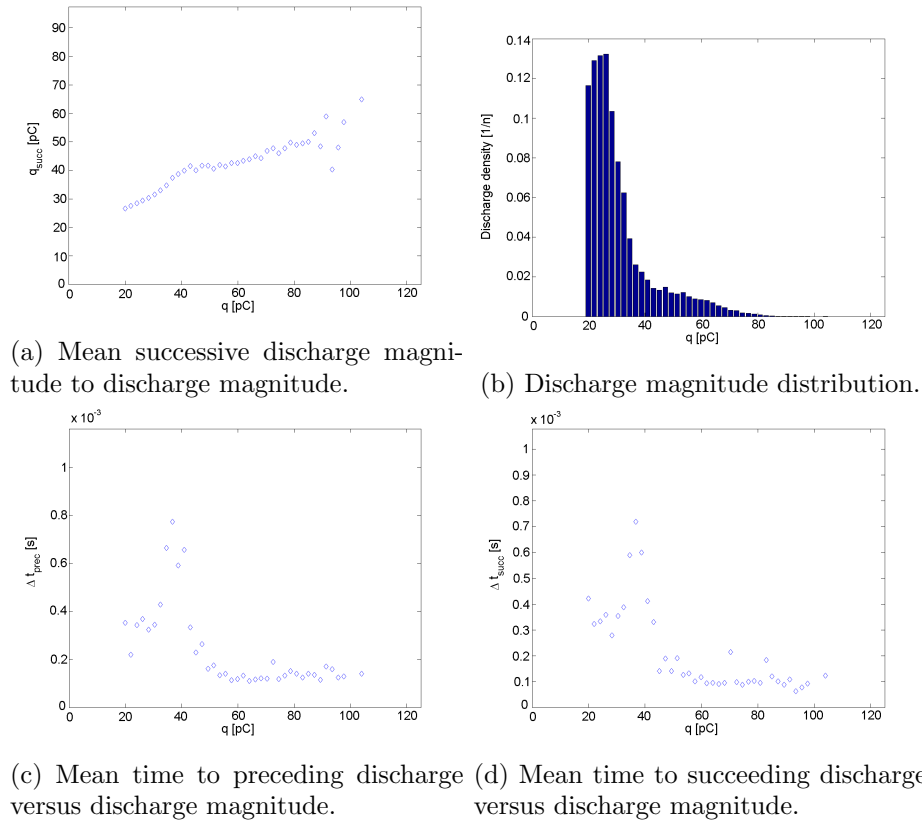


Figure 5.25: DC recognition plots for surface discharges after flash-over at 60kV.

Positive DC voltage

The inception voltage of the surface PD for positive applied DC voltage starts at 53 kV. Increasing the voltage increases the charge magnitude and the repetition rate as can be seen in table 5.12. Compared to the discharges seen at negative applied voltage, the repetition rate is low, but the charge magnitude is very high. This is as a result of the PD originating from the *triple point*. An abundance of free electrons result in longer discharge paths resulting in bigger discharges and longer recovery times for the next discharge.

Voltage [kV]	Q_{min} [pC]	Q_{max} [pC]	$Q_{max95\%}$ [pC]	Repetition rate [N/s]
53	9	223	110	0.544
58	117	1483	1365	1.621
63	27	2953	2105	6.176

Table 5.12: Discharge magnitudes and repetition rate surface discharges over cylindrical spacer at increasing positive DC voltage levels. Detection by means of quadrupole calibrated according to *IEC 60270*.

The voltage was increased up to 63 kV showing a linear increase for both the charge magnitude and the repetition rate. After a period of time a flash-over occurred at this voltage level.

The DC power supply is not able to deliver the necessary power and reduces to a stable output of 60 kV. Reducing the voltage from this state has led to trends as seen in table 5.13.

Voltage [kV]	Q_{min} [pC]	Q_{max} [pC]	$Q_{max95\%}$ [pC]	Repetition rate [N/s]
63	11	3867	820	916.704
60	11	2354	1506	172.801
57	23	1836	871	1649.772

Table 5.13: Discharge magnitudes and repetition rate surface discharges over cylindrical spacer at decreasing positive DC voltage levels. Detection by means of quadrupole calibrated according to *IEC 60270*.

The surface PD extinguishes at 55 kV, a voltage level higher than its inception voltage. This is opposite of what was measured for the PDs resulting from negative DC. The discharges due to the triple point at this voltage level are numerous with high magnitudes resulting in deposited charge on the surface that reduce the electric field. The condition for PD locally ceases to exist and the PDs extinguish.

The time-resolved PD pattern of the surface discharges at 57 kV after flash-over has taken place is shown in fig. 5.26. It displays a very erratic pattern for the discharges changing continuously in time. The majority of the PDs have a discharge magnitude between 300 and 600 pC. Throughout the time-resolved pattern a continuous discharge level is seen between 800 and 1000 pC with discharge trains introducing discharges with magnitudes from 0 to 1600 pC.

Focusing on such a discharge train in fig. 5.27 reveals a high concentration of discharges between 300 and 600 pC accompanied with discharges above 1100 pC.

The recognition graph of the discharge magnitude and the mean successive discharge shows a positive correlation between the discharges between the discharge magnitude of 300 - 1100 pC. The relation does not hold for discharges exceeding 1100 pC.

The DC-recognition graphs based on the inter-times reveal the discharge trains again.

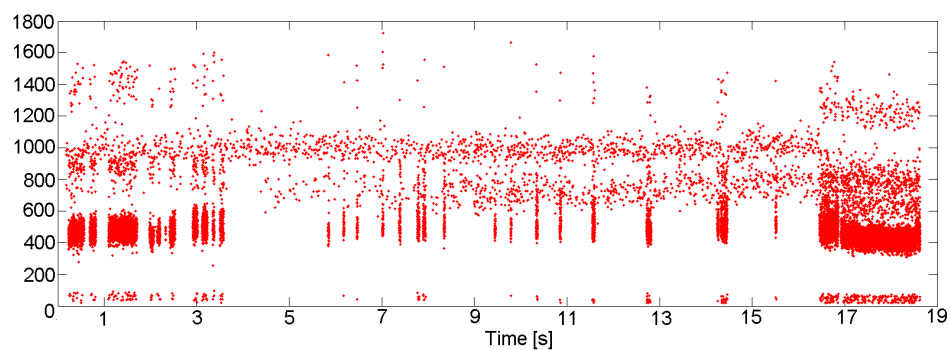


Figure 5.26: Time-resolved pattern of surface discharge after flash-over at 57kV.

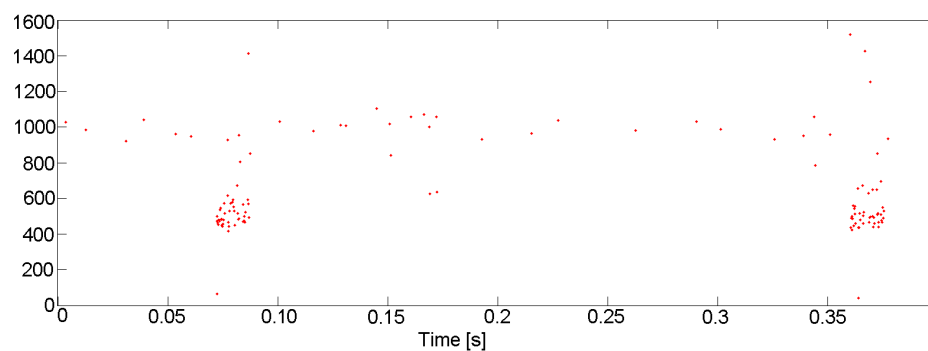


Figure 5.27: Time-resolved pattern of PD discharge train at 57kV.

The higher average times for both to the successive and previous discharge shows the discharges between 600 and 1100 pC occurring with a lower repetition rate than the discharges as a result of the discharge trains.

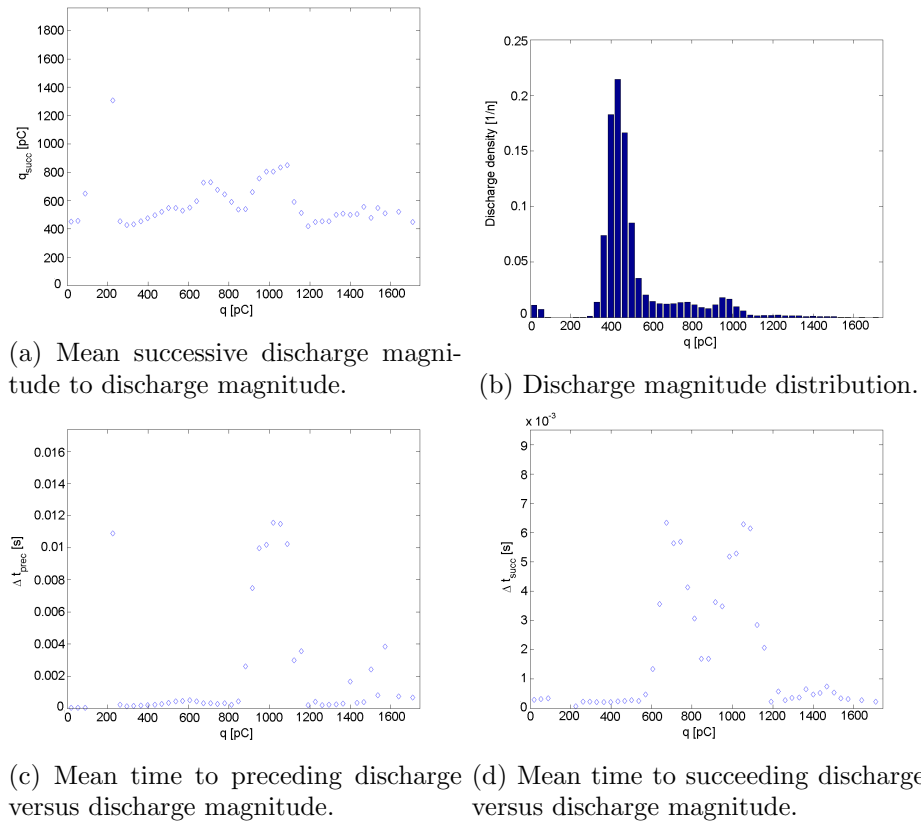


Figure 5.28: DC recognition plots for surface discharges after flash-over at 57kV.

5.3.3 Discussion

The voltage level for inception of surface discharges is many times lower for AC 35 kV (peak) than for DC with 53 kV. The polarity reversal of the voltage releases starting electrons far easier from the interface or triple point than the constant electric field.

For discharges in AC and DC it was seen that the discharge repetition rate and the PD magnitude are positively correlated with the test voltage. A higher voltage increases the electric field. The discharge area expands as the electric field increases and a larger number of possible discharge paths become available increasing the repetition rate. The higher electric field also increase the discharge path and the discharged volume increasing the PD magnitude.

In both AC and DC, the effect of the triple point greatly affects the PDs. An increase in magnitude is visible for both as more electrons are injected. In DC this injection leads to very big discharges covering longer distances before extinguishing. As a result the breakdown of the total spacer occurs at lower voltages.

The surface discharge is very dependent on the local electric field. The electric field is refracted due to locally dependent factors that range from the surface roughness, conductivity variances etc. Charge deposited by previous PDs also affect the local electric field leading to field distortions along the discharge path. These charges could lead to shielding of the defect source, but deposited electrons could also result in increasing the discharge paths when freed as starting electrons. With SF_6 as gas medium these deposited charges will become negative ions and the shielding effects will increase. Discharge paths vary depending on the distortions encountered. The length of the discharges vary and with it the discharge magnitude.

The PD magnitude and the repetition rate of surface discharges are changing over time. This is presumably due to the charging effect of the surface. The interface becomes progressively charged with time and the electric field at this location decreases. This was seen in the extinction of the discharges at voltages where the PD activity slowly ceases.

There is a memory effect between the successive surface discharges as seen in the relation of the magnitude of the discharge q and that of the successive discharge \bar{q}_{succ} . The deposited electrons on the surface are not deeply trapped and are freed leading to more starting electrons for the surface PD. In SF_6 these deposited electrons will have the reverse effect as they recombine in negative ions reducing the electric field. The same is also the case for too much electrons deposited as was seen for DC positive.

The recognition graphs of the discharges based on the inter-times have shown little correlation between the times between the discharges and the charge magnitude. The charge magnitude is too dependent on the path of the discharge. This path is determined by local surface parameters resulting in multiple discharge paths when possible. The discharges thus become independent of one another.

The surface condition was also influenced by attaching a conductive particle to the surface of the spacer. In DC this particle resulted in an increased breakdown strength for both polarities. The inception voltage of the surface discharges increased to 70 kV and the voltage where flash-over occurs increased to 80 kV. This increase in breakdown strength was also noticed in [33] and is possibly due to surface charging of the spacer near the tips of the particle influencing the flash-over mechanism. Prior to flash-over no corona discharges are measured as the surface charging results in a decreased local electric field. Surface discharges occurred in a similar fashion as was measured for smooth spacers and once the obstacle of surface charging is overcome, the PD propagate over paths through the metallic particle can be seen in by the paths over the surface in fig. 5.19b. The path through the metallic particle has the lowest breakdown strength as the particle is charged with each discharge increasing the local field to the opposite conductor.

Chapter 6

Experimental Results II: RF PD calibration in GIS

6.1 Introduction

In chapter 5 of this thesis the recognition of PD defects stressed by DC has been studied.

The charge magnitude of the discharge is an important parameter as it relates to the transfer and the distribution of charges on and around the defect source. The condition for the occurrence of PD is affected and a pattern emerges.

The IEC 60270 detection method used in the previous chapter had the advantage of calibrated measurements resulting in a measurement of the apparent charge directly related to the discharge magnitude. The major drawback of this method is in the use for on-line monitoring. The configuration necessary results in taking the GIS out of service. Furthermore, only the slowly damped response to fast PD activity [53] is measured which results in a loss of the information on the discharge mechanism. The UHF technique described in section 3.2.2 uses a coupling sensor to measure the EM waves induced by PD current pulses. The measurement is a non-contact technique and has high sensitivity for discharges propagating inside the GIS tank making it an ideal alternative for on-line monitoring of PD inside the GIS.

The waveforms of the PD can not be calibrated in a similar fashion as the IEC method but previous studies have shown a possible relationship between the two measuring principles and results of [54] indicate that there might be a relationship between RF energy and apparent charge with a dependence on the nature of the defect and its mechanism.

The measured RF energy is not only dependent on factors related to the PD behaviour itself but also on the frequency response of the RF detection equipment that is used. The references [55, 56] specify that the measured RF energy is dependent on the characteristics of the detecting RF sensor, but also dependent on the resonances within the GIS due to propagation effect of reflection, dispersion and attenuation.

The output level of the RF PD measuring system is determined by several factors such as:

1. The type of PD (i.e. the electric stress caused by the defect's type and geometry)
2. The frequency response of the RF sensor
3. The effect of the HV equipment structure in terms of:
 - the loss of information about the discharge process itself with increasing distance between sensor and PD origin,
 - the increasing impact of pulse propagation path on PD waveform,

- the superposition between different signals, e.g. multiple PD sources, crosstalk, external interferences.

A graphic representation of these factors influencing the measured output is shown in fig. 6.1.

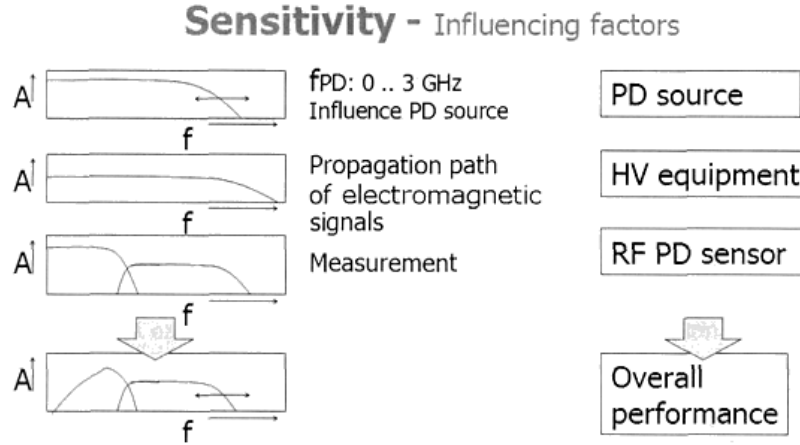


Figure 6.1: PD detection sensitivity affected by different factors [46].

Using this information an investigation into the relationship between RF signals picked up through RF detection and the apparent charge quantity of different types of PD defects with the intention of calibrated RF measurements is done in this chapter.

6.2 PD Measurement

6.2.1 Acquisition of data

The measurement of PD is achieved through the IEC 60270 and the UHF technique for DC voltages. The UHF antenna, HFCT and Quadrupole sensors simultaneously measure the PD and the waveforms of the same PD event are captured using the Tektronix DPO7354C digital oscilloscope.

The HFCT sensor has shown a high Signal-to-Noise Ratio (SNR) and this waveform is used to trigger the capture of the PD waveforms. Using digital wideband filtering according to IEC 60270 specifications of the Quadrupole signals resulted in peak values from which the apparent charge quantity is calculated. The UHF waveforms are processed further in the time and frequency domain for characteristic parameters to compare to the apparent charge quantity. The pulse spectrum is determined through the FFT of the pulse waveform smoothed to show a frequency spectrum with a 1 MHz RBW.

For proper comparison between the RF signals and the apparent charge quantity the recorded waveforms of both the UHF antenna and the Quadrupole sensors must show no distortion. A selection of waveforms for further analysis is made through separation via the TF-map of the Quadrupole signals followed by the same procedure of the UHF waveforms. This selection resulted in an exclusion of the waveforms showing multiple discharges within the captured window, distortions, EMI and internal noise signals.

The measured waveforms originate from the PD sources used in the same set-up for the experiments of chapter 5. The insulating gas for all the measurements is *air* at atmospheric

pressure.

6.2.2 Tools for quantitative data analysis

The wave shape of the acquired RF PD signals can be differentiated into two types based on the discharge mechanism. The fast Streamer and the slower Townsend discharge waveforms as seen in fig. 6.2a are identified. The emitted RF radiation excites the GIS into resonance at frequencies of up to 1.2 GHz. The shape of the original PD pulses are heavily influenced by these resonances and other factors and the resulting pulse spectra as visible in fig. 6.2b show little resemblance to the simulations of section 3.2.3 except for the Streamer discharges with more energy content in the higher frequencies.

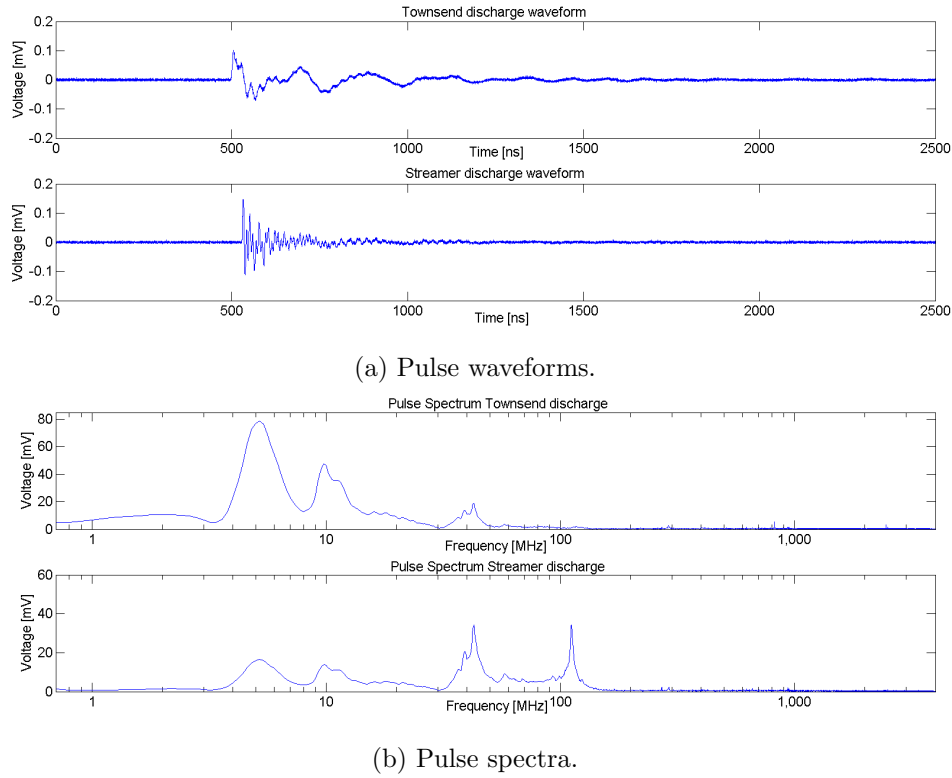


Figure 6.2: RF signals and spectra of Streamer and Townsend discharges in internal cavity.

Due to the complex resonant nature of RF PD pulses, the peak amplitude often used to correlate the RF signal to the apparent charge is an inadequate quantification of the signal strength in the GIS. A quantity taking into account all the points on the trace of the captured waveform is the RF energy and thus better suited. The RF energy is the discrete-time integral of the pulse waveform which is calculated according to eq. (6.1) with V_i the energy at sample point i , Δt the time between samples and R the load impedance of the measuring system.

$$E_{RF} = \frac{\Delta t}{R} \sum_i V_i^2 \quad (6.1)$$

The pulse spectra for the different discharge mechanisms shows a non-linear distribution over frequency band. The E_{RF} is the energy over the whole frequency range, but by filtering in frequency bands the effect of the complex resonances can either be excluded or included. The bandwidths decided upon for RF - apparent charge correlation are:

- 0.8 – 3 MHz

- 4 – 7 MHz
- 1 – 30 MHz
- 40 – 50 MHz
- 60 – 100 MHz
- 300 – 3000 MHz

For statistical verification of the reliability of the regression equations of the correlation graphs between the different parameters and the apparent charge quantity, regression analysis was applied to all data to determine the regression of the dataset quantitatively. A regression coefficient is calculated ranging between 0 and 1. The greater the value of this coefficient the better the correlation is between the supposed independent variables. The formula is as follows:

$$R^2 = \frac{SSR}{SST} = \frac{\sum_{i=1}^n (\hat{y}_i - \bar{y})^2}{\sum_{i=1}^n (y_i - \bar{y})^2} \quad (6.2)$$

with y_i the observed values, \bar{y} the mean value of y_i , \hat{y} the regression value, SSR the regression sum of squares and SST the total sum of squares indicating the total dispersion between all observed values and their mean values.

6.3 Results and discussion

6.3.1 Floating component discharges

The discharges of the floating components are identified as Streamer discharges for all captured waveforms. The high amplitude PDs have been measured without amplification. The flat response of the High Frequency (HF) amplifier should not result in distortion of the signals measured with the amplifier and can thus be readily compared to the signals measured without an amplifier.

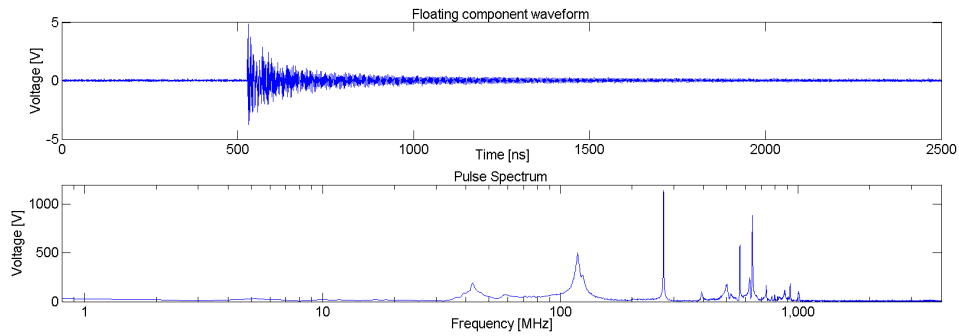


Figure 6.3: RF signal and frequency spectrum produced by a floating component discharge.

In this configuration not all discharges are picked up with the UHF antenna. The high magnitude discharges of the double layer discussed in section 5.1 are picked up with peak values in volt range. The lower magnitude discharges however are not visible in the same scale.

The discharges measured by the UHF antenna as seen in fig. 6.3 are plotted against the apparent charge of the discharge resulting in the relationship plots of fig. 6.4.

The linear regression of both the waveform and spectrum parameters to the apparent charge and the square of the apparent charge in the case of the energy are shown in

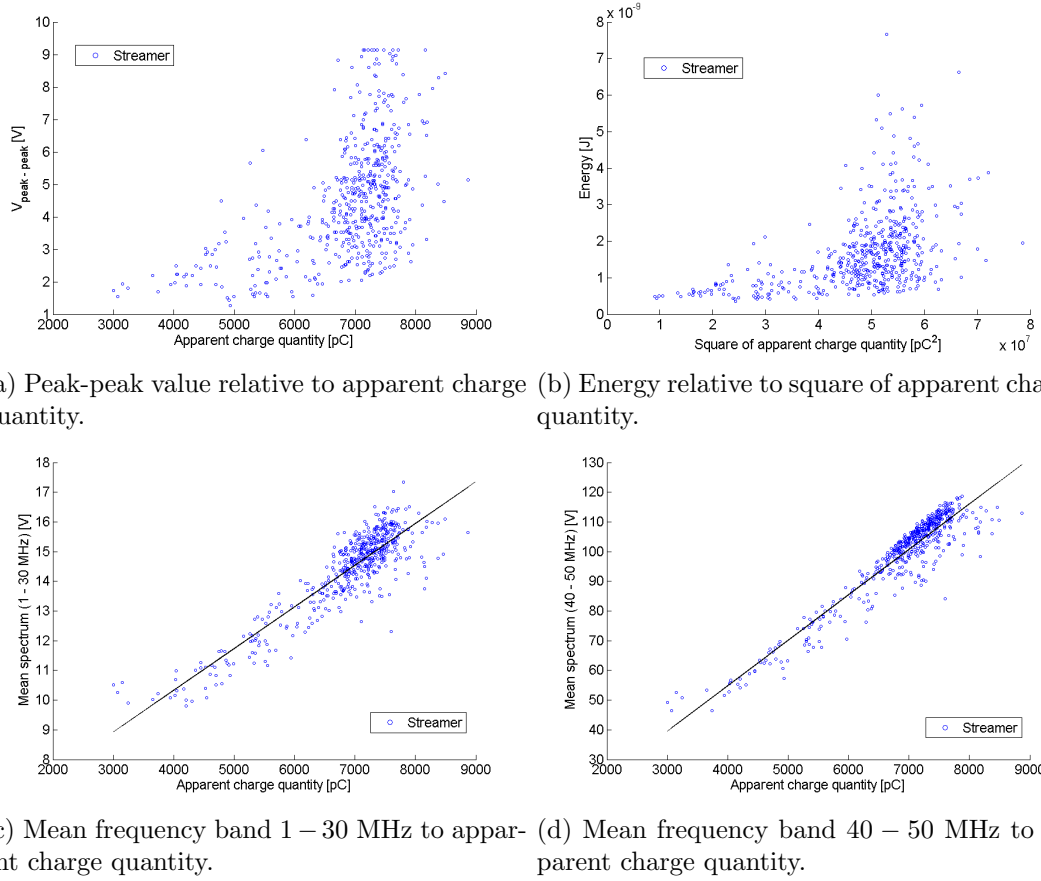


Figure 6.4: Relationship between RF signal floating component PD and apparent charge quantity.

table 6.1. Within the range of the discharge magnitude the waveform parameters show little relation to the apparent charge. This relation is found within certain frequency bands as these show much better regression. The parameters showing good regression to the apparent charge quantity are coloured in red as seen in table 6.1.

Frequency band (MHz)	Streamer	
	R	m [V/pC]
0.8 – 3	0.4524	0.0017
4 – 7	0.8036	0.0022
1 – 30	0.8960	0.0014
40 – 50	0.9441	0.0153
60 – 100	0.8510	0.0085
300 – 3000	0.3577	0.0012

Waveform parameter	Streamer	
	R	m
V_{peak}	0.5448	$4.3631e^{-4}$ [V/pC]
V_{pp}	0.5245	0.0010 [V _{pp} /pC]
Energy	0.4674	$4.3850e^{-17}$ [J/pC]

(a) Spectrum parameters.

(b) Waveform parameters.

Table 6.1: Value of regression coefficient R and slope m of regression line for floating component discharges.

6.3.2 Negative corona

The negative corona discharges comprised of PDs of the streamer type of which one is displayed in fig. 6.5. The discharges differed little from one another and this was also noticeable in the RF waveforms and frequency spectra. In comparison to the floating component discharges, the distribution of frequency content in the lower frequencies is much higher.

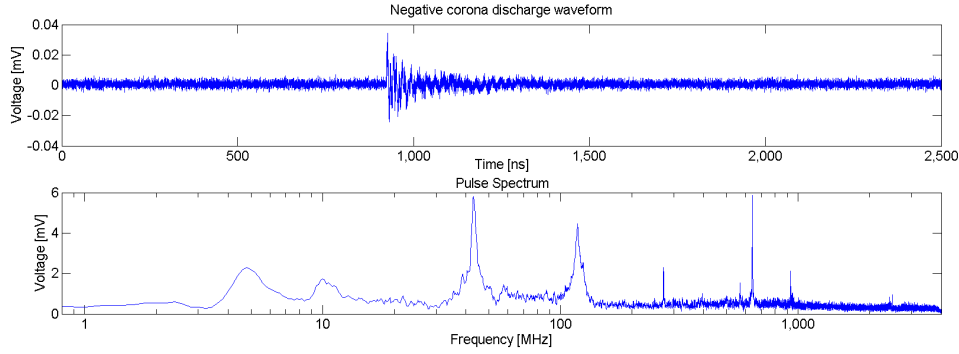
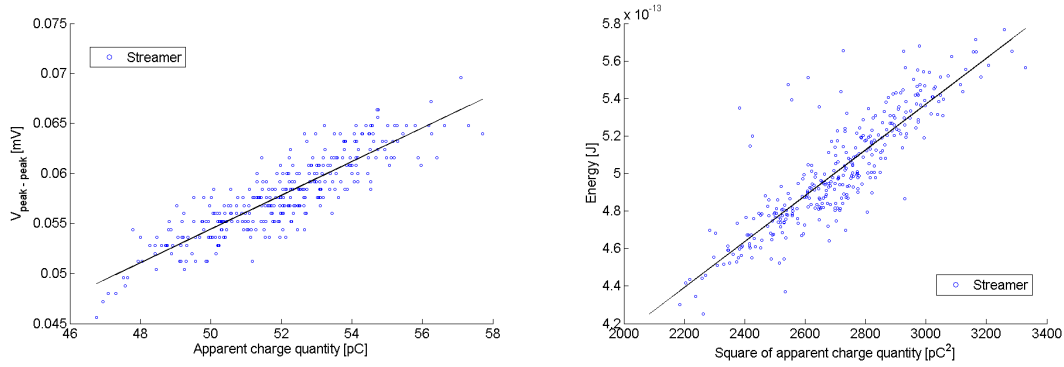
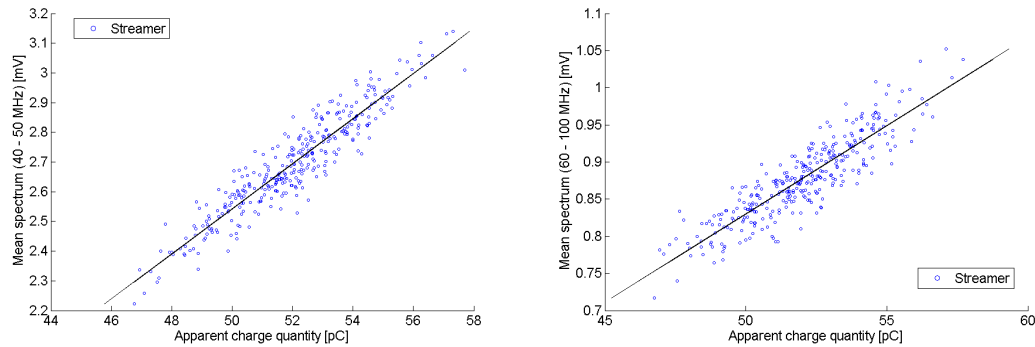


Figure 6.5: RF signal and frequency spectrum produced by negative corona.



(a) Peak-peak value relative to apparent charge quantity. (b) Energy relative to square of apparent charge quantity.



(c) Mean frequency band 40 – 50 MHz to apparent charge quantity. (d) Mean frequency band 60 – 100 MHz to apparent charge quantity.

Figure 6.6: Relationship between RF signal negative corona and apparent charge quantity.

The waveform parameters show a good relation to the apparent charge quantity within the discharge range. The same is seen in the spectrum parameters for the higher frequencies as can be seen in fig. 6.6 and in table 6.2.

Frequency band (MHz)	Streamer	
	R	m [mV/pC]
0.8 – 3	0.0163	$5.784e^{-4}$
4 – 7	0.7271	0.0446
1 – 30	0.8150	0.0167
40 – 50	0.9350	0.0759
60 – 100	0.8882	0.0238
300 – 3000	0.5677	0.0012

(a) Spectrum parameters.

Waveform parameter	Streamer	
	R	m
V_{peak}	0.8182	$9.8720e^{-4}$ [mV _p /pC]
V_{pp}	0.8738	0.0017 [mV _{pp} /pC]
Energy	0.8669	$1.2218e^{-16}$ [J/pC]

(b) Waveform parameters.

 Table 6.2: Value of regression coefficient R and slope m of regression line for negative corona discharges.

6.3.3 Positive corona

The positive corona discharge waveforms show a lot of variation in the wave-shape to one another and has little frequency content above 300 MHz.

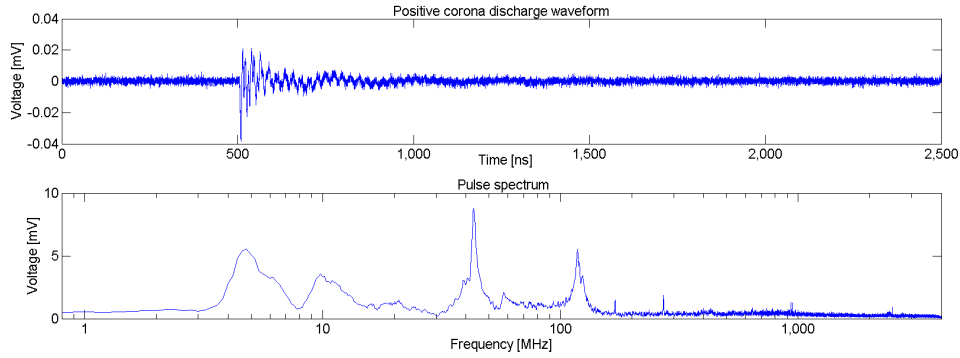
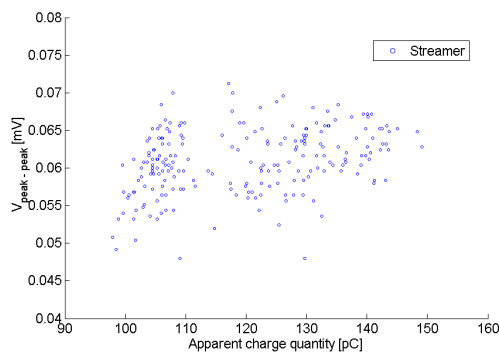
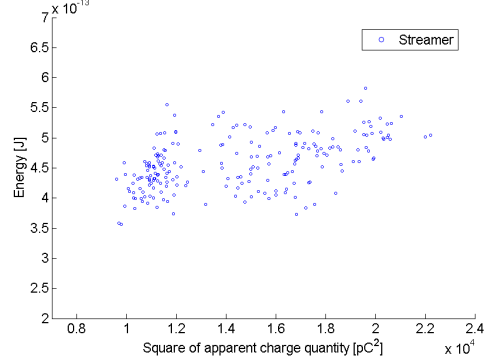


Figure 6.7: RF signal and frequency spectrum produced by positive corona.

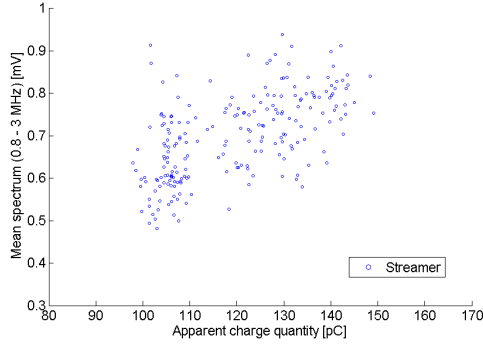
The relationship graphs of the waveform and spectrum parameters to the apparent charge quantity show little correlation. This difference between the negative and positive corona is possibly due to the starting point of the PD. The PDs in negative corona originate at the needle protrusion while these of the positive corona start in the high field region near and propagating towards the needle tip. The propagation path differs along with the angle of observation to the UHF antenna and with it the manner in which the PD is picked up.



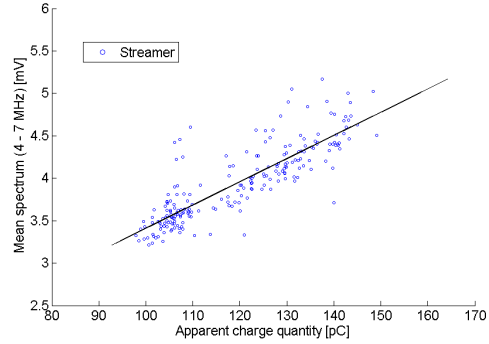
(a) Peak-peak value relative to apparent charge quantity.



(b) Energy relative to square of apparent charge quantity.



(c) Mean frequency band 0.8 – 3 MHz to apparent charge quantity.



(d) Mean frequency band 4–7 MHz to apparent charge quantity.

Figure 6.8: Relationship between RF signal positive corona PD and apparent charge quantity.

Frequency band (MHz)	Streamer	
	R	m [mV/pC]
0.8 – 3	0.5891	0.0042
4 – 7	0.8471	0.0273
1 – 30	0.4674	0.0070
40 – 50	0.4134	0.0098
60 – 100	0.0728	$4.3308e^{-4}$
300 – 3000	0.0623	$1.3066e^{-5}$

(a) Spectrum parameters.

Waveform parameter	Streamer	
	R	m
V_{peak}	0.3427	$6.6820e^{-5}$ [mV _p /pC]
V_{pp}	0.3306	$1.0200e^{-4}$ [mV _{pp} /pC]
Energy	0.4942	$6.4054e^{-18}$ [J/pC]

(b) Waveform parameters.

Table 6.3: Value of regression coefficient R and slope m of regression line for positive corona.

6.3.4 Internal discharges

Two types of PD take place in the cavity sample. These are the Streamer type discharges as shown in fig. 6.9 and the Townsend type discharges displayed in fig. 6.10.

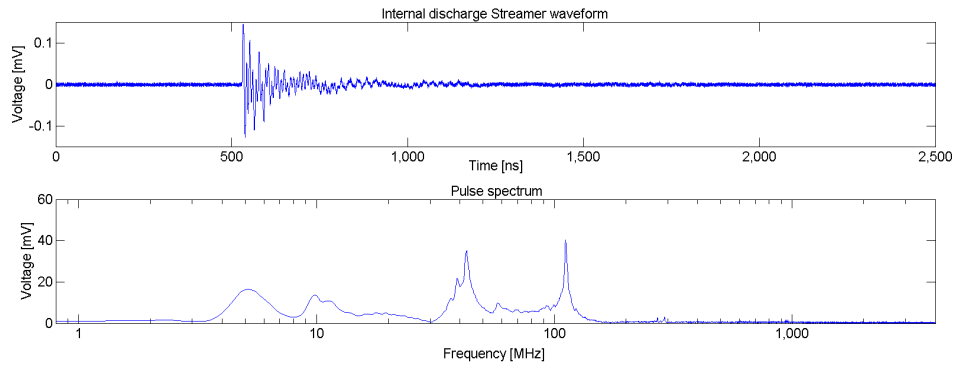


Figure 6.9: RF Streamer discharge signal and frequency spectrum produced by internal discharges.

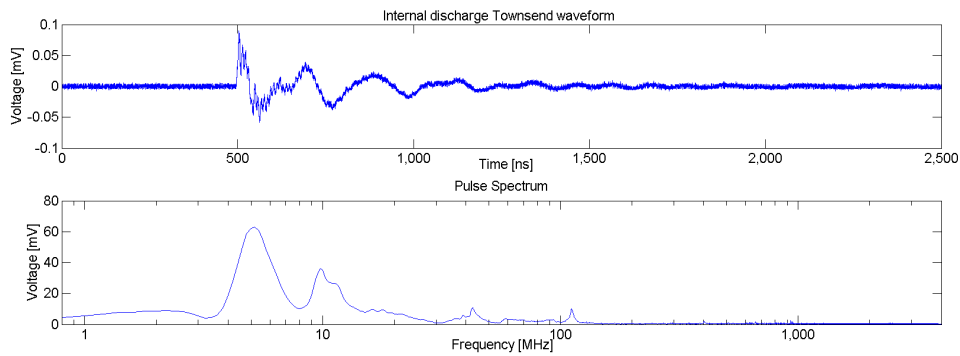


Figure 6.10: RF Townsend discharge signal and frequency spectrum produced by internal discharges.

The frequency distribution of the two types of discharges shows that the Townsend discharges have their frequency content distributed over much lower frequencies than the Streamer discharges.

Separate analysis of the types of discharges show that the relationship of the characteristic parameters to the apparent charge quantity is heavily dependent on the discharge mechanism as visible in the relationship plots of fig. 6.11.

The linear regression coefficient of both the waveform and spectrum parameters to the apparent charge shown in table 6.4 show that in the spectrum parameters the mean of the lower frequency regions for Townsend discharges show the highest regression while for the Streamer discharges the higher frequency regions yields better result.

The analysis plots also shows that the apparent discharge magnitudes of the Townsend discharges exceed that of the Streamer discharges.

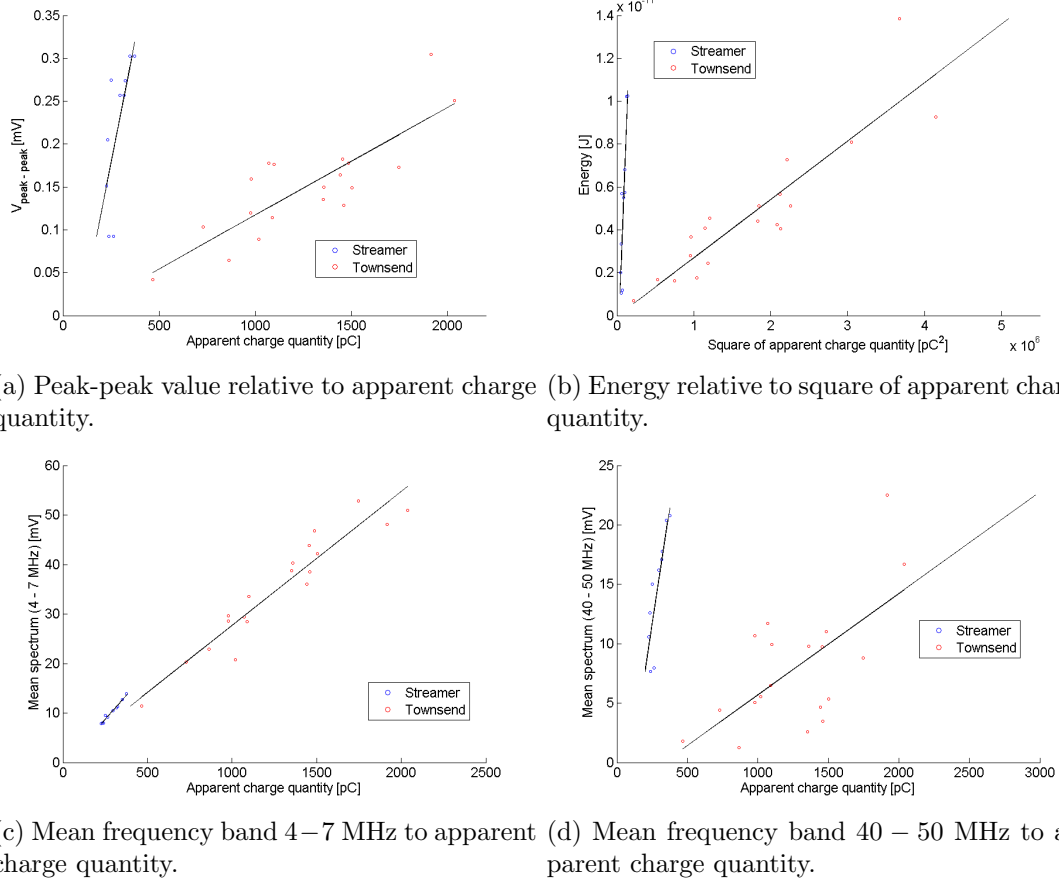


Figure 6.11: Relationship between RF signal internal discharges and apparent charge quantity.

Frequency band (MHz)	Townsend		Streamer	
	R	m [mV/pC]	R	m [mV/pC]
0.8 – 3	0.9622	0.0048	0.5103	0.0018
4 – 7	0.9505	0.0271	0.9874	0.0393
1 – 30	0.8807	0.0076	0.8559	0.0145
40 – 50	0.6429	0.0085	0.8642	0.0788
60 – 100	0.7371	0.0015	0.7528	0.0304
300 – 3000	0.6855	$3.3998e^{-5}$	0.7258	$1.4360e^{-4}$

(a) Spectrum parameters.

Waveform parameter	Townsend		Streamer	
	R	m	R	m
V_{peak}	0.8214	$6.3880e^{-5}$ [mV _p /pC]	0.7831	$6.9171e^{-4}$ [mV _p /pC]
V_{pp}	0.8291	$1.2533e^{-4}$ [mV _{pp} /pC]	0.7259	0.0011 [mV _{pp} /pC]
Energy	0.9037	$6.7242e^{-18}$ [J/pC]	0.8967	$9.6938e^{-17}$ [J/pC]

(b) Waveform parameters.

Table 6.4: Value of regression coefficient R and slope m of regression line for internal discharges.

6.3.5 Surface discharges

Similar to the discharges of positive corona, the wave-shapes of the surface discharges show a lot of variation. The surface discharges excite resonances in very high frequencies as seen in fig. 6.12. The frequency distribution of the surface discharges is very different from the previous discharges. The insertion of a spacer in GIS does change the inner structure and as a result the changes in resonances.

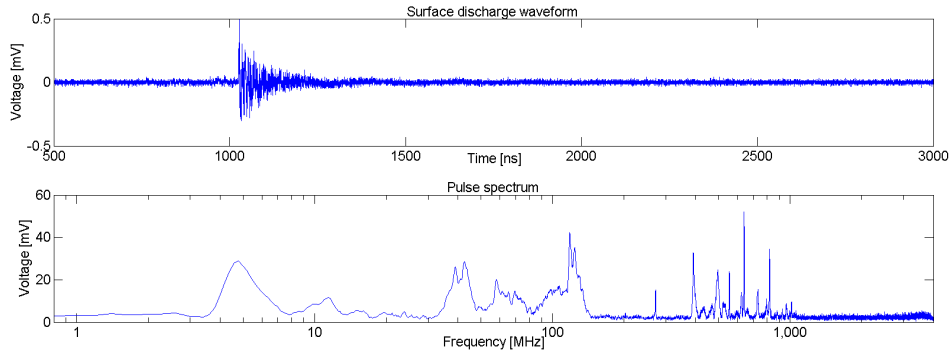


Figure 6.12: RF signal and frequency spectrum produced by a surface discharge.

The relationship graphs of the waveform and spectrum parameters to the apparent charge quantity show little correlation. The surface discharges have the possibility to propagate in all directions over the surface resulting in different angle of observations for successive discharges. The PDs are picked up differently by the UHF antenna and as seen for the waveform parameters the regression drops drastically. This is also the case for the frequency characteristics of the surface discharges although to a lesser effect as can be seen in fig. 6.13.

Frequency band (MHz)	R	m [mV/pC]	Waveform parameter		
0.8 – 3	0.4760	$9.3301e^{-4}$		R	m
4 – 7	0.6670	0.1010	V_{peak}	0.1956	$8.7411e^{-5}$ [mV _p /pC]
1 – 30	0.6329	0.6033	V_{pp}	0.2536	$1.9624e^{-4}$ [mV _{pp} /pC]
40 – 50	0.2925	0.0065	Energy	0.3446	$1.1850e^{-17}$ [J/pC]
60 – 100	0.2906	0.0020			
300 – 3000	0.2746	$3.4231e^{-4}$			

(a) Spectrum parameters.

(b) Waveform parameters.

Table 6.5: Value of regression coefficient R and slope m of regression line for surface discharges.

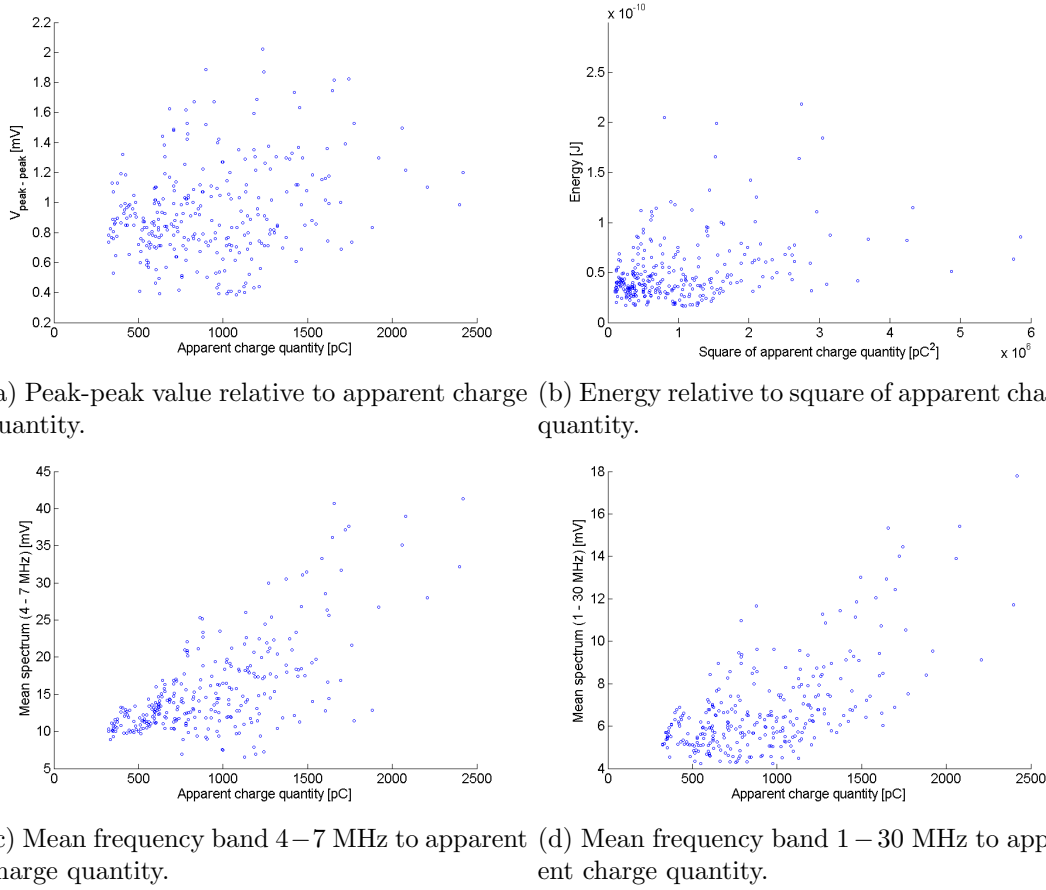


Figure 6.13: Relationship between RF signal surface discharges and apparent charge quantity.

6.3.6 Discussion

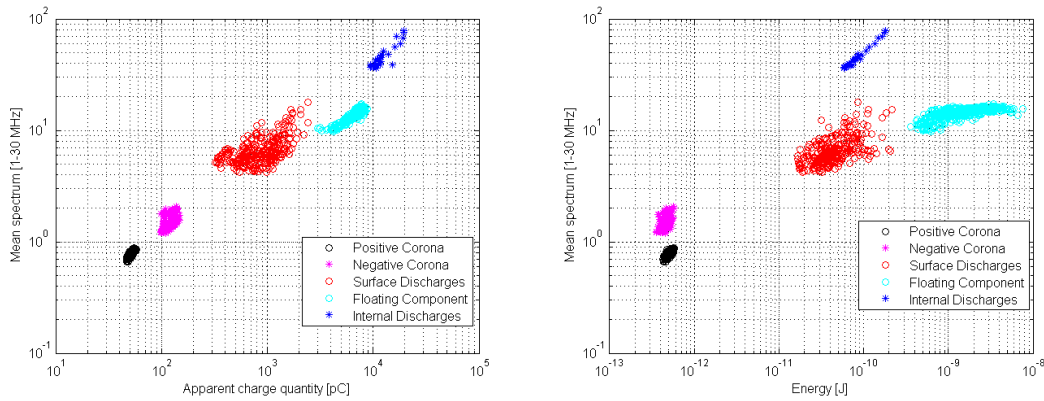
The results of the experiments with the combined RF and apparent charge measurements show for almost all tested defects a linear relation of one of the waveform or spectrum parameter to the apparent charge. A selection based on the regression coefficient R (see table 6.7) result in the parameters that have shown an adequate linear relationship to the apparent charge. The corresponding slopes of the regression lines m are bundled together in table 6.6 for comparison of the defects to one another. Table 6.6 shows no correlation between the slopes of the different insulation defect for the corresponding RF parameters. This indicates that the linear relationship for each type of defect is unique and as a result the RF signals cannot be calibrated using the exact same calibration procedure.

The differences in the regression curves are as a result of a multitude of variations in the defect sources. During the experiments, factors such as the dimension of the chamber, location of the defect and the response of the measurement system are kept constant as much as possible. The insulation defects themselves have resulted in variations of:

1. **Type of PD phenomenon.** The different insulation defects have resulted PD phenomena with varying RF waveforms. Discharge types such as the Townsend or Streamer mechanism have shown different energy distribution in the frequency spectrum as seen for internal discharges in section 6.3.4. The resonances are also affected by the discharge magnitude. The frequency distribution varies along with the discharge magnitude, such that linear relationships to RF parameters might not hold over large magnitude variations.

2. **Angle of observation.** The orientation of the discharge to the antenna greatly affects the picked up RF waveform. The effect of it can be seen the sections 6.3.3 and 6.3.5 for positive corona and surface discharges. For both defects, the discharge paths vary per discharge and thus also the RF waveform. As a result no convincing regression lines could be fitted over the dataset of these type of insulation defects. The angle of observation is thus a major drawback for the RF measurement for defects experiencing varying discharge paths.

The differences between the different insulation defects in the RF parameter regression curves create a potentiality in isolating and differentiating individual PD sources within data. An example of which is seen in the correlation graphs of the internal discharge in fig. 6.11. The graphs show a good separation for the different PD mechanisms for the RF parameters. This is also the case for multiple insulation defects in the same dataset as seen in fig. 6.14. The plots can be based on RF parameters plotted against the charge magnitude. The RF parameters



(a) Mean frequency band 1 – 30 MHz to apparent charge quantity. (b) Mean frequency band 1 – 30 MHz to RF energy.

Figure 6.14: Separation of PD sources based on RF parameters.

The quantification of the charge magnitude for certain RF parameters make defect recognition for insulation defects using DC recognition graphs possible. With prior knowledge of useful RF parameters, a time resolved discharge pattern with quantifiable charge magnitude data using only the UHF antenna can be retrieved from the RF waveforms originating from negative corona. This is seen in fig. 6.15. The visual tools such as the DC recognition plots in fig. 6.16 can help aid in the identification of the insulation defect as was discussed in chapter 5.

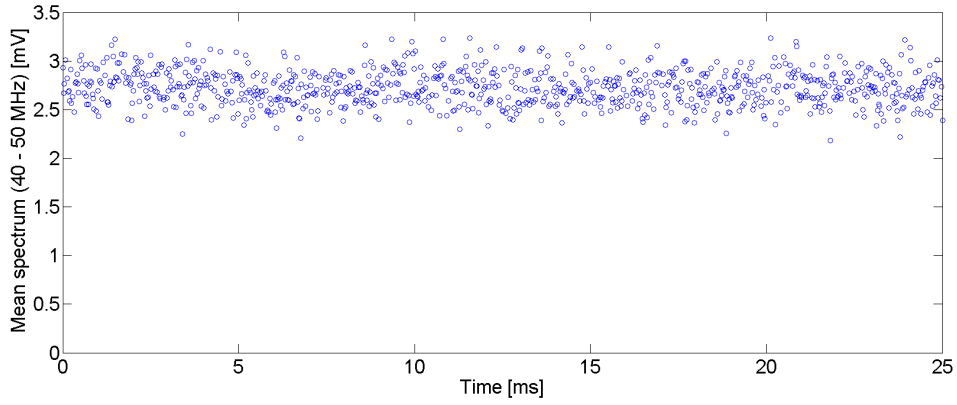


Figure 6.15: Time-resolved PD pattern of negative corona.

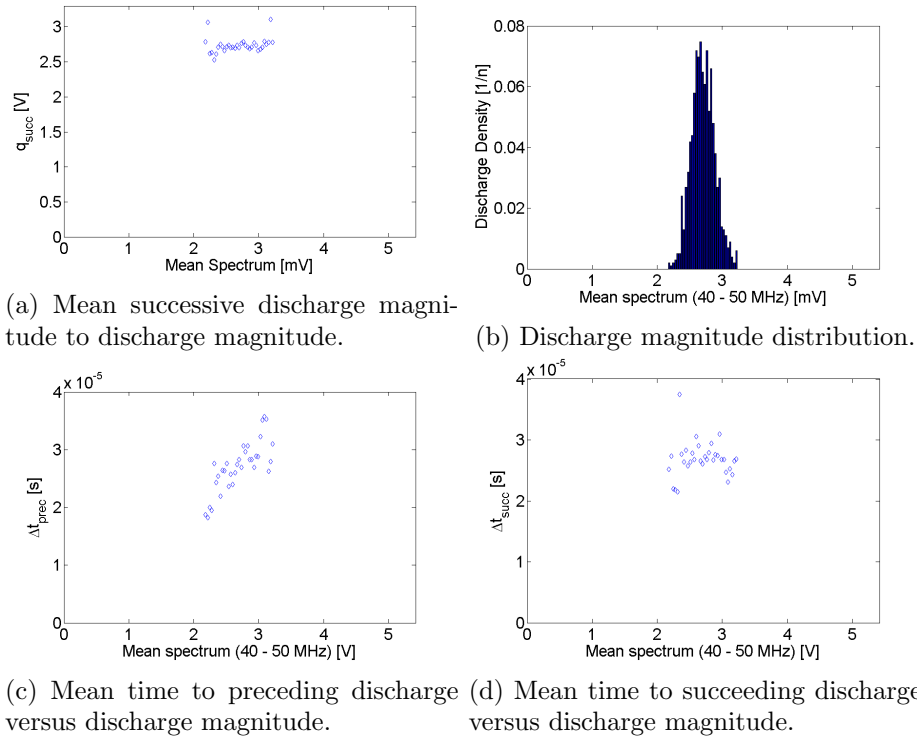


Figure 6.16: DC recognition plots of negative corona using the RF parameter of frequency selection between 40 – 50 MHz.

Spectrum parameters	Floating component	Negative corona	Positive corona	Internal discharges	
	<i>Streamer</i>	<i>Streamer</i>	<i>Streamer</i>	<i>Townsend</i>	<i>Streamer</i>
Frequency band (MHz)	m [V/pC]	m [mV/pC]	m [mV/pC]	m [mV/pC]	
0.8 – 3				0.0048	
4 – 7	0.0022		0.0273	0.0271	0.0393
1 – 30	0.0014	0.0167		0.0076	0.0145
40 – 50	0.0153	0.0759			0.0788
60 – 100	0.0085	0.0238			
300 – 3000					
Waveform parameters	Floating component	Negative corona	Positive corona	Internal discharges	
	Streamer	Streamer	Streamer	<i>Townsend</i>	<i>Streamer</i>
V_{peak}		$9.8720e^{-4}$ [mV _p /pC]		$6.3880e^{-5}$	[mV _p /pC]
V_{pp}		0.0017 [mV _{pp} /pC]		$1.2533e^{-4}$	[mV _{pp} /pC]
$Energy$		$1.2218e^{-16}$ [J/pC]		$6.7242e^{-18}$	$9.6938e^{-17}$ [J/pC]

Table 6.6: Selection of regression line slopes m of RF parameters to the apparent charge for multiple insulation defects.

Spectrum parameters	Floating component	Negative corona	Positive corona	Internal discharges		Surface discharges
	<i>Streamer</i>	<i>Streamer</i>	<i>Streamer</i>	<i>Townsend</i>	<i>Streamer</i>	<i>Streamer</i>
Frequency band (MHz)						
0.8 – 3	0.4524	0.0163	0.5891	0.9622	0.5103	0.4760
4 – 7	0.8036	0.7271	0.8471	0.9505	0.9874	0.6670
1 – 30	0.8960	0.8150	0.4674	0.8807	0.8559	0.6329
40 – 50	0.9441	0.9350	0.4134	0.6429	0.8642	0.2925
60 – 100	0.8510	0.8882	0.0728	0.7371	0.7528	0.2906
300 – 3000	0.3577	0.5677	0.0623	0.6855	0.7258	0.2746
Waveform parameters	Floating component	Negative corona	Positive corona	Internal discharges		Surface discharges
	<i>Streamer</i>	<i>Streamer</i>	<i>Streamer</i>	<i>Townsend</i>	<i>Streamer</i>	<i>Streamer</i>
V_{peak}	0.5448	0.8182	0.3427	0.8214	0.7831	0.1956
V_{pp}	0.5245	0.8738	0.3306	0.8291	0.7259	0.2536
$Energy$	0.4674	0.8669	0.4942	0.9037	0.8967	0.3446

Table 6.7: Regression coefficients R of RF parameters to the apparent charge for multiple insulation defects.

Chapter 7

Conclusions and Recommendations

The object of this thesis was to obtain diagnostic information from DC GISs using electrical PD detection methods. The thesis research was accomplished using several test techniques, experimental set-ups and analysis in the time and frequency domain. The results of the PD measurements concerning DC recognition of PD sources and the comparison of RF parameters to the apparent charge quantity are discussed in section 7.1. In section 7.2, recommendations regarding further research into DC PD monitoring of GIS are presented.

7.1 Conclusions

7.1.1 Recognition of PD under DC

Calibrated PD measurements were performed using the IEC method for the discharge types: floating component discharges, corona, internal discharges and surface discharges. The experimental set-ups for the defect types are validated by analysing the PRPD patterns in AC.

In DC the time-resolved pattern yields the parameters charge magnitude q and the time of discharge occurrence t_i . Using these parameters, the characteristic graphs $q_{succ} - q$, $\Delta t_{precc} - q$, $\Delta t_{succ} - q$ and the distribution of q are derived. These graphs are visual tools for understanding the PD sequence of the PD source. Additionally the repetition rate of the discharges and the *memory effect* or the lack of spotted in the discharge sequence are used to detect the insulation defects of floating component, needle protrusion, internal cavity and surface discharges.

The pulse sequence analysis of time-resolved PD patterns is not able to differentiate multiple defects or separate noise signals. To achieve better performance, separation of PD data based on the PD source should be undertaken prior to using this analysis. Separation and identification of PD sources using RF parameters as shown in fig. 6.11 and fig. 6.14 show possibilities using only RF sensors.

7.1.2 RF method

The research into the relationship between parameters of the RF waveform and the apparent charge quantity shows that the captured RF waveform is dependent upon several factors among which the resonances, location of the defect with respect to the antenna and the PD source.

Quantification of the charge magnitude is achieved for the defect types floating component, negative corona and internal discharges with a multitude of RF parameters. The

parameters that have shown promise are the RF energy and energy content between certain frequency bands.

The steepness of the PD pulse influences both the frequency content and the energy content of the frequency spectrum. This variation results in differences measured for different discharge mechanisms and discharge magnitudes for the same RF parameters preventing direct comparison to different insulation defects.

A limitation was discovered for this method concerning the orientation of the PDs to the sensors. This limitation obscures the linear relationship for RF parameters to the apparent charge for positive corona and surface discharges.

The relationship of RF parameters to the apparent charge quantity can aid in noise separation, recognition and discrimination of multiple defects.

7.2 Recommendations for future research

The experiments performed in this research project are an initial step towards establishing a PD monitoring system for DC GIS. Further research is necessary and could focus on:

- The severity of PD sources on HVDC equipment. The PDs in DC have a different repetitive nature and varying sequential charge magnitudes. As a result the acceptable PD levels for AC might not suffice and the criticality of PD in DC must be researched to determine acceptable levels.
- The effect of insulating gases. The results of all the experiments have been achieved with *air* as insulating medium. The electro-negative gas SF_6 will affect the discharge mechanism, the PD pulse and the discharge magnitude that will change the RF waveform completely. The electro negative gas will also see to a change in the *memory effect* of PDs resulting in possible different DC recognition graphs.
- The experimental results using the RF method have taken place with a fixed distance to the UHF antenna. Research should be carried out into varying distances between PD source and sensor and the effect it has on the RF signal and the relationship of the RF signal parameters to the apparent charge quantity.
- PD source localization techniques. Usage of multiple sensors and time of arrival techniques can determine the PD source location which can have the added function of multiple PD source identification. The location of the PD source can also possibly predict the insulation defect.

Appendix A

Spectrum Analyser Fundamentals

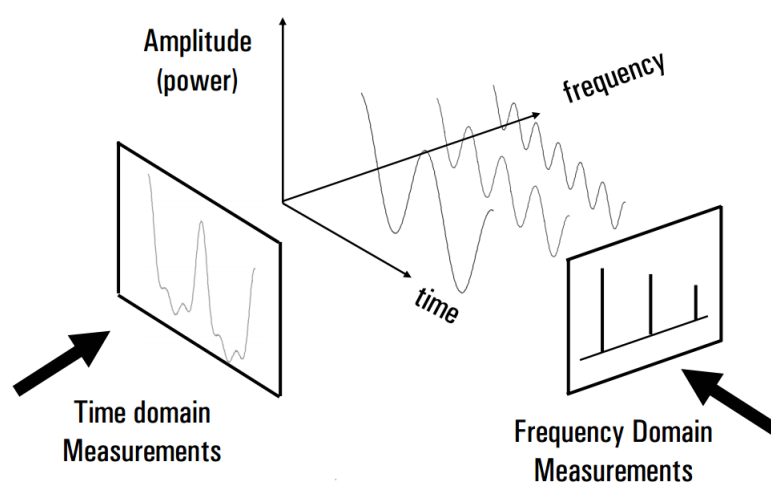


Figure A.1: Time and frequency domain of a signal[57].

Two types of SA are differentiated between determined by the method used to obtain a signal spectrum:

- **Super heterodyne Swept-Tuned SA** uses a Local Oscillator (LO) and a mixer to shift the preprocessed measuring signal to an Intermediate Frequency (IF).
- **Fast Fourier Transformation (FFT) SA** digitizes the time domain and applies digital signal processing techniques to decompose the signal into sinusoidal signals of different frequencies.

The block diagram in fig. A.2 describes the process of spectrum analysis of an input signal by the super heterodyne swept styled SA. The signal passes through an input attenuator and followed by a low pass filter. The signal is then mixed with a sinus from the LO outputting a signal that is composed of the frequencies of the two original, their harmonics and the sum and differences of these frequencies. The signal is passed through a bandpass filter with a bandwidth called the RBW used as a window to detect and pass only the wanted frequencies. A ramp generator sweeps the LO frequency through the span of desired frequencies that are displayed in windows of RBW bandwidth on the screen.

The x-axis on the display is linearly calibrated in frequencies and adjusted by setting the central frequency and then the span at the right and left of the central frequency. The y-axis shows the amplitude of the signal either in volts (linear scale) or in dB (logarithmic scale).

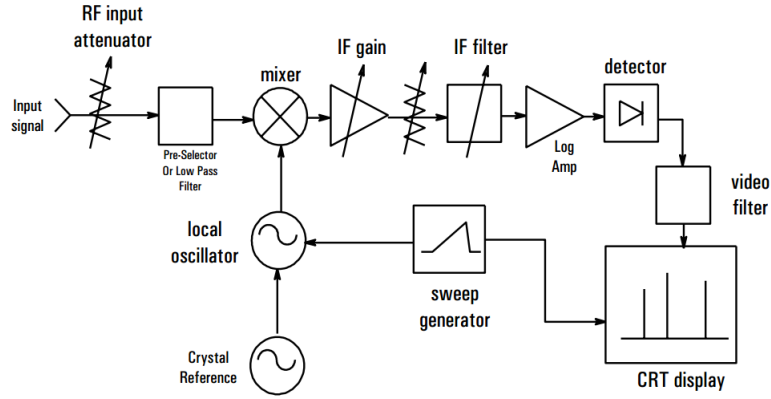


Figure A.2: Spectrum Analyser block diagram [57].

The IF filter is a circuit that needs a finite time to charge and discharge to detect the amplitude of the signal. The processing of the signal cannot be achieved too fast or a loss of signal would result. For this, the ST, the time in which the RBW window passes through the span of signals, is taken into account. The minimum ST is thus dependent on the span and the RBW as shown by:

$$ST = \frac{k(\text{span})}{RBW^2} \quad (\text{A.1})$$

Detection Modes

The signal is displayed in a number of discrete points or bins on the screen. Each of these points represents the information over a frequency range (RBW) by a certain time interval. Each of these intervals or bins contain data from both a time and span frame of which the relation is:

- Frequency bin width: $\frac{\text{span}}{\text{tracepoints}-1}$
- Time bin width: $\frac{ST}{\text{tracepoints}-1}$

Within these bins the data can be represented according to six detection modes which are:

- **Sample** detection modes that saves the instantaneous amplitude in the center of each bin good for showing the fluctuations within a bin.
- **Positive peak** only looking at the maximum within the bin.
- **Negative peak** in the same way as positive peak, but looking at the minimum in the bin.
- **Normal** detection mode shows the positive peak in the odd-numbered buckets and for the even-numbered buckets the negative peaks. These peaks are the minimum or maximum of not only the bucket measured but also the bucket before to ensure no peak is missed.
- **Average** is the detection mode that averages the trace point within a bin and displays the single average.
- **Quasi-peak detection** by detecting the charge rate of a signal and thus also result in information on the repetition rate within a bin.

Sensitivity

The measurement of a low-level signal is hindered by the noise generated by the SA itself. The noise is amplified by the several amplification stages and displayed and known as the Displayed Average Noise Level (DANL).

The input attenuator, the mixer, the amplifiers and other internal circuit elements produce noise that add up to the overall system noise. The additional noise has a constant amplitude over the span and gets amplified at the IF gain stage before reaching the IF filter. The noise power level that is passed through the filter is dependent on the RBW and it is seen that for continuous wave signals the best SNR is achieved by narrowing the RBW to a minimum, while for pulse signals the contrary holds true and a better SNR is achieved with larger bandwidth.

Appendix B

Amplifier response

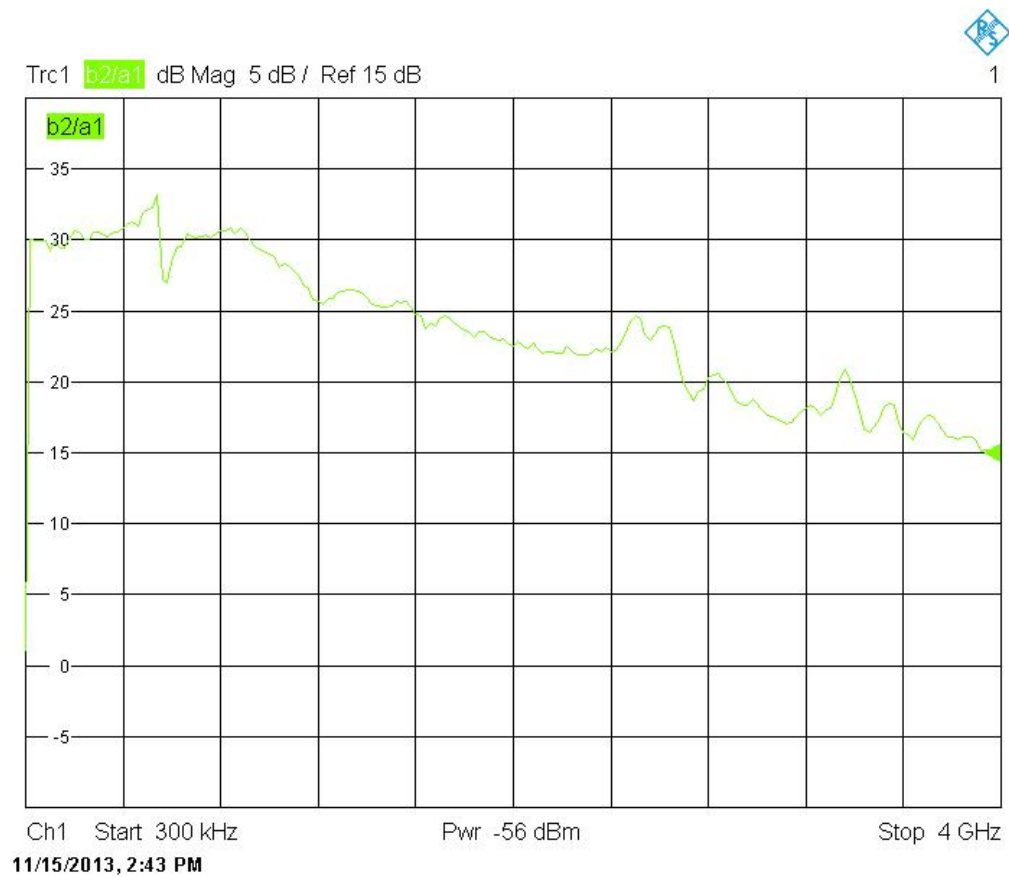


Figure B.1: Frequency response of HF amplifier III.

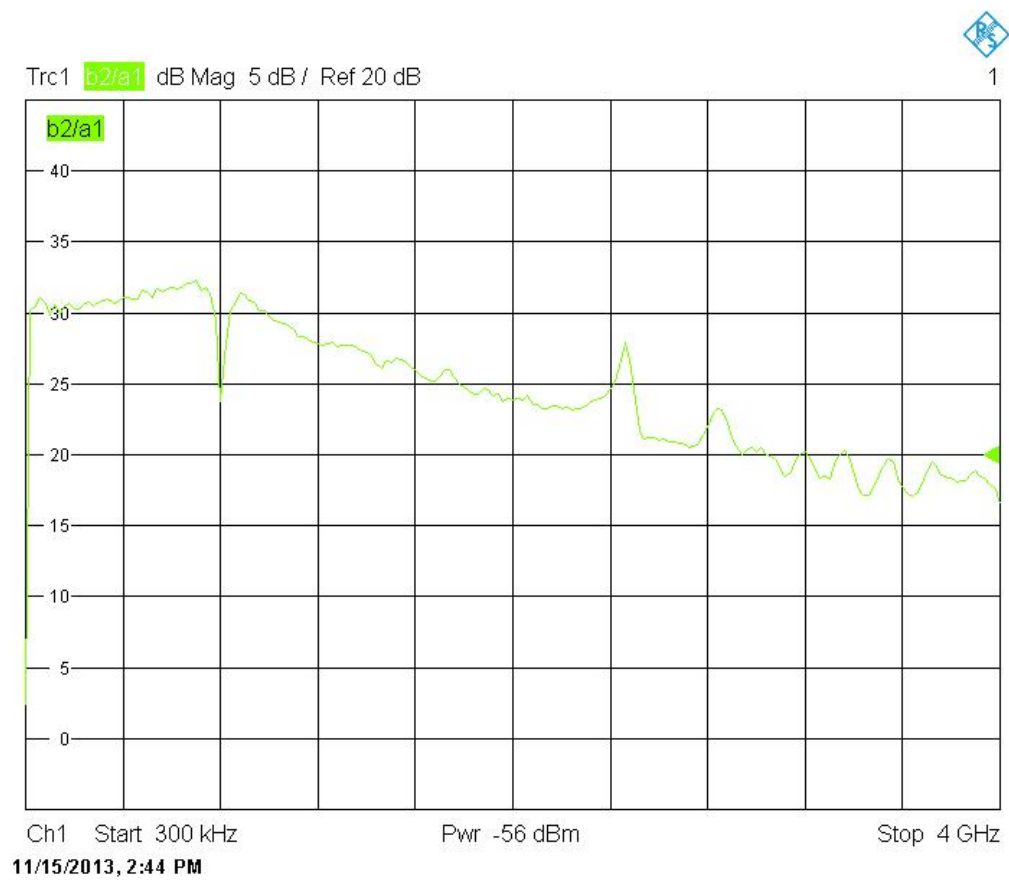


Figure B.2: Frequency response of HF amplifier IV.

Acknowledgements

Many people have contributed either directly or indirectly to the completion of this research project. I am so very grateful to have had them by my side.

Firstly, I would like to thank my promoter Prof. dr. Johan Smit for nudging me in the direction of this project at the very beginning of it all and allowing me to share my results to many visiting parties in the HV lab.

An enormous amount of gratitude to my supervisor Dr. ir. Armando Rodrigo Mor for guiding me through this whole project exploring the magical but unpredictable world of PDs. A vast amount of knowledge about so many different topics has kept me afloat so many times. As did the encouragement to keep on looking for the answer when the question had not yet been asked. I am truly grateful to have constantly received such unique support.

A great deal of thanks goes out to Roland Piccin, my predecessor to this project. After finishing his project, he has guided me so fluently through the initial stages of this project. His thorough knowledge of the GIS has helped me cut down on so much valuable time.

Special thanks to the staff of the HV laboratory Ing. Paul van Nes and Wim Termorshuizen for assisting me throughout the whole of my measurements. Every contraption I could think of was built, every practical problem had an even more practical solution. The memorable anecdotes told during 3 o'clock "tea time" have kept me laughing all day.

I would also thank the whole of the HV group, a rare group of unique minds. Alex Tsekmes, Roman Kochetov, Lukasz Chmura and Dennis van der Born for the discussions in the lab and my fellow master students Imke Zimmerling, Bert van Veen and Aniket Lewarkar for expressing their solidarity throughout.

Finally, I would like to thank my family for always being a source of inspiration to me and Sarah who has supported without fail.

Bibliography

- [1] Ram Adapa. High-wire act: HvdC technology: The state of the art. *Power and Energy Magazine, IEEE*, 10(6):18–29, 2012.
- [2] ALSTOM. *B105 170 – 300 kV Gas-insulated Substations*.
- [3] S. I. Cho. On-line pd (partial discharge) monitoring of power system components. Master’s thesis, Aalto, 2011.
- [4] S. Meijer. *Partial Discharge Diagnosis of High-Voltage Gas-Insulated System*. PhD thesis, Delft: Optima Grafische Communicatie, 2001.
- [5] C Neumann, B Krampe, R Feger, K Feser, M Knapp, A Breuer, and V Rees. Pd measurements on gis of different designs by non-conventional uhf sensors. In *Proc. Cigre Session*, 2000.
- [6] CIGRE WG 15.03. Diagnostic methods for gis insulating systems. In *CIGRE Report 15/2301*. Paris (1992).
- [7] C.M. Cooke, Roy E. Wootton, and Alan H. Cookson. Influence of particles on ac and dc electrical performance of gas insulated systems at extra-high-voltage. *Power Apparatus and Systems, IEEE Transactions on*, 96(3):768–777, May 1977.
- [8] M.E. Holmberg and S.M. Gubanski. Motion of metallic particles in gas insulated systems. *Electrical Insulation Magazine, IEEE*, 14(4):5–14, July 1998.
- [9] R. Baumgartner, B. Fruth, W. Lanz, and K. Pettersson. Partial discharge. ix. pd in gas-insulated substations-fundamental considerations. *Electrical Insulation Magazine, IEEE*, 7(6):5–13, Nov 1991.
- [10] Brian Hampton. Uhf diagnostics for gas insulated substations. 1999.
- [11] F.H. Kreuger. *Industrial High Voltage*. Delft University Press, 1991.
- [12] Ahdab El-Morshedy Roshdy Radwan M. Abdel-Salam, Hussein Anis. *High-Voltage Engineering*. Marcel Dekker, Inc., 2000.
- [13] G Hartmann and I Gallimberti. The influence of metastable molecules on the streamer progression. *Journal of Physics D: Applied Physics*, 8(6):670, 1975.
- [14] E. Kuffel, W. Zaengl, and J. Kuffel. *High Voltage Engineering: Fundamentals*. Newness, 2000.
- [15] JM Meek. The mechanism of growth of spark discharges. *Applied Scientific Research, Section A*, 5(1):269–276, 1956.
- [16] Leonard B Loeb. Streamer breakdown and sparking thresholds. *Physical Review*, 81(2):287, 1951.

- [17] P.H.F. Morshuis. *Partial Discharge Mechanisms*. PhD thesis, Delft University of Technology, 1993.
- [18] F.H. Kreuger. *Industrial High DC Voltage*. Delft University Press, 1995.
- [19] U. Fromm. *Partial Discharge and Breakdown Testing at High DC Voltage*. PhD thesis, Delft University of Technology, 1995.
- [20] Peter Morshuis and Marc Jeroense. Space charge in hvdc cable insulation. In *Electrical Insulation and Dielectric Phenomena, 1997. IEEE 1997 Annual Report., Conference on*, volume 1, pages 28–31. IEEE, 1997.
- [21] Marc Jan Petrus Jeroense. Charges and discharges in hvdc cables-in particular in mass-impregnated hvdc cables. 1997.
- [22] L Niemeyer, L Ullrich, and N Wiegart. The mechanism of leader breakdown in electronegative gases. *Electrical Insulation, IEEE Transactions on*, 24(2):309–324, 1989.
- [23] E. Lemke. A critical review of partial-discharge models. *Electrical Insulation Magazine, IEEE*, 28(6):11–16, Nov 2012.
- [24] Lutz Niemeyer. A generalized approach to partial discharge modeling. *Dielectrics and Electrical Insulation, IEEE Transactions on*, 2(4):510–528, 1995.
- [25] F Gutfleisch and L Niemeyer. Measurement and simulation of pd in epoxy voids. *Dielectrics and Electrical Insulation, IEEE Transactions on*, 2(5):729–743, 1995.
- [26] Alan H Cookson. Review of high-voltage gas breakdown and insulators in compressed gas. *Physical Science, Measurement and Instrumentation, Management and Education-Reviews, IEE Proceedings A*, 128(4):303–312, 1981.
- [27] HFA Verhaart, J Tom, AJL Verhage, and CS Vos. Avalanches near solid insulators. In *Proceeding of the 5th International Symposium on HV Engineering, Braunschweig*, 1987.
- [28] AK Chakrabarti, RG Van Heeswijk, and KD Srivastava. Spacer involvement in conducting-particle-initiated breakdown in compressed gas insulated systems. *Electrical Insulation, IEEE Transactions on*, (4):431–438, 1987.
- [29] T. Nitta, Y. Shibuya, Y. Fujiwara, Y. Arahata, H. Takahashi, and H. Kuwahara. Factors controlling surface flashover in sf6 gas insulated systems. *Power Apparatus and Systems, IEEE Transactions on*, PAS-97(3):959–968, May 1978.
- [30] O Farish and I Al-Bawy. Effect of surface charge on impulse flashover of insulators in sf 6. *Electrical Insulation, IEEE Transactions on*, 26(3):443–452, 1991.
- [31] C.M. Cooke. *Gaseous Dielectrics III*. Pergamon, 1982.
- [32] J.R. Laghari and A. H. Qureshi. Surface flashover of spacers in compressed gas insulated systems. *Electrical Insulation, IEEE Transactions on*, EI-16(5):373–387, Oct 1981.
- [33] Shigemitsu Okabe. Phenomena and mechanism of electric charges on spacers in gas insulated switchgears. *Dielectrics and Electrical Insulation, IEEE Transactions on*, 14(1):46–52, 2007.

- [34] K. Nakanishi, A. Yoshioka, Y. Arahata, and Y. Shibuya. Surface charging on epoxy spacer at dc stress in compressed sf₆ gas. *Power Apparatus and Systems, IEEE Transactions on*, PAS-102(12):3919–3927, Dec 1983.
- [35] A. Kumada and S. Okabe. Charge distribution measurement on a truncated cone spacer under dc voltage. *Dielectrics and Electrical Insulation, IEEE Transactions on*, 11(6):929–938, Dec 2004.
- [36] S.A. Boggs, G. L. Ford, and R. C. Madge. Coupling devices for the detection of partial discharges in gas-insulated switchgear. *Power Apparatus and Systems, IEEE Transactions on*, PAS-100(8):3969–3973, Aug 1981.
- [37] JM Braun, FY Chu, and R Seethapathy. Characterization of gis spacers exposed to sf₆ decomposition products. *Electrical Insulation, IEEE Transactions on*, (2):187–193, 1987.
- [38] N Wiegart, L Niemeyer, F Pinnekamp, J Kindersberger, R Morrow, W Zaengl, M Zwicky, I Gallimberti, and SA Boggs. Inhomogeneous field breakdown in gis-the prediction of breakdown probabilities and voltages. i. overview of a theory for inhomogeneous field breakdown in sf₆. *Power Delivery, IEEE Transactions on*, 3(3):923–930, 1988.
- [39] AED Heylen. Sparking formulae for very high-voltage paschen characteristics of gases. *Electrical Insulation Magazine, IEEE*, 22(3):25–35, 2006.
- [40] Heinzinger GmbH. *PNC series - User Manual*, 2012.
- [41] International Electrotechnical Commission et al. Iec 60270 standard. *High-voltage test techniques-Partial discharge measurements*, 2000.
- [42] Eberhard Lemke, S Berlinjn, Edward Galski, Michael Muhr, E Pultrum, T Strehl, W Hauschild, J Rickmann, and G Rizzi. Guide for partial discharge measurements in compliance to iec 60270. *CIGRE, WG D*, 1, 2008.
- [43] A Rodrigo, P Llovera, V Fuster, and A Quijano. Study of partial discharge charge evaluation and the associated uncertainty by means of high frequency current transformers. *Dielectrics and Electrical Insulation, IEEE Transactions on*, 19(2):434–442, 2012.
- [44] John Sheffield, Dustin Froula, Siegfried H Glenzer, and Neville C Luhmann Jr. *Plasma Scattering of Electromagnetic Radiation: Theory and Measurement Techniques*. Academic press, 2010.
- [45] Karl Erik Lonngren, Sava Vasilev Savov, and Randy J Jost. *Fundamentals of Electromagnetics with MATLAB*. Scitech publishing, 2007.
- [46] P.D. Agoris. *Sensitivity verification of radio frequency partial discharge detection in high voltage equipment*. PhD thesis, Delft University of Technology, 2009.
- [47] G Wanninger. Apparent charge measurement in gis by modern diagnostic methods. *European transactions on electrical power*, 7(4):251–255, 1997.
- [48] Martin D Judd, Li Yang, and Ian BB Hunter. Partial discharge monitoring of power transformers using uhf sensors. part i: sensors and signal interpretation. *Electrical Insulation Magazine, IEEE*, 21(2):5–14, 2005.

- [49] S Meijer, WR Rutgers, and JJ Smit. Acquisition of partial discharges in sf 6 insulation. In *Electrical Insulation and Dielectric Phenomena, 1996., IEEE 1996 Annual Report of the Conference on*, volume 2, pages 581–584. IEEE, 1996.
- [50] A Contin, A Cavallini, GC Montanari, G Pasini, and F Puletti. Digital detection and fuzzy classification of partial discharge signals. *Dielectrics and Electrical Insulation, IEEE Transactions on*, 9(3):335–348, 2002.
- [51] T Okamoto and T Tanaka. Novel partial discharge measurement computer-aided measurement systems. *Electrical Insulation, IEEE Transactions on*, (6):1015–1019, 1986.
- [52] J. Beyer. *Space Charge and Partial Discharge Phenomena in High Voltage DC Devices*. PhD thesis, Delft University of Technology, 2002.
- [53] BG Stewart, AJ Reid, MD Judd, and RA Fouracre. Uhf and iec60270 correlation analysis of radiated frequency band measurements on resin insulation void samples. In *Electrical Insulation Conference and Electrical Manufacturing Expo, 2007*, pages 138–141. IEEE, 2007.
- [54] BG Stewart, MD Judd, AJ Reid, and RA Fouracre. Suggestions to augment the iec60270 partial discharge standard in relation to radiated electromagnetic energy. In *Electrical Insulation Conference and Electrical Manufacturing Expo, 2007*, pages 175–178. IEEE, 2007.
- [55] L Yang, MD Judd, and G Costa. Simulating propagation of uhf signals for pd monitoring in transformers using the finite difference time domain technique [power transformers]. In *Electrical Insulation and Dielectric Phenomena, 2004. CEIDP'04. 2004 Annual Report Conference on*, pages 410–413. IEEE, 2004.
- [56] S Xiao, PJ Moore, MD Judd, and IE Portugues. High frequency finite element analysis of electromagnetic radiation due to partial discharges in high voltage equipment. In *Power and Energy Society General Meeting-Conversion and Delivery of Electrical Energy in the 21st Century, 2008 IEEE*, pages 1–7. IEEE, 2008.
- [57] Agilent Technologies. *Spectrum Analyzer Basics*.